Characterization of high-purity, multi-segmented germanium detectors

Michaël Ginsz

UNIVERSITÉ DE STRASBOURG

ÉCOLE DOCTORALE pcp Physique et Chimie-Physique

Université de Strasbourg

Ecole doctorale de physique et chimie physique
Institut Pluridisciplinaire Hubert Curien
UMR 7178 CNRS/IN2P3

Thèse

présentée par

Michaël Ginsz

soutenue le :
Mercredi 30 septembre 2015

pour obtenir le grade de : **Docteur de l'Université de Strasbourg**
discipline : physique

Caractérisation de détecteurs multi-segmentés au germanium hyper pur

Characterization of high-purity, multi-segmented germanium detectors

Thèse dirigée par :
Monsieur Gilbert Duchêne — directeur de recherches, Institut Pluridisciplinaire Hubert Curien

Rapporteurs :
Madame Amel Korichi — directrice de recherches, Centre de Sciences Nucléaires et de Sciences de la Matière
Monsieur Andy Boston — senior lecturer, University of Liverpool

Autres membres du jury :
Madame Araceli Lopez Martens — directrice de recherches, Centre de Sciences Nucléaires et de Sciences de la Matière
Monsieur Benoît Gall — professeur, Université de Strasbourg
Monsieur Benoît Pirard — ingénieur, CANBERRA France

IPHC Institut Pluridisciplinaire Hubert CURIEN STRASBOURG

cnrs dépasser les frontières

CANBERRA

Remerciements

Quelle aventure cette thèse. Tout a commencé en Aout 2012 par ce coup de fil d'un certain Benoît Pirard et se termine après trois ans (plus quelques mois de retard) avec un chien, un mariage et un bébé. Avec le recul, ça n'était pas gagné d'avance de travailler pour la physique nucléaire quand on n'a pas appris ça à l'école. Je trouve le résultat plutôt pas mal et ça n'a été possible que grâce à aux nombreuses personnes que j'ai côtoyé durant ces années. Je vous suis à tous très redevable.

Tout d'abord un grand merci à Benoît Pirard, qui est à l'origine de tout ça en ayant pensé à moi il y a trois ans. Ta vision côté industriel et tes commentaires constructifs, parfois sceptiques m'ont permis de développer mon esprit critique et m'ont poussé à aller explorer toujours plus loin afin de prouver la valeur de mon raisonnement.

Un autre grand merci à Gilbert Duchêne, tu as été un directeur de thèse toujours disponible et très pédagogue. Ca a été un réel plaisir de t'avoir comme chef et collègue.

Merci à François Didierjean pour son suppport technique, pour m'avoir tant aidé en partageant son expérience du scan de détecteur et en vulgarisant pour moi la physique subatomique, ce qui n'était pas la panacée avec moi.

Merci aux autres de la "team scanning" de l'IPHC: à Marie-Hélène Sigward et à Michel Filliger, ce fut très agréable de travailler avec vous. Gardez le moral et faites en baver au suivant juste pour rigoler.

Merci aux membres de la commnuauté AGATA, tout mes voeux de réussite.

Merci à Christelle Roy et à Marie-Odile Lampert de m'avoir accueilli respectivement au sein de son laboratoire et de son entreprise.

Merci à mes parternaires de bureau et de galère: merci à Regina qui m'a permis d'avancer à pas de Geant en C++, en ROOT et en Geant4, merci à Andreina "reine de la malchance", à tes côtés on se sent le plus chanceux du monde ;), merci Houda pour ta bonne humeur. Ce fut un plaisir de partager notre bureau ensemble et je vous souhaite à chacune le meilleurs pour l'avenir.

Merci aux autre jeunes galériens qui ont croisé plus ou moins longtemps mon chemin, Didi, Hugo, Fabien, Momo, Jérôme, Pierre, même Loic. Vous avez quelque part tous un peu cimenté le grand édifice de ce travail.

Merci à l'ensemble du groupe CAN pour votre accueil chaleureux et toutes ces discussions plus ou moins constructives. Merci à la jamais neutre reine des neutrons Louise Stuttgé pour sa bonne humeur communicative, à Benoît Gall, Olivier Dorveaux, François Leblanc et Dominique Curien pour leur expertise et leurs conseils. Merci aussi au transfuge Christian Finck pour son cynisme à toute épreuve qui me plaît bien et merci à Nicole qui faisait pour moi tout autant partie du groupe CAN que les autres. Un merci un peu spécial à Marc et Olivier pour la gestion de l'indispensable or noir multicolore: les dosettes de café. C'est rarement gratifiant de se farcir les commandes pour tout ces affreux jojos en manque, moi j'étais bien content alors merci.

Merci aussi à ceux du groupe théorie amateurs de pauses café. Vous ne parlez pas toujours français pour moi mais on a bien rigolé.

Merci à ceux qui on permis à la table de scan de scanner: au service mesure et acquisition et aux gens de la méca. Merci particulièrement à Marc Richer et Laurent Charles: sans vous j'aurais conclu ma thèse en transformant l'adage *pas de bras, pas de chocolat* en *pas*

d'acquisition, pas de doctorat. D'ailleurs, merci à ceux qui ont contribué à développer les TNT2, j'ai dû lancer quelque chose comme 100 000 runs durant ces trois dernières années en mesurant une bonne centaine de To de data et elles n'ont pas bronché, bravo pour ces bonnes vieilles cartes.

Je tiens également à remercier l'ensemble du personnel de Canberra. Peut-être que tout n'est pas toujours rose mais vous êtes quoi qu'il en soit des gens bien et sympathiques, c'est un plaisir de venir travailler parmi vous après cette aventure. Je remercie plus particulièrement Mustapha Allali, Pascal Quirin, Vlad Marian, Yvan Hieter pour toutes ces discussions, ces infos, ces conseils que vous m'avez donnés et qui ont été enrichissant.

A tous les oubliés je vous dis un gros merci accompagné de mes excuses. S'il y en a parmi vous trop vexés contactez moi[1] et on règlera ça autour d'un verre de schnapps.

Merci aussi à ceux du MOC Volley Ball qui étaient toujours là pour bien s'amuser le Vendredi soir. Un merci spécial à Franck, voilà, tu es cité dans une thèse, belle réussite félicitations !

Merci les pompiers, même si je n'ai pas réussi à vous faire comprendre ce que je fais ça m'a fait du bien de passer du temps avec vous.

Merci à mes parents et à ma soeur qui m'ont toujours soutenu à leur façon.

Enfin un énorme merci et un gros schmoutz à ma petite famille grâce à qui tout est bien qui finit merveilleusement bien, Lucie, Andrea et Hyoshi, je vous aime, pardon pour tout ces sacrifices et en route pour la suite.

[1] michael.ginsz@laposte.net, bah oui j'allais quand même pas vous donner mon numéro de portable.

Contents

Introduction

Gamma-ray spectroscopy in the field of nuclear structure has reached unprecedented complexity. The comprehension of matter goes through the study of exotic nuclei still farther from the stability, produced with very low cross-sections. Such work requires the use of γ-ray detection devices, able to deal typically with high background, high γ-ray multiplicities and eventually large peak broadening due to Doppler effect. The last generation of High Purity Germanium (HPGe) γ-ray spectrometers such as EUROBALL and GAMMASPHERE were dedicated to such purpose. Unfortunately, they reached the limit of photopeak detection efficiency, due to the use of Compton suppression shields. The later cover about 50% or 4π steradian around the reaction chamber, thus limiting the available space for germanium. Also the Doppler correction was limited by the finite size of each individual HPGe detector. New technologies in HPGe detectors, such as electric segmentation, coupled with digital signal analysis have been used to develop position-sensitive devices, which triggered the concept of γ-ray tracking. AGATA and GRETINA are state-of-the-art spectrometers dedicated to γ-ray tracking. They are composed of hundreds of HPGe large volume, multi-segmented detectors, which provide pulse shapes varying with the location of the γ-ray interaction in the crystal. They are using Pulse Shape Analysis (PSA) in order to localize the position of γ-ray interactions within the crystal. It relies on the comparison of experimental signal shapes with a signal database. Such information allows to recover the γ-ray path in germanium and the total energy of the γ-ray, thus greatly improving the resolving power of the array compared to the previous γ-ray spectrometer generation. In addition, the accurate determination of the position of the first interaction point enables to correct efficiently for the Doppler broadening of the γ lines.

The overall position resolution which has been reached is not yet as small as expected, most probably because signal databases used until now come from simulations which are not realistic enough. An improvement is expected if simulated signal databases were replaced by experimental ones. Germanium-detector scanning tables which extract experimental signal shapes as a function of the location of the γ-ray interaction exits since more than ten years. The coincidence method used allows to extract the mean pulse shape of $\sim$1200 points in 1-2 months scans. This is too long to provide a complete database of measured signal shapes for each detector.

The IPHC has developed a scanning table dedicated to perform Pulse Shape Comparison Scan (PSCS), a fast technique which for the first time, allows to create a 48500 points, exhaustive, complete experimental pulse-shape database in only two-weeks scan. The systematic scan of each individual detector is now possible which could lead to a breakthrough for the detector properties comprehension and for the overall AGATA array performances. Also, such information can be used to design specific devices for γ-ray imaging or Comp-

ton suppression with pulse-shape analysis, thus opening the way for various HPGe detector applications.

The main purpose of this thesis work is to test the PSCS technique and to perform it in the whole volume of AGATA crystals. The first chapter briefly summarizes some of the physics background required for understanding. The second one develops the various steps leading to the output signal-shape generation in HPGe detectors. Then, both PSCS technique and IPHC scanning table are described in detail in chapter 3. Detector characterization by two dimension scans are presented in chapter 4. Several topics are investigated such as charge-carrier trapping, doped-contact issues or even inter-segment charge sharing. Finally, the last chapter demonstrates the PSCS performance through simulations for 3D scans and experimental results of a full AGATA-crystal scan are shown and discussed. The resulting experimental signal database is compared to a simulated one in order to point out serious advantages when the former one is used in PSA algorithms.

Chapter 1

From γ-ray interaction to high-purity germanium array

This chapter is dedicated to the physical processes involved for γ-ray detection in High-Purity Germanium Detectors (HPGe). Photons can undergo various interaction mechanisms when they go through matter. Most of them lead to the generation of charge carriers in HPGe detectors, forming an electrical signal proportional to the energy deposit. The performance of the detector relies on the quality of the charge-carrier collection, which depends on various factors such as the electrical field inside the detector, the crystalline anisotropy, the crystal purity. These variations are exploitable as an additional information, through pulse shape analysis (PSA).

This chapter briefly describes :

- the possible interactions between γ-rays and matter,
- the use of semiconductor detectors for γ-ray spectroscopy,
- some characteristics of HPGe detectors and HPGe arrays,
- the status-of-the-art γ-ray spectrometer AGATA.

1.1 γ-ray interaction with matter

The γ-rays are high-energy photons emitted by exited nuclei in their transition to lower-lying nuclear levels. A γ-ray does not necessarily interact with matter: the photon has a probability to interact by various mechanisms, depending of its initial energy and of the nature of the absorbing material. After the interaction it can either disappear leaving all its initial energy, or scatter leaving partially its energy. The γ-ray interaction itself is not detected, but it generates secondary electrons, which ionize the surrounding material, enabling its detection. Figure 1.1 shows the relative cross sections of relevant processes of γ-ray interaction in germanium, in the energy range of interest for γ-ray spectroscopy, i.e. from few keV to several MeV. As the energy increases, three major processes are dominating: photoelectric absorption up to $\sim$150 keV, Compton scattering up to $\sim$8 MeV and pair creation for higher energies. The following sub-sections describe these processes. A more detailed description can be found in [1].

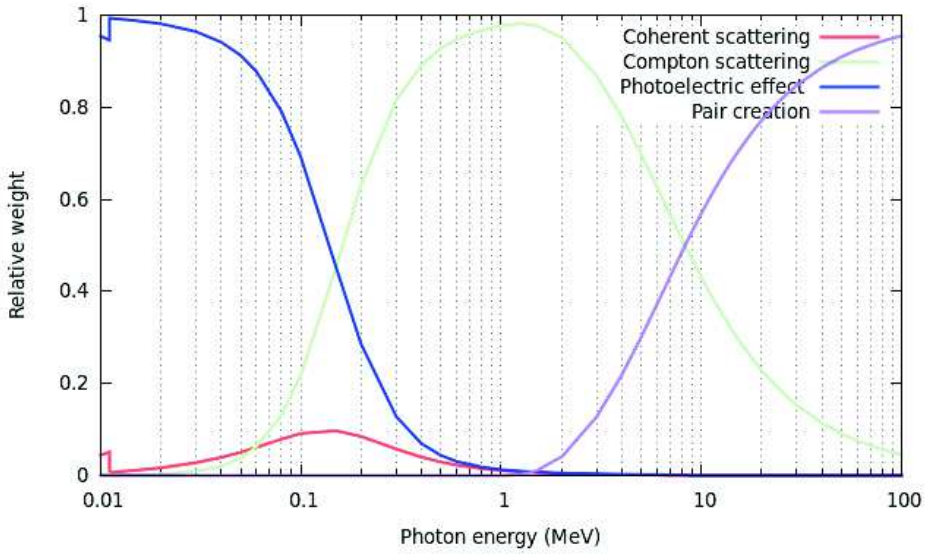

Figure 1.1: Relative cross-sections for the different process of photon interaction in germanium [2].

1.1.1 Photoelectric absorption

In this process, the γ-ray transfers all its energy E_0 to one of the orbital electron of an atom from the absorbing material. This electron, called photoelectron, is ejected from its valence shell with an energy $E_{e-} = E_0 - E_i$ where E_i is the ionization energy of the considered atomic shell. The condition for a photoelectric absorption is $E_0 >> E_i$. The photoelectron leaves an ionized atom behind it. This vacancy is immediately filled with a free electron of the surrounding material, or with an electronic rearrangement. It is likely that an X-ray is emitted. Usually, this X-ray is reabsorbed close to its emission location but sometimes it can escape, affecting the detector response.

Although there is no analytical expression giving the probability for a photoelectric absorption, for an energy E_0 and an atomic number Z, an approximation for the atomic cross-section is:

$$\sigma_{\text{photoelectric}} \propto \frac{Z^n}{E_0^{3,5}} \tag{1.1}$$

where the exponent n varies between 4 and 5, depending on the energy range of the considered γ-ray. This expression shows the strong dependency of the photoelectric effect with Z and E_0. The cross-section increases drastically with the atomic number of the absorbing nucleus and decreases rapidly with increasing incident photon energy.

1.1.2 Compton scattering

In the energy range of standard γ-ray spectroscopy, Compton scattering is the dominant interaction mechanism. Therefore all the results presented in the following chapters are strongly affected by this effect.

The γ-ray undergoes an inelastic collision with an electron of the absorbing material, known as recoil electron. The photon with initial energy $h\nu_0$ is then deflected at a given angle θ with respect to its original direction. The total energy is split between the recoil electron and the scattered γ-ray (with energy $h\nu'$) as a function of θ. The energy of the scattered photon is related to the scattering angle θ as follows :

$$h\nu' = \frac{h\nu_0}{1+\alpha(1-\cos\theta)} \quad \text{with} \quad \alpha = \frac{h\nu_0}{m_0c^2} \tag{1.2}$$

where m_0c^2 is the rest-mass energy of the electron (511 keV). This formula is called the Compton equation. It is of great importance for Compton imaging as for the tracking algorithms which reconstruct the γ-ray path in HPGe detectors and are used for tracking arrays such as AGATA or GRETINA.

The Compton scattering probability of a given material depends on the number of electrons available, i.e. it varies linearly with Z. The Klein-Nishina formula predicts the differential Compton-scattering cross-section $d\sigma/d\omega$ as follows:

$$\frac{d\sigma}{d\omega} = Zr_0^2 \left(\frac{1}{1+\alpha(1-\cos\theta)}\right)^2 \left(\frac{1+\cos^2\theta}{2}\right) \left(1+\frac{\alpha^2(1-\cos\theta)^2}{(1+\cos^2\theta)[1+\alpha(1-\cos\theta)]}\right) \tag{1.3}$$

where r_0 is the electron radius. This distribution is plotted in fig. 1.2 for some relevant energies. It shows an increasing forward scattering with increasing incident γ-ray energy.

1.1.3 Pair creation

For γ-ray energies exceeding two times the electron rest-mass energy (1.022 MeV), a photon can materialize in a pair of electron and positron in the Coulomb field of a nucleus. This process called pair creation has tiny cross-section values in germanium below few MeV and dominates Compton scattering cross-sections above $\sim$8 MeV. The energy excess carried by the photon corresponds to the kinetic energy equally shared between electron and positron. Both particles are slowed down in the material. When the positron is at rest it annihilates with an electron of the surrounding environment which produces two 511 keV γ-rays emitted in opposite direction.

No simple formula describes the pair creation cross-section which varies roughly as the square of the absorber atomic number :

$$\sigma_{\text{pair}} \propto Z^2 \tag{1.4}$$

1.1.4 Coherent scattering

Another possible interaction mechanism is the coherent scattering or Rayleigh scattering. Due to its small cross-section, limited to low energies, it is often neglected. For a more detailed description, see [3]. Rayleigh scattering is an elastic collision between a photon and an absorber atom, characterized by photon scattering on bound atomic electrons. As a result of the interaction, the atom is neither excited nor ionized and after the interaction the bound electrons revert to their original state. The atom as a whole absorbs the transferred

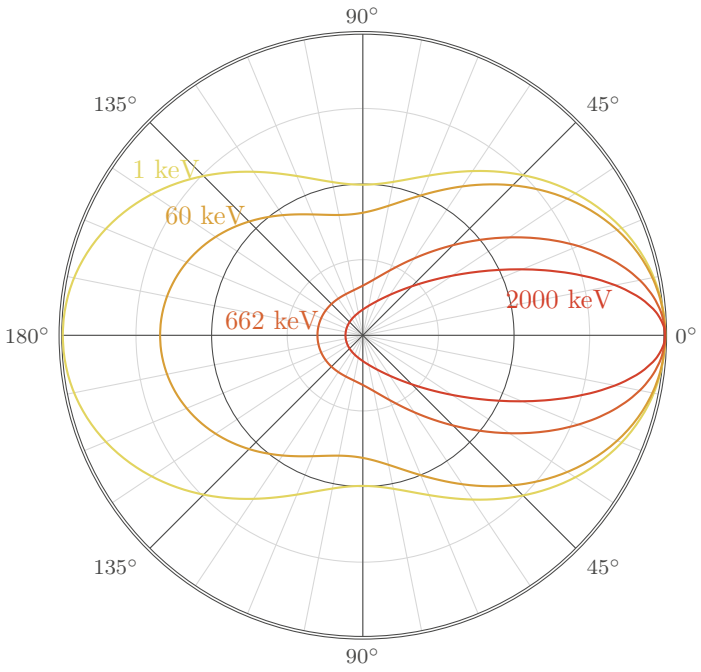

Figure 1.2: Probability of Compton scattering as a function of the scattering angle θ for an incident γ-ray coming from the left. The different curves correspond to various initial energies.

momentum but its recoil energy is very small and the incident photon scattered has essentially the same energy as the original photon. The scattering angles are relatively small because the recoil imparted to the atom produces no atomic excitation nor ionization. In the case of a γ-tracking device, this effect contributes to an undetectable weak scattering of photons. The relative cross-section for coherent scattering is minor compared to the other effects, as seen in fig. 1.1, such that it does not affect significantly the work presented here.

1.1.5 γ-ray detector predicted response

As a result of these various interaction processes, a mono-energetic γ-ray interacting in a detector does not necessarily lead to full energy deposit, as shown in fig. 1.3. A large fraction of incoming γ-rays are partially absorbed depending on various factors such as their energy, their angle of incidence, the interaction location and the detector geometry.

The largest contribution to partial energy deposits is Compton scattering. All scattering angles being allowed, the energy varies from zero to the maximum predicted in eq. 1.2 for backscattering, which corresponds to the Compton edge in the spectrum. As γ-rays are likely to undergo several Compton scatterings and then escape, these multiple events fill the spectrum between the Compton edge and the full-energy peak. The continuum can be split in two contributions : 1) primary photons coming from the γ-ray source which undergo Compton scattering in the detector and then escape, 2) secondary photons which are scattered in surrounding inert material towards the detector. Hence the surrounding material has an

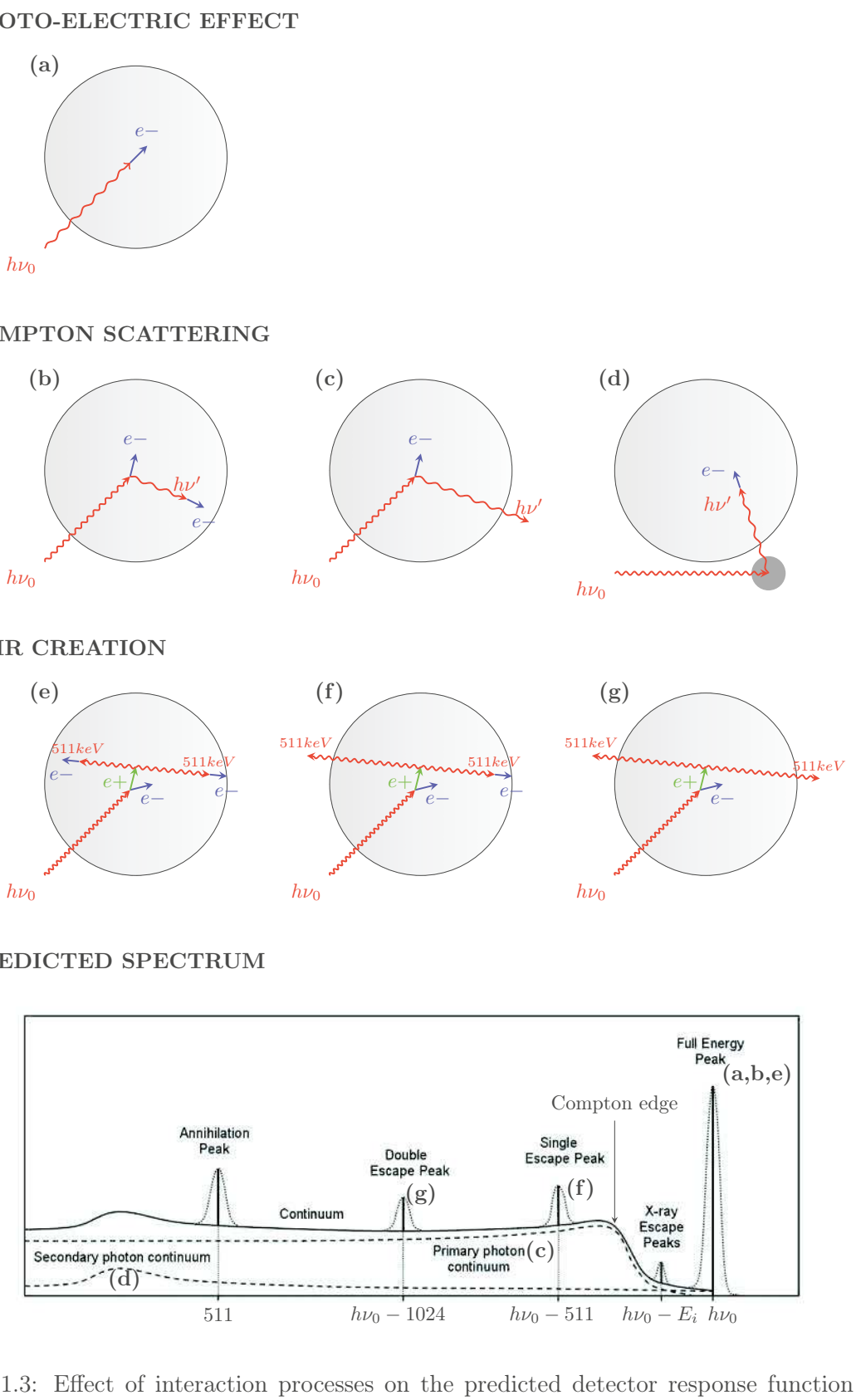

Figure 1.3: Effect of interaction processes on the predicted detector response function for mono-energetic γ-rays with $h\nu_0 >> 1.022MeV$.

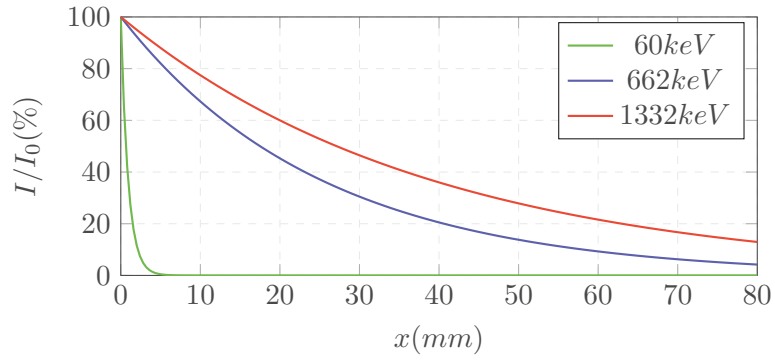

Figure 1.4: Transmission of γ-rays of various energies as a function of the depth of germanium. Data from [2].

influence on the final response of the detector, mainly in the low energy range. The Compton continuum shape gives an information about the detector environment.

Pair creation does also affect the spectrum shape. Depending whether both 511 keV photons are absorbed in the Ge crystal or only one of them or none of them, the full-energy peak, the fist-escape peak or the second escape-peak will be incremented, respectively. These 511 keV γ-rays may also Compton scatter and generate continuous background between and below these peaks. In the same way as Compton scattering, γ-rays can interact with surrounding material, leading to the creation of secondary 511 keV γ-rays which can be detected independently, thus incrementing a 511 keV annihilation peak.

Several complications in the response function can arise, mainly when the γ-ray interaction takes place near the external limit of the detector. Secondary electrons can escape, so that characteristic X-rays produced by photoelectric absorption. In this cases, the deposited energy has a deficit and does not contribute to full energy measurement independently from the detector performances.

1.1.6 γ-ray attenuation in matter

The total cross-section for a γ-ray interaction in matter is the sum of the cross-sections from each effect described above:

$$\sigma_{\text{total}} = \sigma_{\text{photoelectric}} + \sigma_{\text{compton}} + \sigma_{\text{pair}} \tag{1.5}$$

It depends mostly on the atomic number of the absorber material and on the energy of the incident γ-ray, but although on the density of the material. The transmission of a γ-ray through a material of thickness x follows an exponential decay law:

$$\mathrm{I} = \mathrm{I_0 e^{-\mu x}} \tag{1.6}$$

where μ is the linear attenuation coefficient. As we have seen in the previous sections, all interaction processes are strongly correlated with Z and material density. The atomic number of silicon and germanium are respectively 14 and 32, which makes germanium a material more efficient for the radiation detection in the mid- to high-energy range. Further work will focus

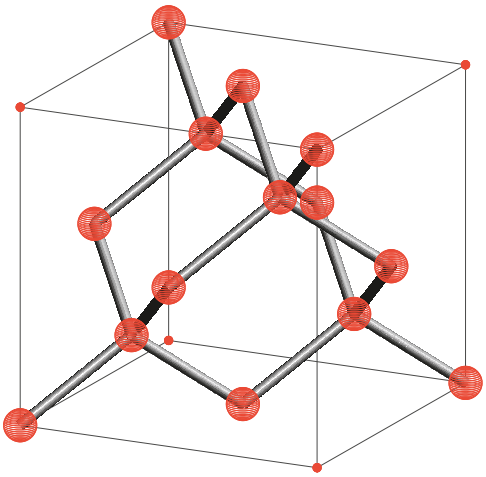

Figure 1.5: Face-centered cubic lattice structure of germanium, silicon and diamond. Each atom has four covalent bonds with four neighboring atoms.

on ^{241}Am and ^{137}Cs radioactive source measurements, with characteristic γ-ray energies of precisely 59.5 keV and 661.7 keV, respectively. These values will be shorten to 60 and 662 keV in the rest of this document. The transmission for photons with these energies in germanium is plotted in fig. 1.4. As all 60 keV photons are absorbed in few millimeters, measurements performed with the ^{241}Am source are probing the near-surface of the detector. About 5% of 662 keV photons are able to cross more than 80 mm of germanium, so that ^{137}Cs measurements are sensitive to the whole detector volume. Nevertheless, a ^{137}Cs source placed in front of a detector will generate much more interactions in the front than in the back of the detector. This will have an impact on statistics discussed in the experiments described in the following.

1.2 Semiconductor detectors

1.2.1 Band structure in semiconductors

In crystalline solids such as germanium, atoms are arranged in an underlying structure where electrons are shared in covalent bondings. Silicon and germanium share the same face-centered-cubic periodic lattice as diamond, which is shown in fig 1.5. This pattern is repeated indefinitely until the crystal boundaries to form a mono-crystal. In this lattice, the allowed energy levels for any electron are no longer discrete as in isolated atoms, but confined in large energy bands. The last filled band corresponds to the electrons of the outer-shell of the atom which is called the *valence band*. The next-higher lying band is called the *conduction band*. These two bands are separated by a gap E_g corresponding to forbidden energies. The size of this gap characterizes the resistivity of a material as shown in fig 1.6.

In conductors, the valence band is not full, allowing electrons to move freely in the material. For insulators, the valence band is full, such that electrons have no free energy levels available. Furthermore, the gap is so high that, from an energetic point of view, there is no possibility for an electron to leave the valence band. Semiconductors are a special case of insulators with low band gap: at zero Kelvin they behave as insulators. However, if some

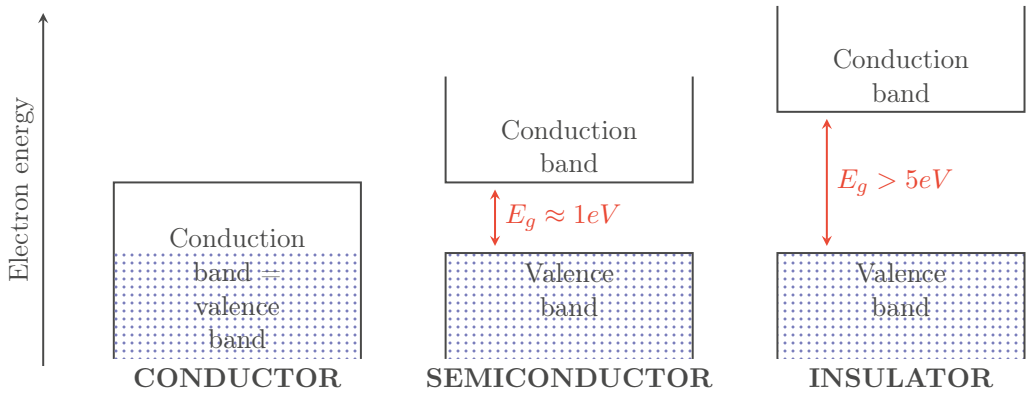

Figure 1.6: Band structure for electron energies in conductors, semiconductors and insulators.

electron get sufficient energy, e.g. thermal energy, the low gap allows them to cross the forbidden band to the conduction band, leaving behind them a vacancy in the valence band which is called a *hole*. Then, electrons from the conduction band can move, and electrons from the valence band can jump from a vacancy to another (in other words, holes are moving too). Both electrons and holes are participating to the global conduction of the material. Because of the non-zero temperature, thermally generated electron-hole pairs will always be present in semiconductors, following this equation:

$$\mathrm{p(T)} = \mathrm{C} \cdot \mathrm{T}^{\frac{3}{2}} \cdot \mathrm{e}^{\left(-\frac{\mathrm{E_g}}{2\mathrm{kT}}\right)} \tag{1.7}$$

where T is the temperature, $\mathrm{E_g}$ is the band-gap energy, k is the Boltzmann constant and C is a constant depending of the material. Germanium has a low gap of 0.66 eV, such that the crystal is saturated with thermal carriers at room-temperature. Germanium detectors have to be cooled typically at 77 K, i.e. liquid nitrogen (LN2) temperature, in order to remove this thermal contribution.

1.2.2 Crystal doping

Modern refining techniques allow to produce germanium crystals with very high purities. Such material is called high purity germanium, or HPGe. However, there are still few impurities remaining which are various unexpected atoms in the crystal lattice. Their concentration is typically in the range 10^{10} cm^{-3}, which is equivalent to one impurity atom for about 10^{14} germanium atoms. If an impurity occupies a substitutional site, i.e. if it replaces one periodic atom, it introduces a discrete energy level close to the conduction or to the valence band, depending of the impurity type. Such levels allow the creation of electron-hole pairs with very little energy compared to intrinsic pair generation. Germanium has four valence electrons. A pentavalent atom carries one electron in excess compared to the surrounding matrix. It is then a negative impurity, also called n-type impurity. It creates a donor level near the conduction band. This electron is easily available to contribute to the conduction. Reversely, a trivalent impurity or p-type impurity, has a lack of one electron which creates an acceptor level near the valence band. Thus valence electrons can easily move to this levels and leave a hole. These processes are shown in fig. 1.7.

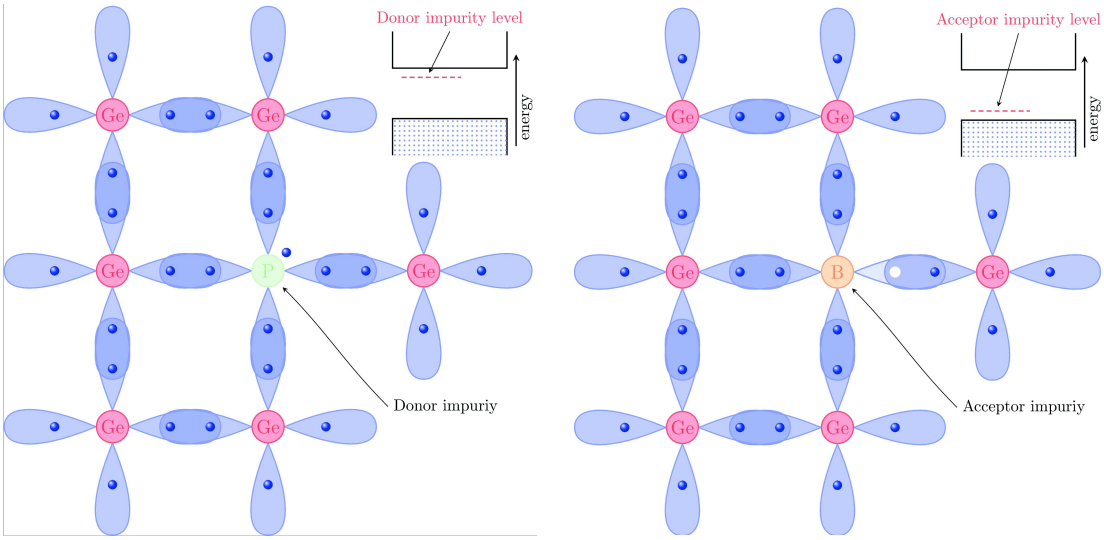

Figure 1.7: Effect of crystal doping on the electronic behavior of semiconductors

1.2.3 Reverse biased PN junction

Crystal doping can be monitored with chemical and physical processes, in order to modify the semiconductor behavior. For example in HPGe:

- a lithium diffusion on the crystal surface creates a n-type semiconductor with the addition of a supplementary electron, the thickness of the doped material with such process is usually considered to be ~ 500 μm,
- a boron implantation creates a p-type semiconductor because it is trivalent, the doping profile has ~ 0.5 μm thickness.

When a semiconductor has a p-type region in contact with a n-type region, a PN-junction is created with favorable properties for radiation detection. Excesses of holes and electrons due to doping are attracted due to their opposite charges and the system tends to an equilibrium with the drift of free carriers. Electrons from the n-side move to the p-side, attracted by holes opposite charges. Reversely, holes from the p-side move to the n-side. Most part of these moving charges disappear with electron-hole recombinations. The moving electrons and holes are leaving immobile charges in the form of ionized impurities, respectively positive and negative. Therefore, there is a net negative space charge on the p-side and a net positive space charge on the n-side, creating an electric potential difference that reduces the probability of further diffusion until zero when enough charges have been moved. This process is shown schematically in fig. 1.8. The value of charge potential ϕ in the junction can be found by resolving Poisson's equation :

$$\nabla^2\phi = -\frac{\rho}{\epsilon} \tag{1.8}$$

where ρ is the net charge density and ϵ is the dielectric constant of the material. This potential difference leads to variations in the electric field following:

$$\mathcal{E} = -\nabla\phi \tag{1.9}$$

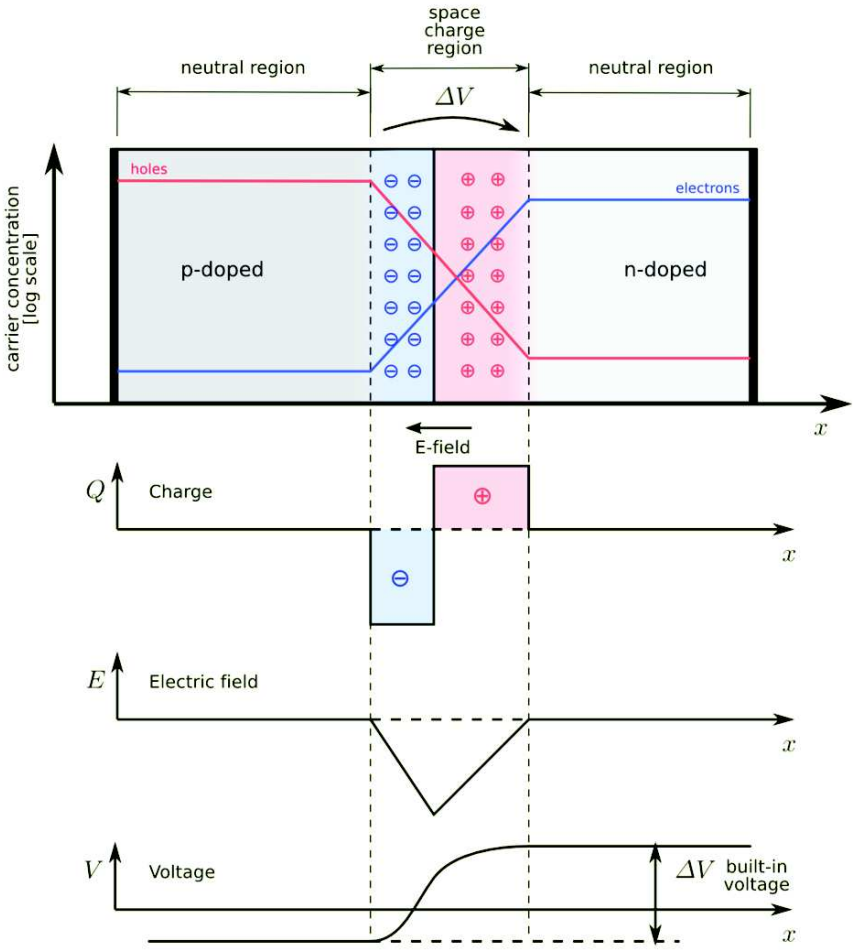

Figure 1.8: Principle of a PN junction with corresponding space charge Q, electric field E and electric potential V.

In the middle of the junction, the region with no more charge carriers is called the depleted region. It exhibits very attractive properties for radiation detection. Any charge created in this region is accelerated by the electric field, toward the n-type or p-type material in case it is an electron or a hole, respectively. The size of the depleted region can be significantly increased when the p-side and the n-side of the PN junction are separated with a large intrinsic semiconductor region. It is then a PIN diode with a very large intrinsic volume. The external surface of both p-type and n-type regions are metalized in order to measure the resulting signals on these electrodes. The naturally generated potential (ΔV in fig. 1.8) at the PIN junction is so weak that the depleted region is small and just a fraction of the volume can be used as radiation detector. A reverse bias is then applied to the junction, which corresponds to an increase of the natural potential difference. The magnitude of this bias voltage is typically of a few thousands volts, depending on the size of the crystal and on the impurity concentration. The effect is that the size of the depletion region increases to reach the full crystal volume is expressed in eq. 1.10, which is an analytical solution of the depletion depth for a planar configuration:

$$\mathrm{d} = \left(\frac{2\epsilon \mathrm{V}}{\rho}\right)^{1/2} \tag{1.10}$$

with d the depletion depth and V the bias voltage. This equation shows that high-purity material (low ρ typically about 10^{10} cm^{-3}) is necessary to deplete large volume crystals.

1.2.4 Charge collection

Any energy deposit in the semiconductor leads to the production within few nanoseconds of a cloud of carriers with equal number of electrons and holes. If they are generated in the depletion volume of a PIN junction, these charges undergo two major effects:

- a random thermal motion which leads to the diffusion away from their origin point,
- the influence of the electric field.

As a result they drift and spread within the depleted region from their creation location to the junction boundaries, driven by the electrical field orientation. The amount of charges collected is proportional to the energy deposit and it is necessary to collect all of them. A pulse height analysis of the output signal allows to generate a γ-ray spectrum where the numbers of detected counts are plotted as a function of their energy.

Charges drift with a velocity ν. For moderate electric fields, the velocity is proportional to it such that a mobility μ can be defined for both electrons and holes as follows:

$$\nu_{\mathrm{h}} = \mu_{\mathrm{h}} \times \mathcal{E} \tag{1.11}$$

$$\nu_{e} = \mu_{e} \times \mathcal{E} \tag{1.12}$$

While increasing the electric field $\mathcal{E}$, the drift speed behavior is getting more complex. An empirical parametrization has to be used [1], which has the form:

$$\nu_{\mathrm{l}} = \frac{\mu_0 \mathrm{E}}{(1 + (\mathrm{E}/\mathrm{E}_0)^{\beta})^{1/\beta}} - \mu_{\mathrm{n}} \mathrm{E} \tag{1.13}$$

where ν_l is the velocity along the crystallographic axis l, μ_0, β and E_0 are adjustable parameters fitting the experimental data. The term μ_nE accounts for the Gunn effect (for very high electric fields, the mobility decreases as the electric field is increased). For high electric-field intensity variations ($\sim$ 1000 V/cm), the velocity does not increase significantly anymore: a saturation velocity is reached which is about 100 μm/ns. Detectors are usually operating with a bias voltage large enough to reach the saturation drift velocity in most of the depleted volume, in order to optimize the charge collection process.

In practice, crystal imperfections such as dislocations, radiation damages and impurities can behave as electron-hole recombination centers or trapping centers. In the first case, charges either positive or negative, tend to be attracted to the same point, inducing their recombination. In the second case, charges are trapped in defects with energy levels placed deeply in the band gap. Each type of impurity has its own trapping time-constant and releases trapped charges following an exponential decay probability. Therefore, during the collection process, carriers are trapped for a time scale which is typically longer than the specific measurement time scale, i.e. the integration time, so that they do not contribute to the final measurement. These events undergo pulse-height defects and the result on the final spectrum is a low-energy tailing of the full-energy peak. In the worst cases, this can be redhibitory for fine spectroscopy.

The electric-field distribution inside the volume, combined with the crystal anisotropy, leads to drift time values depending on the location of the initial charge production. This is of prime importance because, as a consequence, the output signal has a rising edge varying with the location of the γ-ray interaction in the crystal. This property is used for γ-ray tracking devices such as AGATA [4] and GRETINA [5]. Investigations are ongoing on several new detector geometries with small(long) drift speed(path) [6, 7], where the charges drift speed does not reach necessarily saturation. Such behavior allows to push forward the interaction-position sensitivity in these detectors.

1.2.5 Anisotropic mobility behavior

The drift velocity of charge carriers depends mostly on the electric-field strength. The effective behavior is somehow more complex and, as a result of the crystalline anisotropy, the mobility vector is neither collinear nor proportional to the electric-field vector [8]. Energy levels allowed for free charge carriers moving through the material are located in specific low potential regions. At a macroscopic scale, the apparent trajectory is bent in order to drift only in authorized levels, reaching the electrode with a longer drift time.

The anisotropy is split in longitudinal and tangential components which give the drift speed and the tilt between the orientation of both the electric field and charge drift. The effect of the mobility anisotropy is demonstrated in fig. 1.9 which shows the influence of electric field upon charge velocities, along the three main crystallographic axes. The <100> axis is the fastest, while the <111> is the slowest for both electron and holes. The velocity saturation behavior of electrons for high electric field is obvious.

An example of the tangential anisotropy is depicted in fig. 1.10. Both electric field and drift directions are tilted with an angle Φ depending on the electric field orientation along the crystallographic axis. This tilt can reach almost 20° for electrons. Such behavior has relevant effects on drift trajectories.

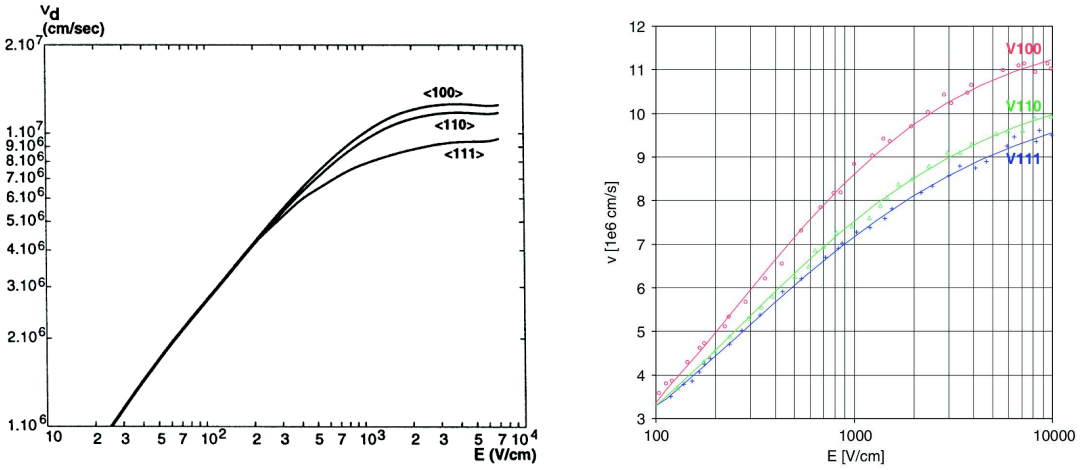

(a) (b)

Figure 1.9: Charge drift velocity along the 3 main crystallographic axes for: (a) Electrons (figure from ref. [9]) and (b) Holes (figure from ref. [8]).

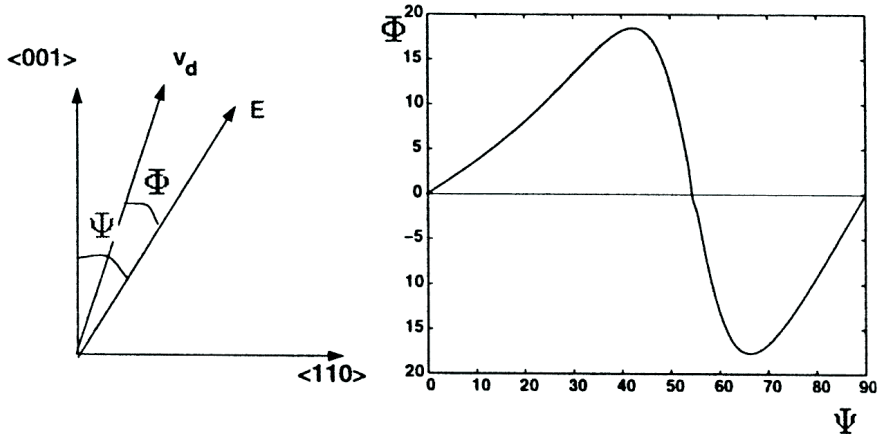

Figure 1.10: Electron tangential anisotropic effect in one crystal plane. Ψ is the relative angle between the electric field vector and the crystallographic direction <100> and Φ is the resulting angular shift (the tilt) between the drift velocity and the electric-field vector. Figure from ref. [9].

Anisotropic mobility is a complex behavior to parametrize but it results in an additional location information of the output signal shapes.

1.3 HPGe detector and HPGe array characteristics

Local variations of charge collection, integrated over the whole volume of the detector, lead to a global response which is commonly characterized by several parameters.

1.3.1 Detection efficiency

A first criterion to evaluate a radiation detector is to quantify its ability to detect γ-rays with the full energy, i.e. the photopeak energy. The absolute efficiency ϵ_{abs} is given by the ratio:

$$\epsilon_{\text{abs}} = \frac{\text{number of counts in the full–energy peak}}{\text{number of } \gamma \text{ emitted by the source}} \tag{1.14}$$

It depends not only on detector properties but also on the relative position of the detector with respect to the source. This geometric contribution no longer states with the intrinsic efficiency ϵ_{int}, i.e. the number of full-energy counts versus the number of incident γ-ray on the detector solid angle.

$$\epsilon_{\text{int}} = \frac{\text{number of counts in the full–energy peak}}{\text{number of incident } \gamma} \tag{1.15}$$

In a first approximation, both can be related with following equation :

$$\epsilon_{abs} = \frac{\Omega}{4\pi}\epsilon_{int} \tag{1.16}$$

where Ω is the solid angle in steradian subtended by the detector relative to the source.

Another commonly used value is the relative efficiency ϵ_{rel} which is the ratio, given in percentage, of the detector absolute efficiency over the one of a 3×3 inches cylinder of scintillating sodium iodine in specific conditions [10]. It gives a straightforward estimation of the efficiency.

Another characteristic commonly used for γ-ray spectrometer is the peak-to-total ratio, defined as:

$$\text{P/T} = \frac{\text{number of counts in the full–energy peak}}{\text{total number of counts in the spectrum}} \tag{1.17}$$

As the background of the γ-ray detector depends on the surrounding environment, this value is only relevant for a given measurement condition. For a single HPGe detector, the P/T ratio increases with the size of the crystal because the photopeak efficiency increases.

1.3.2 Resolution

A scintillating crystal such as sodium iodine (NaI) has a poor energy resolution, leading to very broad full-energy peaks, which makes it an unsuitable material for fine γ-ray spectroscopy.

In germanium the average energy for the creation of an electron–hole pair is 2.96 eV at 90 K although the bandgap of Ge is only 0.74 eV at 90 K [11]. The energy difference is due to the excitation of lattice vibrations, a process which competes with the creation of electron–hole pairs. Nevertheless a 1 MeV γ-ray undergoing photoelectric effect in germanium generates $\sim 3.4 \cdot 10^5$ electron-hole pairs. The statistical fluctuation for the collection of so many charges is very small, such that the full-energy peak is sharp, allowing to disentangle between very close γ-ray energies. This emphasizes the advantage of germanium detectors over any other type of γ-ray detector for spectroscopy purposes.

The full energy peak has a Gaussian shape which width at half maximum (FWHM) is used to characterize the detector energy resolution. For a monoenergetic γ-ray detected in an HPGe detector, the FWHM, W_T, is due to statistical fluctuation of several parameters :

$$W_T^2 = W_D^2 + W_C^2 + W_E^2 \tag{1.18}$$

where W_D, W_C, W_E are due respectively to variations on charge-carrier creation, charge-carrier collection and electronic noise. The former is intrinsic to the detector material. The two others are to be optimized considering the measurement to perform. Small-volume detectors have a better overall energy resolution than larger due to their lower capacitance and lower charge drift distance, which lead respectively to lower electronic noise and lower trapping-induced pulse height defects.

1.3.3 Short review of γ-ray spectrometers

Fundamental research in nuclear physics aim to study structures or exotic nuclei with very low production cross-sections. Experimental conditions which vary case by case are listed below:

- intense ion beam leading often to high count rates (up to 25 kHz per crystal and beyond),
- large recoil velocity of the emitting nucleus inducing large Doppler broadening effect,
- large γ-ray multiplicity (20 or more) leading to pileups.

Time coincidence between two or more detectors enables the identification and selection of γ-ray cascades hence to build level schemes.

Since the seventies, configurations with at least two germanium detectors were commonly used in coincidence for γ-ray spectroscopy. To gain in detection efficiency detectors were placed close to the target. In such configurations, two γ-rays emitted simultaneously are likely to interact at the same time in a single crystal, resulting in a summed-energy readout (or pileup) which contributes to the background. The probability for such event to occur can be decreased by placing the HPGe detectors farther from the target, thus decreasing their solid angle and the absolute efficiency of the experimental setup. This efficiency loss can be compensated by gathering more and more crystals around the target chamber. A worsening side effect of such set up is that a single γ-ray scattered between several detectors will on the one hand, contribute several times to the background in the final spectrum, and on the other hand, result in a fake γ-γ coincidence. The final spectrum has a large background, such that any rare event will emerge barely or even not at all from the continuum.

A first improvement to reduce the background in γ-ray spectra is to use escape-suppression shields. The HPGe is surrounded with scintillators with only one hole provided for the entrance of γ-rays (see top panel of fig. 1.11). Gamma-rays scattered out of the HPGe have a large probability to interact with scintillators. Their signal is used as a veto for these events which are not incremented in the HPGe spectrum. This process results in a large decrease of the Compton background (about a factor 3 less), as shown in the bottom of fig. 1.11, and therefore in a large increase of the P/T ratio. Suppression shields were introduced in the seventies and national multi-detector arrays composed of 6, 12 and up to 20 germanium crystals each surrounded by suppression shields were built in the eighties [12]. In the second half of the eighties, an increase in the full energy efficiency of the germanium detectors was

obtained by the production of larger size crystals with relative efficiencies rising from 20% up to 70%. In the early nineties, large germanium arrays were constructed such as EUROGAM I and II [13], EUROBALL [14] and GAMASPHERE [15]. They were made of several HPGe crystals (50, 126, 239, 110, respectively) surrounded by suppression shields. The issue with such a configuration is that the solid angle covered by HPGe is limited to ∼45%, the remaining part being occupied by escape-suppression shields.

1.3.4 Doppler broadening

Another challenge of fast ion beam collisions on target is that, in most experiments, the recoiling nucleus emitting γ-rays is moving at high velocity. If its speed $\beta = \mathrm{v/c}$ reaches a relevant fraction of the speed of light, γ-rays are subject to Doppler effect. A nucleus in the situation shown in fig. 1.12 with velocity β, emitting a γ-ray with energy $\mathrm{E_0}$ at an angle θ compared to the recoil direction has a measured energy $\mathrm{E_\gamma}$ as follows:

$$E_\gamma = \frac{E_0}{\gamma(1 - \beta cos\theta)} \tag{1.19}$$

where $\gamma = 1/\sqrt{1-\beta^2}$ is the Lorentz factor. A detector placed at forward (backward) angles measures a higher (lower) energy than $\mathrm{E_0}$. This can be corrected with the relative position of the detector, but the finite solid angle $d\theta$ of the detector results in a full-energy peak broadening as follows :

$$\delta E_\gamma = E_0 \cdot \beta \cdot \sin\theta \cdot d\theta \tag{1.20}$$

The peak broadening is largest at 90° relative to the beam direction, because detectors in this position are detecting a continuum of forward and backward emission. The only solution to avoid peak broadening is to reduce the apparent solid angle of the detector at 90°, which allows a more accurate correction. The detector has to be placed farther from the target or it should be electrically segmented.

1.3.5 Composite detectors and segmentation

An array dedicated for nuclear spectroscopy needs to have a large efficiency, high granularity, high throughput and high sensitivity i.e. the ability to detect a peak over the Compton continuum. Composite Clover detectors [16] were developed during the 90's with the main goal to improve Doppler correction. They are based on four 25% relative efficiency HPGe crystals, clustered in one cryostat and working in add-back mode, i.e. when several crystals are triggered simultaneously, their energies are summed and increment in a single add-back spectrum. The add-back applied to these four crystals allows to reach 130% relative efficiency for the whole detector. Due to the small size of crystals, their solid angle is reduced, thus reducing the Doppler-broadening of peaks. That's why these detectors were placed at 90° relative to the beam direction. These detectors are highly reliable and they are less sensitive to radiation damage than large volume detectors due the small size of their crystals, such that they became a standard in the γ-ray spectroscopy research field. Their original design allows to use them also as γ-ray polarimeters [17]. Several other developments concerning HPGe

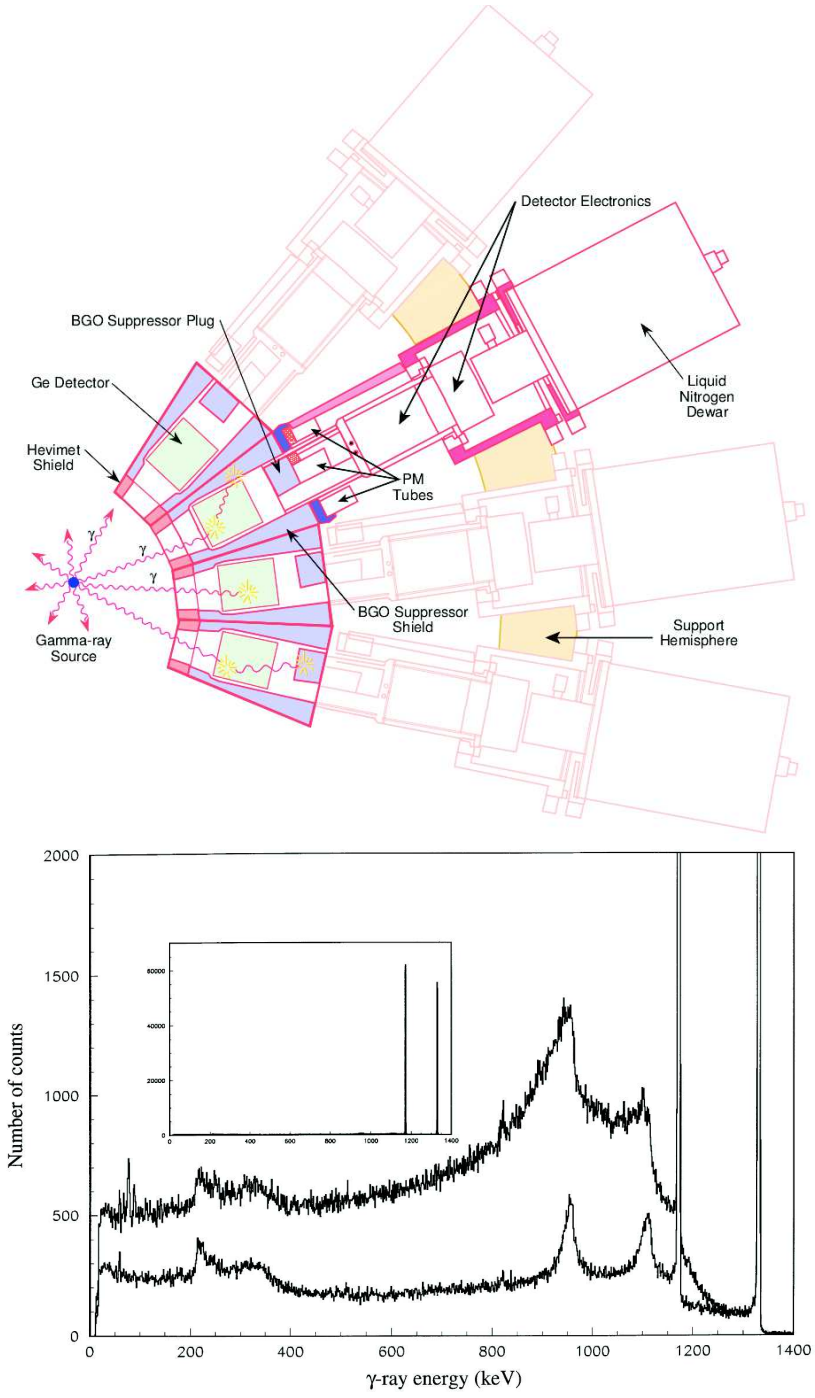

Figure 1.11: Principle of an escape-suppression array (top panel). Gamma-rays scattering from HPGe crystals to their escape-suppression shields are detected due to HPGe-scintillator coincidences. These events are vetoed and not recorded in the γ-ray spectrum (bottom panel [16]), thus drastically reducing the Compton continuum of the spectrum. The final P/T ratio is substantially improved.

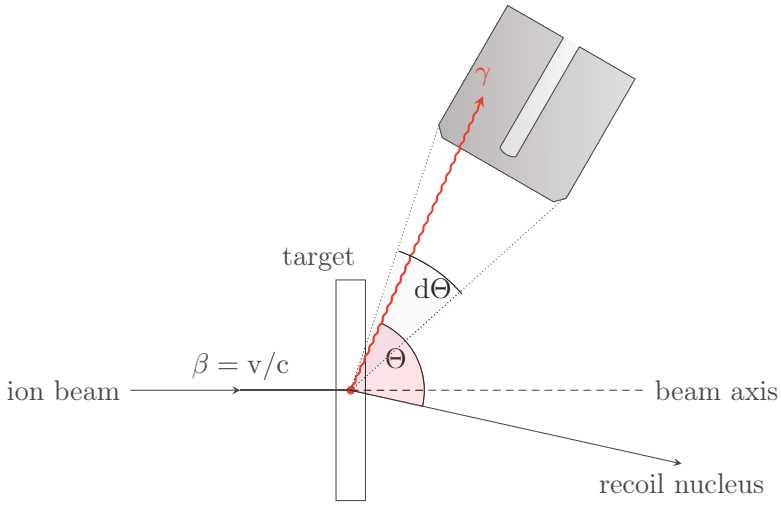

Figure 1.12: Doppler broadening

technologies emerged such as crystal encapsulation [18] which allows an easier maintenance by protecting the HPGe crystal in a sealed aluminum canister. It facilitates the construction of composite detectors such as EUROBALL cluster detector [19] composed of 7 large volume, encapsulated crystals and the MINIBALL [20] triple cluster composed of three large volume, encapsulated, 6 or 12-fold segmented crystals.
A breakthrough arose with HPGe segmentation [21] which allowed to reach another step in the granularity of the whole array. The crystal is electrically divided in several subsections called segments, each of them having a solid-angle smaller than the whole crystal. N-type crystal segmentation consists of implanting boron on the external surface with a specific 2D-pattern which creates several electrodes instead of a unique one. Holes are then collected in segments. The hit segment gives a direct information about the interaction location. Electrons are all collected on the n+ Li-contact, called Core, which has the full energy information of the crystal. This huge potential for Doppler broadening correction has been used in several arrays dedicated to low-multiplicity, high velocity in-beam measurements such as EXOGAM [23], MINIBALL [20] or SeGA [22]. By using segmentation coupled with digital electronics, the analysis of the leading-edge shape of output signals lead to localize the first interaction with a sub-segment precision. Such behavior triggered the idea of an array able to perform γ-ray tracking such as a HPGe shell.

1.4 The AGATA spectrometer

The full-energy, absolute detection efficiency of EUROBALL and GAMMASPHERE, about 0.10, was the upper limit of Compton-suppression shield technique for high-spin physics and EXOGAM and TIGRESS [24] with 0.15-0.20 for exotic nuclei studies. In the second half of the nineties, a new concept arose, the γ-ray tracking, supposed to be a breakthrough in detection efficiency and Doppler broadening correction. A position-sensitive HPGe array allows to track the γ-ray path in germanium, and then to sum partial energy deposits due to

multiple Compton scattering even in the case of scattering between several crystals. Escape-suppression shields are then no more necessary, the large fraction of solid-angle that they occupy is replaced by additional HPGe detectors. In a tracking array, events where a γ-ray scatters between two crystals and is fully absorbed in germanium, if properly reconstructed, will neither contribute to the background nor be rejected. The partial energy releases in both crystals are summed leading to a full-energy detection and Compton background reduction. The P/T ratio is then increased. In the same time, the accurate localization of the first γ-ray interaction, within few millimeters, allows to perform the best Doppler correction ever done for an in-beam HPGe array. That is the purpose of the European project Advanced GAmma Tracking Array AGATA [4], as well as GRETINA [5] in the USA.

1.4.1 Capsule description

AGATA detectors are complex. They consist of large n-type, tapered, coaxial HPGe crystals, combined with state-of-the-art segmentation and encapsulation technologies. Each specific parameter is the result of a design trade-of to reach optimal performances :

- **Coaxial** design allows to have a compact and thick HPGe shell. The efficiency is maximized for high-energy γ-ray, thanks to the large amount of germanium material gathered. It minimizes also the amount of inert material within the solid angle of the array, which is necessary for holding, cooling, biasing and get the signal of each crystal. These support functions are placed out of the HPGe shell.
- **N-type** HPGe crystals are preferred to p-type for fundamental research, because of their lower sensitivity to neutron damage and also their thin entrance window offering better spectroscopic performances for low energy γ-ray.
- **Tapering:** the tapered irregular-hexagonal shape of the front part of the crystals is designed to fit into a geodesic tiling, offering the best solid-angle coverage for the 4π array, in the case of AGATA, 82% of 4π steradian. Although it reduces the relative efficiency of single crystals, it allows an enhancement of the array efficiency.
- **Segmentation pattern:** the configuration of segments is optimized to have large pulse-shape sensitivity with the minimum number of readout channels.
- **Encapsulation:** because HPGe surfaces are very sensitive, crystals are encapsulated and sealed within a protective aluminium canister. It makes any handle of crystal easier and safer. As a result, the setup of the whole array is more reliable.

AGATA crystals have a length of 90 ± 1 mm and a diameter of $80^{+0.7}_{-0.1}$ mm at the rear. At the front they are tapered to a hexagonal shape with a 10° tapering angle. The crystal bored hole has a diameter of 10 mm and extends to 13 mm from the front end. The external segmentation pattern is shown in fig. 1.13.

The 6-fold sector-wise, longitudinal segmentation goes through the middle of each flat hexagonal side, parallel with the bored hole. On the front face, the 6 segmentation lines cross at the center of the hexagon. Figure 1.13(a) shows the relative positions of the sections and their labels (A-F) viewed from the rear of the crystal. In the rest of this document, figures show the sectors with the same orientation as in fig. 1.13(a). The 6-fold transversal external segmentation forms slices of 8, 13, 15, 18, 18 and 18 mm in thickness starting at the hexagonal

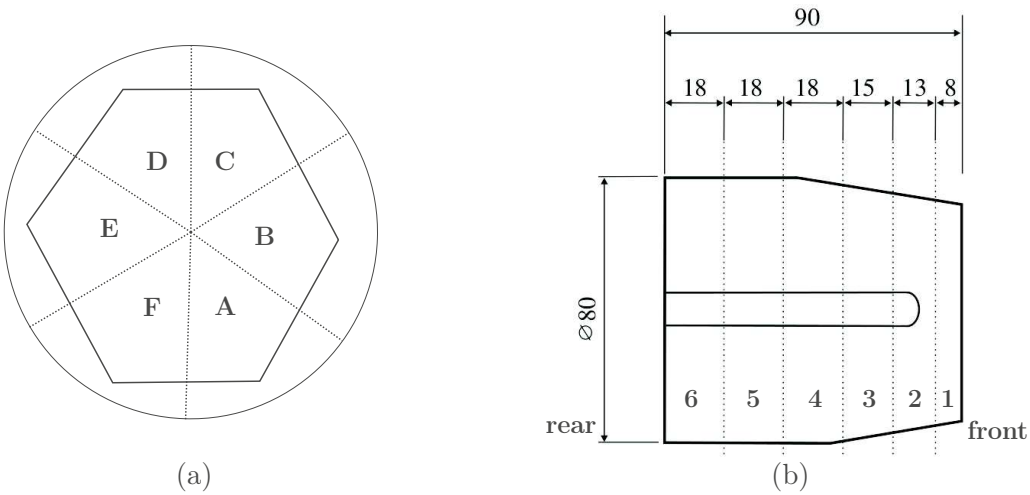

(a) (b)

Figure 1.13: (a) Radial segmentation of the front face of AGATA crystals, viewed from the rear of the crystal. Segmentation lines are going from the center to the middle of each flat hexagonal side. They continue from the front to the rear of the crystal, parallel to the bored hole and are called longitudinal segmentation (b) External transversal segmentation of AGATA crystals.

front face of the crystal and labeled 1 to 6 (see fig. 1.13(b)). The thickness of the slices have been optimized for a uniform distribution of γ-ray interactions and optimal pulse-shape sensitivity [25]. Segmentation lines have a nominal width of 500 μm. Both transversal and longitudinal segmentation lines divide the crystal into 36 segments with 6 slices of 6 sectors. The bored hole n+ contact collects signal coming from interaction in the whole volume. The corresponding electronic channel is called *Core*. Signals are extracted through vacuum feedthroughs at the rear of the canister, where PCB plates supporting the cold-FETs (first stage of preamplification) are mounted.

1.4.2 AGATA array

AGATA is a shell of HPGe detectors as described above. The whole array is made of 180 HPGe crystals covering 82% of the 4π solid angle. The spherical tiling is achieved with the use of three different crystal shapes, with irregular-hexagonal sections. These crystal shapes are labeled as A-type (red), B-type (green) and C-type (blue). Three crystals, one of each type, are gathered in a single cryostat called triple-cluster [26]. It holds the 3 crystals, cool them to LN2 temperature and also supports the first and second stages of signal preamplification. The whole configuration for in-beam experiments is depicted in fig. 1.14.

Once the array triggered, several γ-rays may interact. Both energy and pulse shapes for all segments and for the Core of each hit crystal are registered with a specific 14-bit, 100 MHz digital electronics. These data undergo the following analysis:

1. Pulse Shape Analysis (PSA): each experimental pulse shape is compared to a database of simulated pulse shapes, i.e. a signal basis, covering the entire volume of the crystal

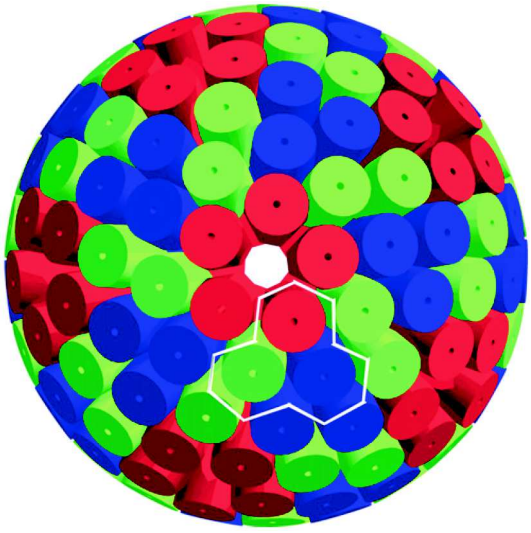

(a)

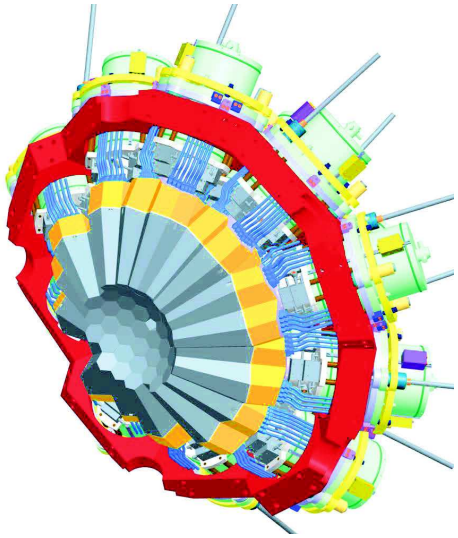

(b)

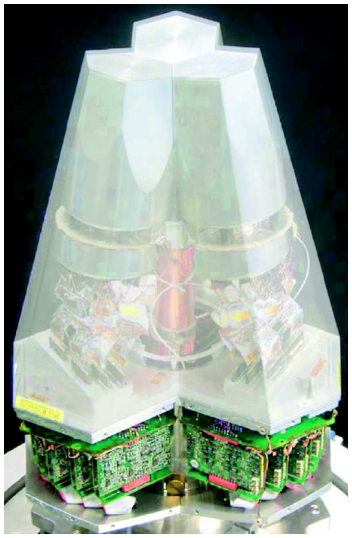

(c)

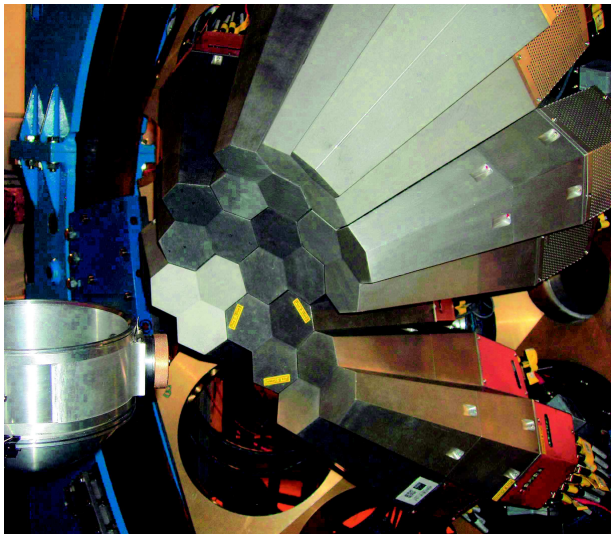

(d)

Figure 1.14: AGATA configuration concerning : (a) crystals packing of the full 4π array, (b) the complete 1π configuration including the material required for support functions, (c) three irregular-shaped crystals and their front-end electronic inside a triple cluster [26], (d) the AGATA spectrometer for the GANIL phase during summer 2015, with 8 triple clusters and 24 crystals.

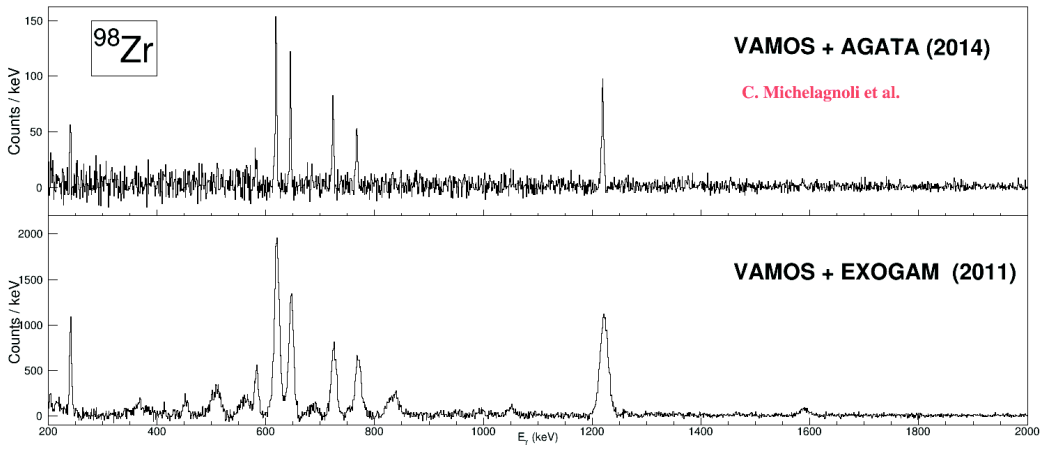

Figure 1.15: Comparison of AGATA and EXOGAM spectra obtained in the same conditions. Both γ-ray arrays are coupled to VAMOS placed at 20° relative to the beam direction. The γ-ray spectra are gated on ^{98}Zr produced in the ^{238}U(6.5 MeV/A)+^{9}Be fusion-fission reaction during an EXOGAM experiment and a short AGATA commissioning run. Courtesy of C. Michelagnoli, the VAMOS collaboration and the AGATA collaboration.

following a 2 mm pitch grid. Signals from the basis which are most similar to experimental one enable to assign a spatial position of interaction [27, 28].

2. Clustering: the distribution of all interaction points of one event (one trigger) is analyzed in order to cluster points which are likely to result from a single γ-ray [29]. One event is likely to gather several clusters due to the γ-ray multiplicity.

3. Tracking: for each cluster of interaction points, all possible interaction sequences, each corresponding to a multi-Compton scattering path of the photon, are analyzed. A figure of merit is attributed to each sequence. It takes into account the physical probability for such sequence to occur [30, 31, 32, 33]. At the end, partial energy deposits corresponding to the most probable sequence are summed and incremented in the experimental spectrum.

An example of improvement obtained with AGATA over other arrays is given in fig. 1.15, which shows the results of a commissioning run. AGATA is coupled with the spectrometer VAMOS. Using the ^{238}U +^{9} Be fusion-fission reaction with VAMOS placed at 20° relative to the beam direction, light fission fragments are detected and identified (A,Z) in VAMOS while γ-rays are detected in AGATA in a preliminary configuration of nine crystals. Zirconium is one of the strongest species populated. Isotope 98 is selected by VAMOS and the coincident γ-rays are shown in fig. 1.15. Despite the modest full-energy detection efficiency and thanks to PSA and tracking performances allowing an excellent Doppler correction (recoil velocity v/c$\sim$12%), the AGATA spectrum quality is obviously better than the one of a two weeks EXOGAM experiment. This lets imagine the capabilities of the complete equipment.

1.5 Role of detector characterization

The entire tracking concept is based on the analysis of output signal shapes of the hit crystals. Only a thorough understanding of the signal formation, taking into account each crystal specificities allows to build simulated signal basis. Both simulated basis and tracking algorithms have been benchmarked with in-beam measurements using AGATA [34]. They revealed several issues to work on:

- the spatial resolution reached with PSA is on average 5 mm FWHM, lower values might be reachable,
- the hit-point distribution in each crystal is not uniform,
- there is a loss of efficiency on tracked spectra compared to what is expected.

Currently, tracking allows a large P/T ratio improvement, with the cost of a loss in efficiency: a lot of events are rejected by the tracking algorithms because they are physically unlikely to happen. An explanation is that the output of the PSA is not proper enough, such that the reconstructed interaction points are not corresponding to the effective history of γ-rays in the shell, hence affecting the tracking algorithm performances.

One main point concerning the quite large PSA spatial resolution is that signal basis are not matching exactly experimental signals, mainly in the front and the rear of the crystals. Possible solutions are to improve pulse-shape simulations using comparisons with precise experimental signal shapes and/or to replace simulated pulse-shapes bases by experimental ones. Due to experimental limitations, an entire experimental signal basis was not a reachable goal until now. The aim of this work is to extend a known but not yet much studied characterization technique [35] which is able to generate an experimental signal basis in reasonable time, i.e. few weeks. It uses a collimated γ-ray beam mounted on a scanning table which can investigate locally in three dimensions the response of HPGe detectors. With such technique, one may consider to establish an individual experimental signal basis for each AGATA crystal.

Other issues could be investigated, which would allow a better understanding of AGATA crystals behavior and, by extension, of segmented HPGe detectors.

Chapter 2

Signal formation and modeling

An operating HPGe detector works roughly as follows:

- A γ-ray interacts within the semiconductor depleted volume and generates a large number of charge carriers (electrons and holes), proportional to the energy deposited.
- The charge carriers move in the crystal from their creation position to the outer electrodes, thanks to the electric field applied on the crystal contacts.
- The charge motion causes variations of the induced charge at each electrode. The current is converted to a voltage pulse using a charge-sensitive preamplifier.
- Carriers are compensated by the induced charges when they reach the electrodes: they are collected.
- The resulting pulse height is proportional to the energy, the pulse shape is related to the trajectory of charge carriers, i.e. it gives an information about the location of the interaction.

The details on these processes leading to signal formation and pulse-shape simulation will be described in this chapter.

2.1 The Shockley-Ramo theorem

The time-dependent output signal of a charge sensitive device can be predicted if the induced charge Q, or the induced current i, on the readout electrode can be calculated as a function of the instantaneous position of the moving charge q in the device. In a HPGe detector, the induced electric signals are the cumulative contributions of moving holes and electrons. The Shockley-Ramo theorem [36, 37] is used to calculate Q(t) or i(t):

$$\mathrm{Q(t)} = -\mathrm{q} \cdot [\phi_\mathrm{w}\left(\mathrm{x_h(t)}\right) - \phi_\mathrm{w}(\mathrm{x_e(t)})] \tag{2.1}$$

$$\mathrm{i(t)} = \mathrm{q} \cdot [\mathrm{E_w(x_h(t))} \cdot \mathrm{v_h(t)} - \mathrm{E_w(x_e(t))} \cdot \mathrm{v_e(t)}] \tag{2.2}$$

where $\mathrm{x_{e/h}(t)}$ and $\mathrm{v_{e/h}(t)}$ are the position and velocity vectors of electron/hole as a function of time, ϕ_w and $\mathrm{E_w}$ are the weighting potential and the weighting field. ϕ_w and $\mathrm{E_w}$ correspond to the electric potential and the electric field existing at the instantaneous position of charge q considering specific parameters which are:

- the readout electrode at unit potential ($\phi_w = 1$),
- all other electrodes at zero potential ($\phi_w = 0$),
- no space charges in the medium.

$\phi_w(x)$ and $E_w(x)$ describe the sensitivity of the electrode versus the relative position x of an electrical charge. The nearest the charge to the electrode, the most intense ϕ_w and E_w and consequently the readout signal. Reversely, if the charge is far from the readout electrode, the resulting signal does not change significantly. It is noteworthy that the value of the weighting potential is independent of both the space charge inside the material and the electrical field, such that its value is determined by geometrical considerations only. Equation 2.1 clearly shows the independence between pulse shape and pulse height: the pulse height corresponds to q while the pulse shape is determined by the weighting potential values along the trajectory of the charges. Two independent γ-rays interacting at the same crystal location will lead to an identical pulse shape, with an height proportional to the energy deposit. In the case of n-type coaxial segmented detectors, the intuitive way is to consider that the Core signal is due to the moving electrons and the segment signals are due to the moving holes. The Shockley-Ramo theorem however proves that it is not that simple, as all charge carriers contribute together to the final readout signal.

By tracking charge carriers from their initial position until their collection with discrete steps, the Shockley-Ramo theorem allows to calculate the signal amplitude at each step, i.e. to generate the leading-edge shape, commonly called the pulse shape. In order to perform such tracking, it is necessary to know :

- the electric-field strength, as well as the carrier mobilities, at the current charge position,
- the weighting-potential value for each readout electrode, in order to determine the readout signal.

2.2 Electric-field and weighting-potential determination

2.2.1 Analytical solution

An accurate calculation of the electric field within the detector is critical. Its value determines the drift velocities and the drift trajectories of the charge carriers, therefore it determines the timing behavior and the charge collection process. In electrostatics, the electric potential ϕ, and its associated electric field $E = -\nabla\phi$, inside a material follows Poisson's law given in eq. 1.8.

In germanium, the relative dielectric permittivity ϵ_r is 16, which corresponds to a permittivity of the material of: $\epsilon = \epsilon_r \cdot \epsilon_0 = 16 \cdot 8.8542 \cdot 10^{-14} = 1.4167 \cdot 10^{-12}$ F $\cdot$ cm^{-1}. The value of the space charge for a fully depleted diode depends on the residual impurities inside the crystal: $\rho = e(N_D - N_A)$ with N_D and N_A the density of respectively the donor and the acceptor impurities. They are usually expressed in cm^{-3}. For n(p)-type semiconductor ρ has positive(negative) values.

For simple geometries where the impurity density is constant, equation 1.8 can be solved analytically. In the case of a true coaxial detector, the electric field value depends on the radius r as follows [1]:

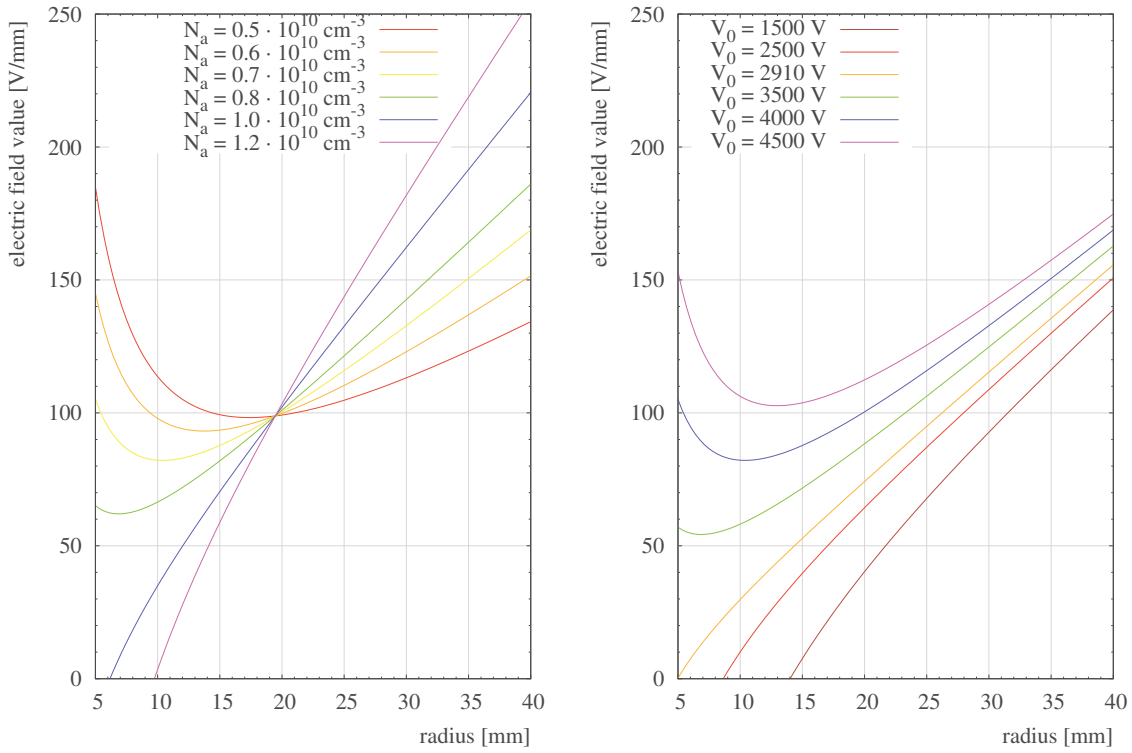

(a) (b)

Figure 2.1: Electric field strength in a true coaxial n-type detector with 5 mm inner radius and 40 mm outer radius, as a function of the cylindrical coordinate r, for (a) several impurity densities N_A with constant bias voltage $V_0 = 4000$ V and (b) several bias voltages with constant impurity density of $0.7 \cdot 10^{10}\text{cm}^{-3}$. In this latter case, the full crystal volume is depleted for a bias of 2910 V.

$$E(r) = \frac{eN_A}{2\epsilon} r + \frac{V_0 - (eN_A/4\epsilon)(r_2^2 - r_1^2)}{r \ln(r_2/r_1)} \tag{2.3}$$

where V_0 is the bias voltage of the detector, r_1 is the inner radius and r_2 is the outer radius. Solutions of this equations are plotted in fig. 2.1 as a function of the radius for various densities of impurities and bias voltages. Panel (a) shows the strong dependency of the electrical field with impurity density. A 10% increase around $0.7 \cdot 10^{10}$ cm^{-3} affects significantly the electric-field distribution and a larger increase can even lead to an undepleted region. The crystal purity and homogeneity are therefore crucial parameters. Due to the growth method of HPGe crystals, the impurity profile shows a gradient marked mostly along the cylindrical axis. This gradient is important to take into account for simulations. Values of the level of impurities at the top and bottom of the crystal are usually given by the manufacturer. One can also expect a gradient along the radius but measurements on AGATA detectors do not show significant radial variations [38].

As shown in fig 2.1, any bias voltage variation around 4000 V within 500 V does not affect the detector performance, as the crystal would stay fully depleted with an electric field strong enough to properly collect the charges. However, any small variation would change significantly the radial electric field profile which modifies the drift behavior of the moving charges, resulting in slight changes on the final pulse shape.

2.2.2 General solution: example

The complex geometry of detectors and the varying space-charge profile force to solve equation 1.8 with a finite-element software. Equation 2.1 is used to determine channel signals because it is easier and faster to compute. Thus, only the weighting potential map is required. Both the electric field and the weighting potentials are considered steady and tabulated for a densely-spaced grid. The electric field is computed once per crystal and weighting potentials are computed once per geometry. Their value at any position are interpolated linearly between neighboring points of the grid. The problem definition takes the following experimental conditions into account: crystal geometry, material electrical properties, space-charge distribution and conditions at the limits. The right boundary conditions are set in order to respect the diode bias and the passivated surface properties:

- Dirichlet boundaries are set on the electrodes; they set the bias voltage of the diode in the central hole and the ground on the outer segments.
- Neumann boundaries are used on the passivated surfaces. They model a perfect behavior with electric potential lines normal to the surfaces.

The weighting potentials of a true-coaxial segmented detector are calculated. The inner radius is 7 mm: this value, larger than real value (commonly 5 mm), was supposed to take into account experimental observations but further work proved that it is not a realistic way to parametrize it. The outer radius is 40 mm and external surfaces are divided azimuthally in 6 segments (A-F) without inter-electrode space, i.e. no passivated surface between electrodes is taken into account in the simulation. The internal electrode (Core) is not segmented, it detects interactions in the whole volume of the crystal.

The Core weighting potential is shown in fig. 2.2(a). It has a non zero value until the extreme limit of external contacts. Equation 2.1 demonstrates that both holes and electrons contribute to the output signal. It means that even when all electrons are collected on the Core electrode, if some holes are still moving near the segment contact or trapped at the surface, it will impact the Core signal with a slight loss on the pulse height. As a consequence, the active detection volume in the detector corresponds to the volume where both electrons and holes are collected efficiently.

The position sensitivity of this detector is illustrated in fig. 2.2(b): an interaction in segment B or F leads to a transient signal in segment A, which amplitude varies from 1% to 40% of the net charge signal, depending on the location of the interaction at a sub-segment scale. This is due to the extension of segment A weighting potential in neighbor segments F and B. Amplitude of the transient signal in A is proportional to the weighting-potential intensity along both electron and hole paths. Even an interaction in secondary neighbors such as segments C and E induces a transient signal but in this case, the amplitude is too low to be significant considering the baseline noise. An interaction in segment D has negligible

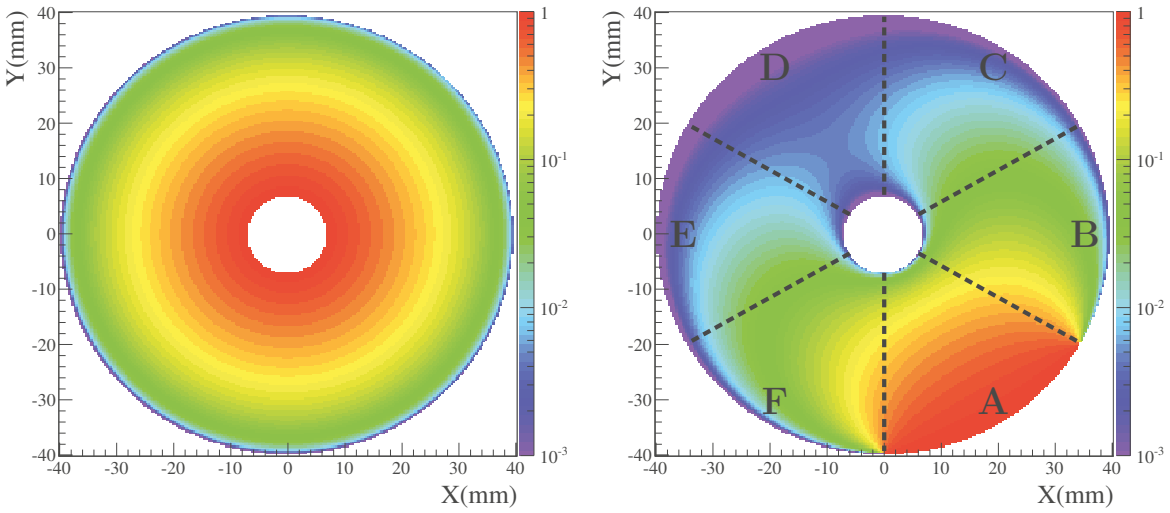

(a) (b)

Figure 2.2: Weighting-potential distributions of the Core (a) and of segment A (b). Calculation conditions are the following: readout electrode at unit potential, all other electrode at zero potential, no space charge inside the material.

influence on A.

2.3 Carrier drift-velocity models

A complete description of electron and hole mobilities can be found in [8]. This parametrization has been used for the pulse-shape simulation work presented here, it is also used to generate signal basis for the AGATA collaboration.

The case of electron-velocity anisotropy was studied since the 60's and is well documented. In the reciprocal space of germanium, free electrons populate only eight half ellipsoidal shaped valleys near the edge of the Brillouin zone, along the four equivalent <111> zones. The effective mobility is the sum of the mobility along each valley, weighted by their relative population which depends itself of an inter-valley electron scattering rate. Unfortunately, past and recent works show that the inter-valley scattering rate may depend on the purity of the germanium crystals. Mobility parameters would then have to be adjusted for each germanium crystal as a function of their impurity concentration gradient. The discrepancies between various independent measurements agree on this statement [8]. Even if the mobility anisotropy model gives coherent results, it matches the experimental data only approximatively.

In the case of holes, it is not possible to directly apply a velocity-anisotropy description identical to electrons, due to the rather complicated mathematical description of the hole valence band near its energy maximum. However, hole-mobility models have also been developed with success [39].

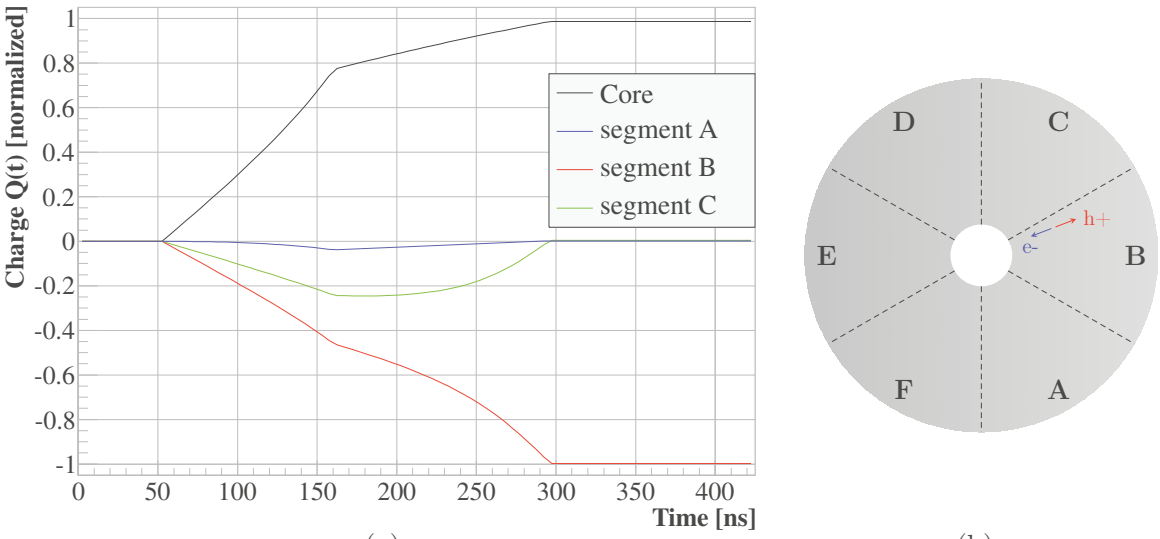

(a) (b)

Figure 2.3: Raw pulses simulated with the simulation code developed in this thesis framework with the following conditions: 6-fold segmented true n-type coaxial detector, inner radius 7 mm, outer radius 40 mm, density of impurity $0.7 \cdot 10^{10} \mathrm{cm}^{-3}$, bias voltage 4000 V.

2.4 Trajectories and pulse shape formation

Each parameter influencing the drift speed of charge carriers has an impact on their trajectories. As a consequence several parameters are involved: crystal geometry, residual space charges density, bias voltage, anisotropic mobility, crystal axis orientation. The carrier path is determined step by step with $\Delta t = 1$ ns steps in this study: charges, electron and hole, are created at the same desired initial position. The local electric field is evaluated, then the velocity vector is calculated for both charges. Each charge is moved towards the real drift direction, by the distance traveled during Δt. The iteration is then performed again until both charges reach the detector boundaries.

At each computed step of the trajectory, Q(t) is determined for each electrode using equation 2.1. Figure 2.3 gives an example of simulated pulse shapes. An electron/hole pair is placed in a random position in the detector at t=50 ns. The charges drift independently. As expected, two behaviors arise: the Core (black line) and the hit segment (red line) pulses have a non zero charge value at the end of the timescale, corresponding to an energy deposit, whereas the neighboring segments have a null final charge, corresponding to a transient signal (blue and green lines). As the induced charge in segment C is larger than the one of segment A, the trajectories of both electrons and holes are located in the hit segment towards segment C. The Core and hit segment pulses have opposite signs as they collect charges of opposite sign. As the electrons are moving towards the Core and as the Core weighting potential increases from the outer to the inner of the crystal, the Core pulse shape is mostly driven by the electron trajectory. Reversely, as segments collect holes, their pulse shape is mostly driven by the holes trajectory. Since the charge collection times are not the same because of

differences in drift distances and carrier mobilities, one of the two contribution stops earlier, leading to the elbow in the Core and hit segment signals, and to the change between rising and decreasing amplitudes in the induced pulses. That is what is observed on the kink at t=160 ns. Electrons are collected while holes are still in motion. Similar information are obtained by measuring the amplitudes and slopes of induced pulses in top and bottom segments.

In the following sections, the segment-pulse amplitudes will always be inverted, in order to make any further pulse-shape filtering more homogeneous.

A simulation in such environment exhibits an ideal behavior. Several experimental effects are not taken into account:

- **Charge sharing:** in the case of a real energy deposit, a great number of electron-hole pairs are created inside the germanium. They behave as a charge cloud moving inside the material. In the case of a segmented detector, at the segment boundaries, this cloud can be split between two neighboring electrodes, resulting in a charge sharing between segments. Thus, a single energy deposit can be seen as a two-fold event.
- **Recombination centers:** some defects act as deep potential levels for both holes and electrons. If one of these defect trap charges of opposite sign, they will recombine and disappear, which leads to a bump in the pulse shape and a charge missing in the pulse height. This exists in HPGe although it is negligible for good detectors.
- **Trapping centers:** other defects are low potential levels which trap the charges during a mean time and then release them. If the trapping time is long enough it can affect the pulse shape, as in the case of neutron damaged detectors [40].
- **Passivated surfaces:** surface treatments on passivated surfaces may generate dead layers or even surface channel where charge carriers are moving in the near-surface of the crystal with a mobility roughly 0.1 times the one of the bulk [41, 42, 43].

2.5 Electronic response

2.5.1 Signal preamplification

The small amount of charges induced on the detector electrode has to be amplified, converted into a voltage, and in the same time its leading edge shape has to be conserved. In semiconductor-diode detectors, the detector capacitance may change with temperature. In this situation charge-sensitive preamplifiers have to be used rather than voltage-sensitive ones.

The principle of a charge-sensitive preamplifier is depicted in fig. 2.4. Putting a charge Q_{in} at the input will result in an output voltage change of:

$$U_{out} = -\frac{Q_{in}}{C_f + \frac{C_D + C_{in} + C_f}{A}} \simeq -\frac{Q_{in}}{C_f} \tag{2.4}$$

which for large amplification is given by the ratio of signal charge over feedback capacitance, indicating the fact that the charge has been transferred completely from the detector to the feedback capacitor. The output signal decreases following an exponential decay given by the feedback circuit $\tau = R_c C_f \simeq 1$ ms typically.

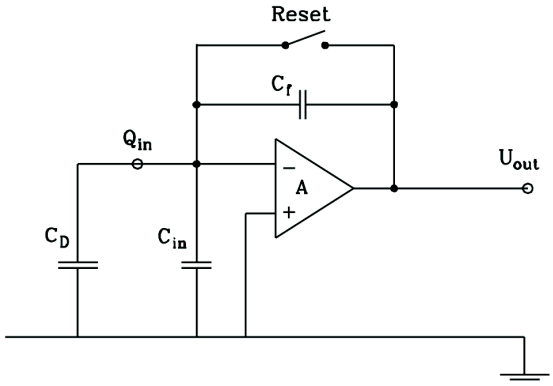

Figure 2.4: Principle of a Charge Sensitive Amplifier. The inverting amplifier has a capacitive feedback C_f. The reset switch is only used for bringing the system into its operating condition, and is often replaced by a high-ohmic resistor $R_c \sim 1G\Omega$.

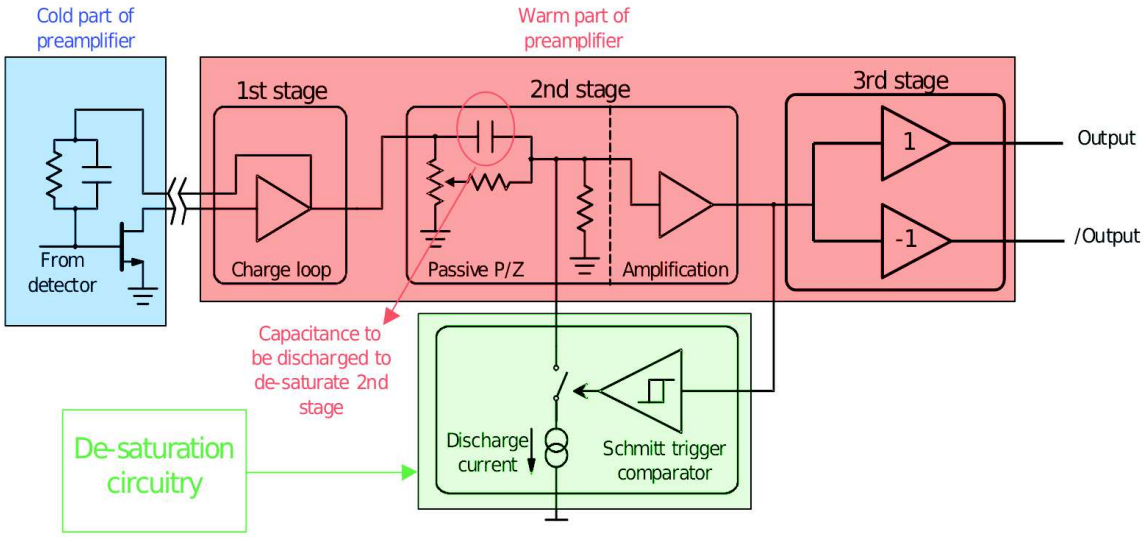

Figure 2.5: Three stages structure of AGATA preamplifier.

A simplified configuration of the signal preamplification in AGATA is shown in fig. 2.5, details are discussed in [44]. FETs (blue area) are working in a cold environment in order to reach adequate low-noise performances. The warm part (red area), operated at room temperature, is located outside the cryostat and comprises a low-noise trans-impedance amplifier, a pole-zero stage which brings the final pulse decay to 50 μs, a differential output, and a fast-reset circuitry (green area) which allows measurement of large energies when the preamplifier is saturated.

This electronics has a limited bandwidth which smooths the rising and falling slopes, as well as the edges of the transient signals. A noise contribution is also coming from both leakage current inside the crystal and the front-end electronics.

2.5.2 Crosstalk

Crosstalk is an electronic effect between channels which lead them to interfere with each other. A capacitive coupling still exists between channels, such that in any case, a fraction of the signal in one channel is readout in the others. There are two components which differ in their effects: a low-frequency proportional crosstalk leading to observable effects on the energy spectra [45] and a high-frequency derivative crosstalk which may distort signal shapes and induce spurious transient signals [39].

Proportional crosstalk is a charge signal on both neighboring segment channels with opposite polarity of the original net charge signal. The Core also affects each segment signal in the same way. This crosstalk can be compensated by adding a fraction of the original net charge signal. It can be explained by an insufficient decoupling of the power supplies of the FETs.

Derivative crosstalk is observed in neighboring segments only. It is based on an inductive coupling which can be compensated by subtracting a fraction of the derivative of the original net charge signal.

These effects can be minimized with a correct design and shielding [46] of the front-end electronics such that, in AGATA, the measured crosstalk is considered to be the minimum expected, related to the HPGe crystal design. It can be corrected [47], as long as it is well characterized for each channel-channel combination in the detector. This calibration was not performed in the present work and no crosstalk contribution has been applied on simulated pulse shapes.

2.5.3 Electronic response modeling

The electronic response of the whole AGATA electronics, from the FETs to the digitizers, has been investigated with the use of a pulser integrated in the Core preamplifier. Figure 2.6 shows the Core-pulser output signal, digitized and averaged on 100 pulses. The fitted response function s(t) corresponds to a sigmoid function as follows:

$$s(t) = \left(\frac{\delta}{\delta + \frac{\kappa^2}{1+\kappa^2} \cdot e^{\frac{-\sqrt{2}\cdot t}{\delta \cdot t}}} \right) \cdot e^{-\frac{(t-t_0)}{t_d}} - \frac{\delta}{2} \tag{2.5}$$

where κ controls the slope, δ is the amplitude, t_0 is the time at zero amplitude and t_d is the decay of the amplified signal, which is negligible in the presented time-scale. Fit parameters

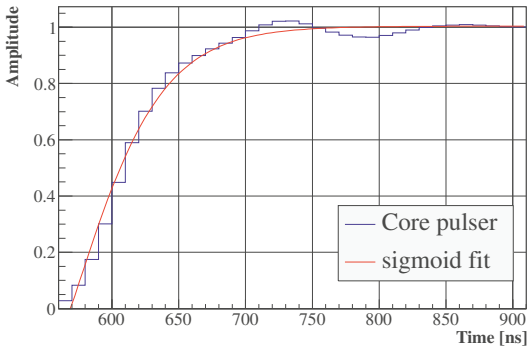

Figure 2.6: Averaged Core-pulser output signal of an AGATA detector, fitted with eq. 2.5.

are $\kappa = 23.8$, $\delta = -2$, $t_0 = 569$ ns and $t_d = 50000$ ns, leading to a T90 risetime value, i.e. the time necessary to rise from 10% to 90% of the maximum amplitude of ∼95 ns. It is a strong low-pass filter which drastically smoothes high frequencies in the leading edge of HPGe signals. It has to be noticed that the use of the AGATA Core preamplifier integrated pulser is not the best way to measure such risetime, because the pulser itself has a quite long risetime. The true AGATA electronic risetime should therefore be lower than 95 ns. Further work is this thesis will use this 95 ns ristetime as a reference. A check was performed and further results are not modified at all if one uses a 60 ns risetime as reference.

This function describes how any measured current inside the crystal is integrated along the electric circuit. The preamplifier output voltage V(t) simulated in a realistic way is a convolution between the current i(t) and its response function:

$$V(t) = \int_{t=0}^{t_0} \int_{t'=t}^{t'=t_0} i(t) \cdot s(t') dt' dt \tag{2.6}$$

This convolution filter is applied on the raw pulse, then a Gaussian noise with $6\sigma = 10$ keV is also added in order to simulate some noise in the system. The result of such smoothing is shown in figure 2.7. All pulses are affected :

- the Core seems barely smoothed but it is more difficult to retrieve the start time and the end time of the pulse shape,
- the kink on the hit segment is almost hidden,
- the initial asymmetry in left segment almost disappears,
- the slight induced signal on the right segment is attenuated.

The previous considerations show that some information is lost after this filtering. This fixes a spatial resolution limit below which it is impossible to detect any pulse-shape variation.

2.6 Simulation of realistic pulse-shapes

Monte-Carlo simulation allows to determine the location of γ-ray interactions and the associated energy, following physical laws. For this purpose, Geant4 [48] is used. The detector

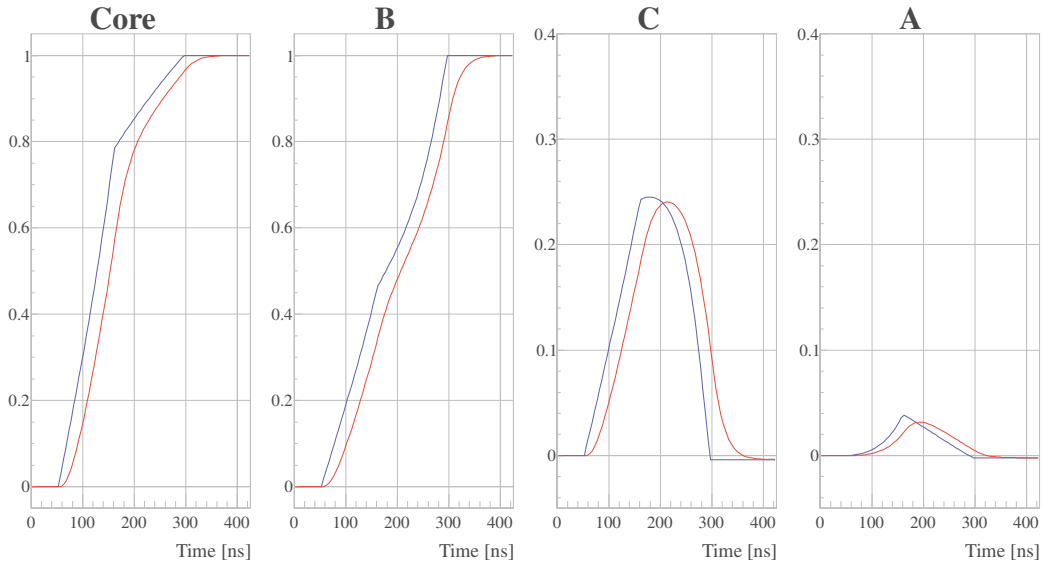

Figure 2.7: Raw pulse shapes (blue line) and same pulses after electronic low-pass filtering (red pulse).

is considered as a monolithic cylinder, no segmentation is necessary at this stage. It is surrounded by an aluminum end-cap. Then, a simulated γ-ray source with identical properties to the one used in the experiment is used. Geant4 creates one photon and tracks it until it is absorbed by any material or until it goes out of the limits of the simulation world. The location and the energy deposit of the interactions are stored in an output file.

In the case of multiple Compton scattering in the detector, a single photon interacts many times in the crystal. Because the time of flight of a photon between two interaction points in the crystal is much shorter than the timing response of HPGe detectors, these events cannot be experimentally separated. In the case of a simulation, each interaction is simulated as a unique one. The global pulse is just the linear combination of each individual pulses, weighted by the corresponding partial energy release. Then, it is possible to recreate realistic pulses shapes, representative of any measurement with the detector considered.

Chapter 3

The IPHC scanning table

We have shown in sections 1.4.2 and 1.5 that the performances of the AGATA spectrometer is based on pulse-shape analysis which uses simulated pulse-shape databases, and γ-ray tracking. To properly simulate pulse-shape signals, their formation and modeling have been studied and tested thanks to 2D scanning tables installed at Liverpool [49] and at Orsay [50]. Detailed studies have been performed on segmented HPGe detectors, in particular on the symmetric prototype [51, 52] and asymmetric [53] capsules of AGATA. However, the time needed to scan 1200 points in an AGATA crystal is about two months, which prevents from performing scans in the full volume of each detector.

In the present chapter, we present the IPHC scanning table based on the Pulse Shape Coincidence Scan method (PSCS) [35] which determines experimental mean pulse shapes as a function of the γ-ray interaction location in a HPGe detector. The major advantage of this technique is that it allows to establish a full database of experimental pulse shapes inside a large volume detector. For AGATA detectors, 48 500 points are scanned along a 3D 2 mm grid in only two weeks of scan. Other fast methods are also arising such as the ones described in [54, 55] where the use of collimated beam is no more necessary.

3.1 Pulse Shape Coincidence Scan method

The principle of PSCS is the following: a collimated γ-ray source is placed on an XY table, allowing 2D horizontal motion. Firstly, the detector is placed vertically (position A in figure 3.1), over the γ-ray beam, such that the front face of the crystal is illuminated. Measurements are performed over all the cross-section of the crystal so that for each known XY position in the crystal, all pulse shapes along the Z axis are collected. Secondly, the detector is placed in the horizontal position (B) in order to be illuminated from its side. The pulse shapes collected come from a known Z position, inside the corresponding XY plan. For the analysis, two distributions of pulse shapes are compared, one coming from position (A), the other coming from position (B), corresponding to two γ-ray beams virtually crossing at point M. Pulse shapes of a position sensitive HPGe crystal such as AGATA are perfectly related with the interaction location. As a consequence, pulses of distribution (A) differ significantly from these of distribution (B) except those coming from the crossing point M where they should be identical. A χ^2test is performed between (A) and (B) in order to select pulse shapes which

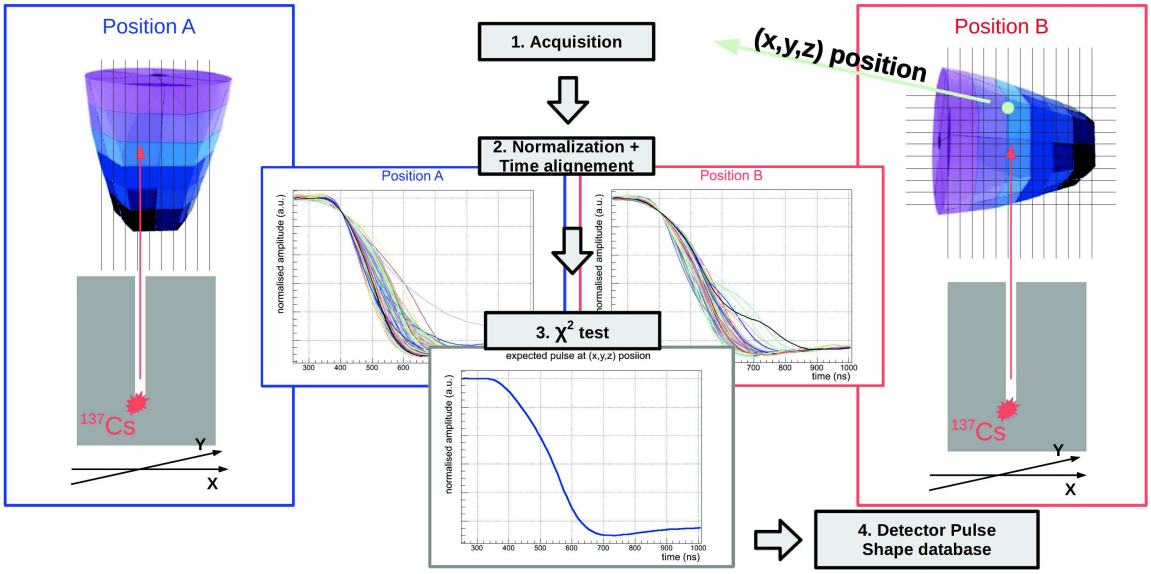

Figure 3.1: Principle of the Pulse Shape Comparison Scan Technique which is used at IPHC.

are most similar. These ones are averaged, thus giving the average experimental pulse shape at position M in the crystal.

Several issues are encountered to perform these measurements and data treatments on a whole crystal volume. Most importantly, the vertical and horizontal measurements must cross at the expected point. The collimated γ-ray beam has to be thin but also intense enough to get sufficient statistics at each point in reasonable time, i.e. several days of scanning per detector position. The scanning table motion must be synchronized with the digital-electronics acquisition system and the analysis deals with a large amount of data. The IPHC scanning table is designed to perform PSCS in most favorable conditions, considering these issues.

3.2 Description of the setup

3.2.1 Mechanics

Some key requirements determine the design of the scanning table which is depicted in fig. 3.2:

- it should allow the motion of the 160 kg collimator along the X and Y axes,
- it must ensure a fine positioning of the detector relatively to the γ-beam for both front and side scans,
- is has to keep the detector as close as possible to the collimator.

The collimator relies on two XY moving axes. The robustness of these axes guarantees that the collimator can move over a large range (300×300 mm) without any significant variation of the pencil beam verticality. Each axis is completed with an optical measurement system, calibrated with 1 μm precision, which gives an accuracy of the collimator positioning better than 50 μm over the 300 mm axes range. In scanning conditions where the tables move by only

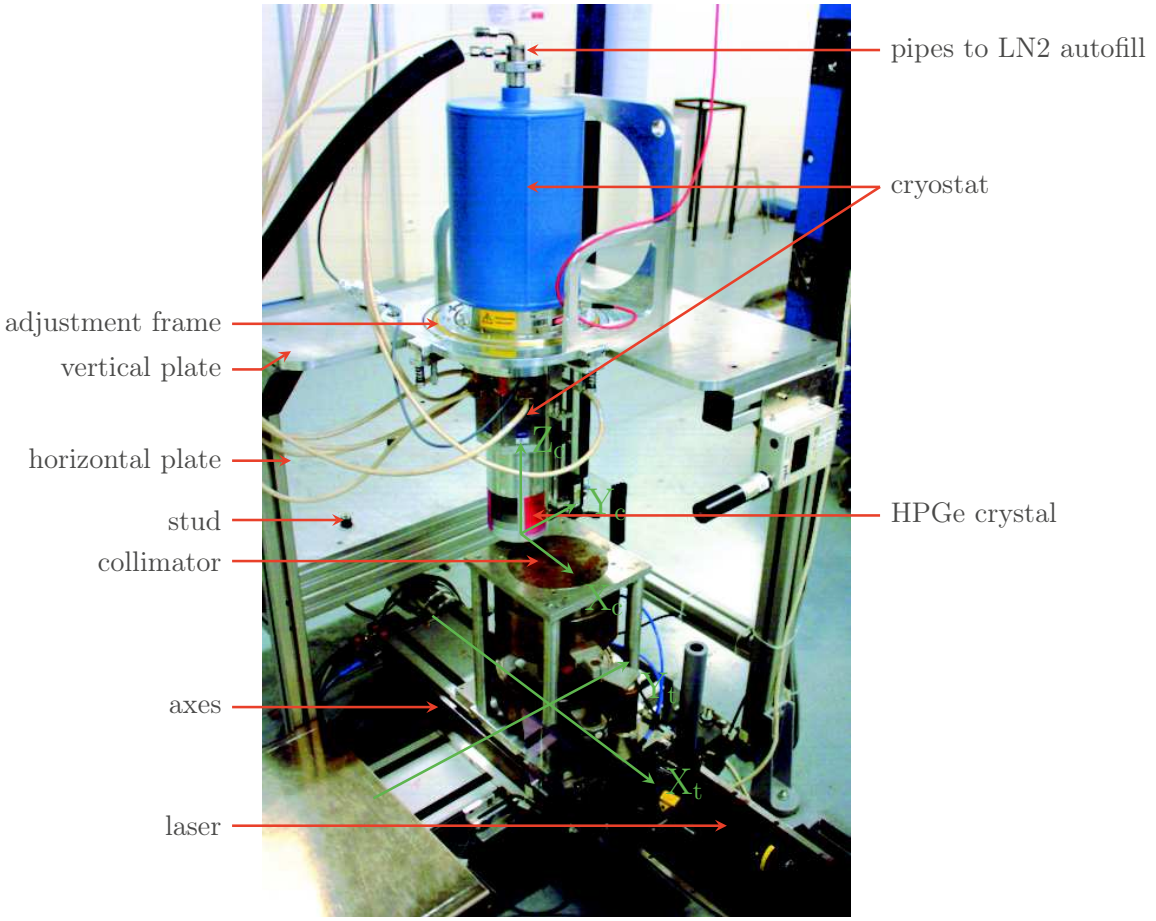

Figure 3.2: Scanning table with comments. Both scanning table and crystal coordinates referential are presented in green.

a few millimeters, the positioning is even more accurate, about 10 μm. The scanning table structure sustains two dedicated plates supporting the detector for vertical and horizontal measurements, respectively. The plates are equipped with centering studs to finely place the *adjustment frame* (or frame), which is the interface piece between the detector and the structure (see fig. 3.2).

The frame has been designed to compensate any variation between the HPGe crystal axis and the scanning table axes. These variations can come from various tilts :

- the perpendicularity between the collimated γ-beam and the plates,
- the cryostat alignment compared to the plates,
- the HPGe crystal tilt in its own cryostat.

To make this compensation possible, the frame is composed of multiple rings, allowing to adjust precisely the cryostat azimuth and elevation with micrometric screws. A 360° rotation of the crystal along the Z axis is also possible by steps of 90°. A continuous rotation by ±10 degrees allows fine adjustments. These movements are shown in fig. 3.3. Finally, the

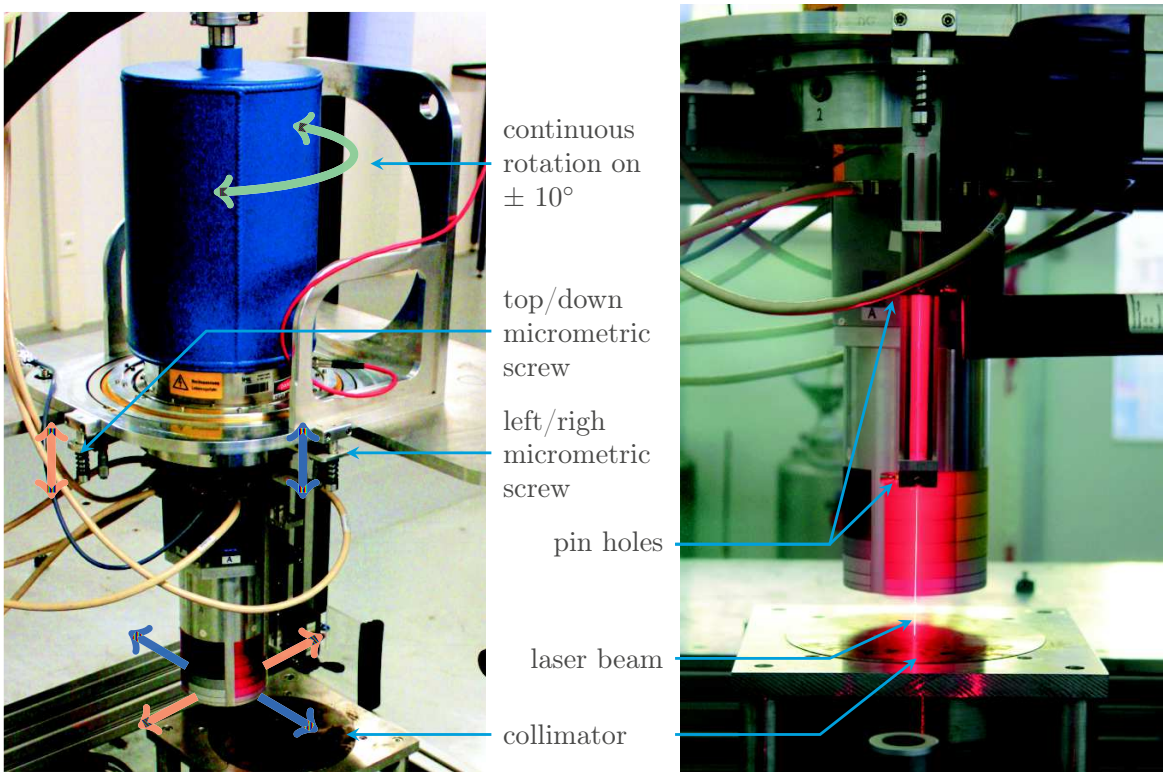

Figure 3.3: Zoom on the AGATA detector mounted in vertical position, with a description of various positioning adjustment parameters of the frame. The right picture shows the laser beam passing through the pin holes for a proper alignment of the system

collimator is placed on a plate which supports also a laser system. When the γ-ray source is removed from the scanning table, the laser beam can pass through the collimator in order to visualize the γ-ray direction. In the same time, a module comprising a pair of pin holes is fixed on the cryostat. This is of prime interest for the alignment procedure depicted in sub-section 3.5.

3.3 Collimated γ-ray sources

The precision of the interaction location depends on the quality of the collimation. The IPHC collimator design is depicted in fig. 3.4. It is made with several pieces of heavimet (Tungsten alloy), lead, steel and tantalum. It can be divided in two sub parts:

- the top part is the thicker, larger an denser one, it contains the collimated hole,
- the bottom part is moving, thanks to a pneumatic cylinder, in order to open and close the collimator.

In the center of the collimator, there is room to place a small lead castle which contains the γ-ray source. This setup allows to exchange easily and safely the γ-ray sources which are permanently sealed within their small lead castle at least.

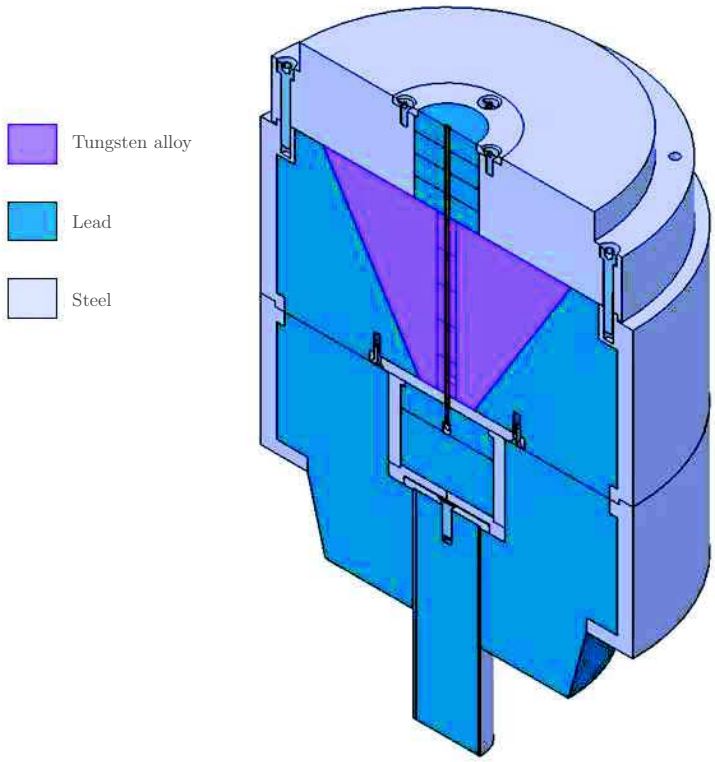

Figure 3.4: Scheme of the collimator. The inner lead/Tungsten alloy tube is 2.5 mm large due to mechanical issues. It is filled with a tantalum tube with 1.5 mm internal diameter to reach the final collimation.

Two γ-ray sources (^{241}Am and ^{137}Cs) where used with the same collimator. Their properties are listed in table 3.1. The ^{241}Am source is used to determine the position of the crystal compared to the scanning table axes, as well as for near-surface analysis. The ^{137}Cs source is used for crystal volume studies, including the PSCS.

The collimated hole has a diameter of 1.5 mm along 165 mm. The collimator design, its materials and the γ-ray source properties are used in order to estimate the pencil beam profile with a Geant4 simulation. Such profile after the collimator output is shown in fig. 3.5. In spite of the significant length of the collimator, the γ-ray beam is slightly divergent (maximum 0.5°, corresponding to a 1.5 mm tilt over 165 mm), resulting in a larger size of the spot when the distance from the collimator increases. It is clear that the closer the detector to the output of the collimator, the denser the γ-ray interaction locations.

3.3.1 Electronics

The electronics of the scanning table is based on ten TNT2 [56] NIM digital boards which represent up to 40 simultaneous readout channels. They are equipped with 100 MHz, 14 bits flash ADCs sharing a common clock. The online calculation of the pulse height, i.e. the energy, is made using a Jordanov trapezoid filter [57]. The output data can be digitized pulse

Radioactive source	γ-ray energy [keV]	Source activity [MBq]	Collimated flux [photon/s]
^{241}Am	59.5	75	90
^{137}Cs	661.7	550	1000

Table 3.1: Characteristics of the ^{241}Am and ^{137}Cs sources of the IPHC scanning table.

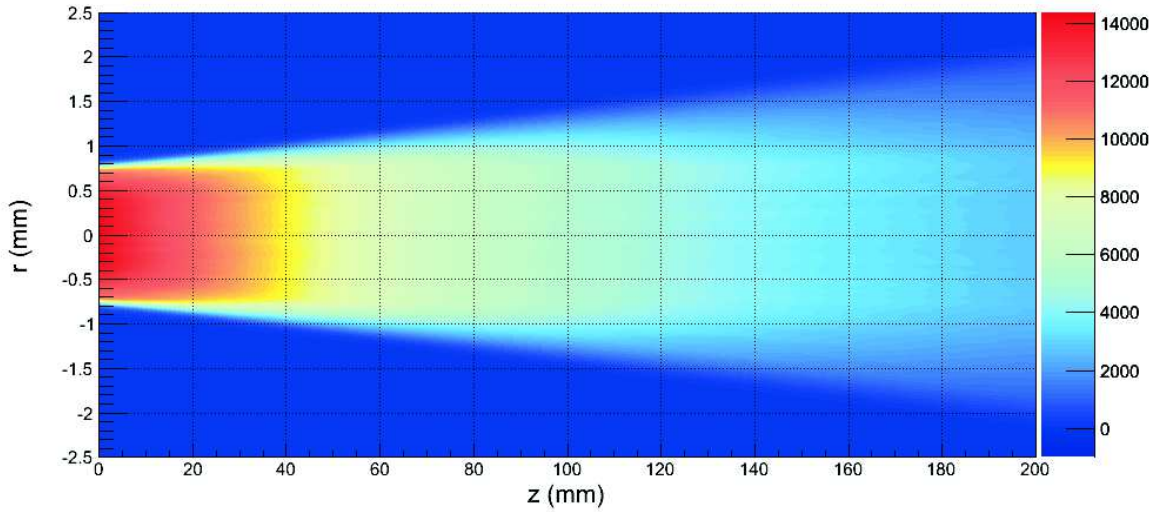

Figure 3.5: Geant4 simulation of the 662 keV γ-ray beam profile after the collimator output. Z is the distance from the exit of the collimator. Colors indicate the relative beam intensity, only primary photons with 662 keV are shown (arbitrary units).

shapes (Oscilloscope mode), energies (Energy mode) or both together (Mixed mode). They are merged and stored in binary files in a dedicated computer with large storage space for further analysis. The trigger system is quite simple even with multi-segmented detectors: a digital trigger integrated in the TNT2 cards runs on the Core channel which is the only triggering channel. The digital trigger is based on a simple first difference stage [58]. The trigger signal propagates, through a Fan-In Fan-Out module, to the 36 other channels. A systematic delay of 80 ns was measured between the Core triggering card and the 9 others, due to the trigger signal propagation. For any interaction in the crystal, the pulse shapes of the 37 channels are registered, even for segments with non-relevant signals. This information gathered for each trigger is called a supertrace. The length of the digitized pulse shape per channel is typically 120 points, corresponding to 1.2 μs. It is as short as possible in order to minimize the storage space, but long enough to encompass the signal baseline, the pulse shape and the final baseline or plateau.

Each TNT2 card in Mixed mode produces two time-stamped files, one of digitized pulse shapes and one of energies. In order to retrieve traces among raw data files, the first analysis consists of parsing the 20 TNT2 output datafiles, looking for events sharing the same time-stamp.

3.4 Scanning procedures

3.4.1 Calibration

The energy calibration of each channel is performed with a specific serial algorithm. A first rough calibration is done with a ^{137}Cs measurement: it is a linear extrapolation between zero and the 662 keV line. It is followed by a ^{152}Eu measurements with sufficient statistics, typically a 12 hours measurement. Two identical sources are used, placed on opposite sides of the crystal, with a total count rate of the Core about 2 kHz. Knowing the expected position of the ^{152}Eu lines thanks to the first calibration, the algorithm identifies peaks, rejects the background[1] and fits each peak with a Gaussian function if there is enough statistics. The different lines are then used to perform the energy versus channel linear calibration.

An ADC-gain alignment is also necessary. Even if all the readout electronics, from the FET to the digitizer, is the same for each channel, the total gains are not identical. These changes can come from various origins: slight differences of the gain preset, dispersions around the specified components characteristics, operating temperature divergence between some segment FET, or even ADC non-linearity. It means that, for an identical energy deposit in different segments, the measured pulse-height amplitude differs. This can lead to spurious analysis when comparing different channels with each other.

In order to correct this effect, a gain matching factor is computed for each channel, such that it allows to normalize all pulse shapes with identical energies to the one of the core. The ADC alignment consist of applying this gain matching factor to the raw pulse shapes before any analysis. At the end of this filter, an identical energy deposit in any channel results in a similar pulse-height.

[1] Use of the TSpectrum::Background class of ROOT [59] v5.34.03 with the option "BackOrder2 BackSmoothing5 BackDecreasingWindow Compton"

This factor is calculated based on the energy calibration parameters. As the Jordanov trapezoid parameters are identical for all channels, this energy calibration includes the individual gain of each channel. The gain matching factor is the ratio between the slope of the energy calibration of the segment over the one of the Core.

3.4.2 Scanning possibilities

The first way to use the scanning system described here is to browse the whole cross-section of a detector in discrete measurements. The γ-ray spectra are then analyzed at each scanned point in order to observe variations of the detector response as a function of the interaction position. An algorithm is used in order to determine various parameters such as the full-energy peak net area, the peak position, the energy resolution, or any other useful information from the γ-ray spectrum. The parameters are then plotted as a function of the position of the collimator, in order to have a two dimension distribution of local effects. Two basic criteria define the quality of such a scan:

- **the step between two successive points**: the closer the various measurements, the better the final granularity of the projection, allowing to see smaller details,
- **the acquisition time at each point**: the longer the measurement, the more reliable the extracted parameters.

An accurate scan of a large volume HPGe detector with a large scanning granularity combined with a long acquisition time can last several weeks. For such long scans, issues related to calibration shifts can arise, leading to an additional difficulty in the analysis, or miss-interpretations when looking at some parameters such as the peak position. A balance is to find between granularity, statistics at each point and duration of the scan. As a standard we use a 2 mm grid and a measurement time of $\sim$120 s. In specific cases, smaller pitches may be used, 1 mm, 200 μm or even 50 μm for a small number of scanning lines of limited length.

A specificity to the IPHC scanning table is the possibility to place the detector in both vertical and horizontal position very accurately. Vertical and horizontal scans virtually cross in the detector, forming a 3D-grid used to perform PSCS. Such technique allows to establish an experimental signal basis and to study peak position shifts, but some information such as the local voxel resolution, or the local P/T ratio are not available due to a lack of statistics.

3.4.3 Filtering of pulse shapes

A first filtering of the raw data is essential in order to perform any kind of pulse-shape analysis: the pulse height information of each pulse-shape is removed in order to focus on the signal shape. As the rising edge of the output signal of HPGe detectors is strongly dependent on the location of the interaction, the trigger is not the same for each event. A time alignment is necessary before performing comparisons between samples. For each event, the filter is the following :

1. apply an offset to place the signal baseline to zero,
2. align the gain of each channel,

3. the Core signal is normalized to 10000, the same normalization factor is then applied to the other channels (10000 is chosen to keep a sufficient precision while recording the data as *unsigned short int* in hard drives),

4. the sampling is virtually increased from 100 MHz to 1 GHz with a linear interpolation between two consecutive samples,

5. an 11-point moving average is applied on the 1 GHz signal,

6. Core time alignment: the Core signal is shifted in time such that the time where it reaches 50% of its maximal amplitude is 600 ns,

7. segments time alignment: the time at 50% amplitude of the segment with the highest energy deposit is shifted to 600 ns, the same shifting factor is applied to all other segments,

8. the sampling is lowered back to 100 MHz.

The result of this filter on the pulse shape is almost insignificant: there is only a slight smoothing of the pulse shapes, mainly on the sharp edges of some transient charges. Any filter smoothing significantly the pulse shapes, as a low-pass filter, would reduce the noise contribution with a loss of part of the information used for the interaction localization.

Pulse-shapes are stored in the computer memory as *short int*, i.e. their value are entire. This reduces the required memory size for storage compared to floating data.

3.4.4 Progressive penetration of the γ-ray beam inside the detector

It is possible to determine very accurately crystal or segment boundaries even if the pencil beam has ∼2 mm in diameter. As it progressively penetrates in the detector, the amount of detected events increases. For the ^{241}Am source, any γ-ray is fully detected, such that the full-energy peak area is proportional to the cross-section of the circle-shaped spot with the detector, as depicted in fig. 3.6. This behavior is also true for the ^{137}Cs source, but full-energy peak area is then also driven by Compton scattering.

The analytical expression of the area A of a circle penetrating a rectangle along the X-axis is :

$$\mathrm{A(x)} = \alpha \cdot (2 \cdot \arccos[\beta \cdot (\mathrm{x} - \mathrm{x_0})] - \sin[2 \cdot \arccos[\beta \cdot (\mathrm{x} - \mathrm{x_0})]) \tag{3.1}$$

where x is the position of the pencil beam spot, x_0 is the position of the crystal boundary, which is also the symmetry center of the curve, α and β control respectively the amplitude and the rising slope.

An example of a ^{241}Am photopeak area profile along a segment boundary is given in fig. 3.7. AGATA B006 D1 segment front-face boundary is scanned. The maximal value remains constant as long as the pencil beam fully points in the segment. As it gradually goes out of the segment, this value decreases down to zero. Equation 3.1 fits well with the decreasing slope. Fit parameters give a boundary localized at x_0 = -170.81 mm and a beam spot diameter of 2.08 mm. Such diameter corresponds to a distance of about 20-30 mm between the output of the collimator and the front face of the detector, according to the

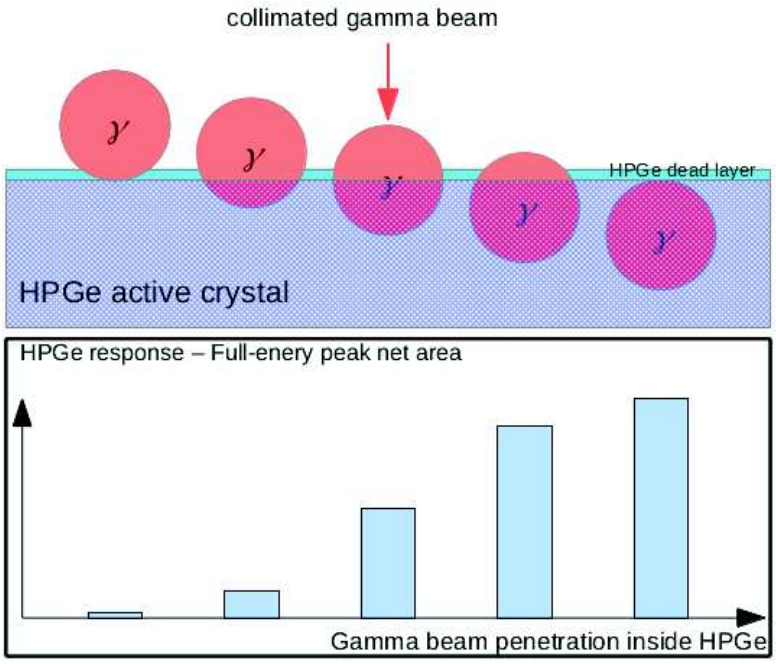

Figure 3.6: Effect on the photopeak net area of the progressive penetration of the γ-ray pencil beam in the HPGe active area.

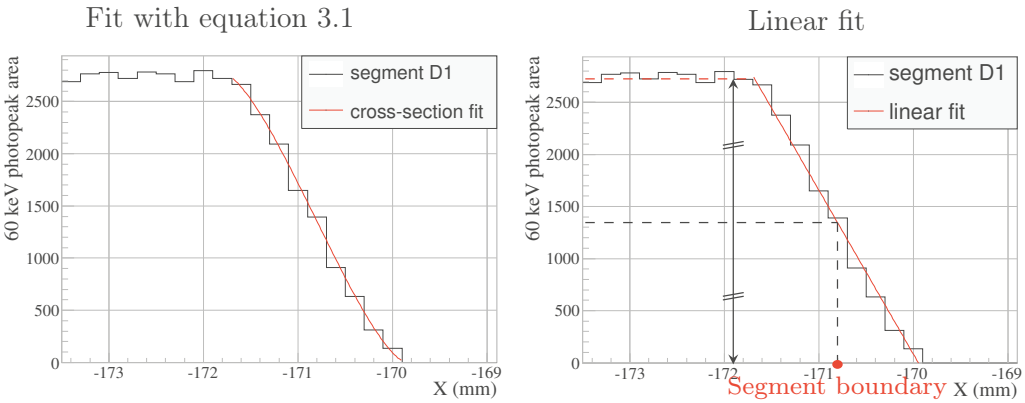

Figure 3.7: ^{241}Am photopeak area along a segment boundary (scan of the front face of AGATA B006 crystal). The pitch between two points is 0.2 mm.

simulated pencil beam profile in fig. 3.6. This distance was determined mechanically with the AGATA cryostat in horizontal position above the scanning table as follows: the end-cap front face position was roughly measured with the laser beam and the front face of the crystal was determined with the γ-ray beam. The distance is 25 mm $\pm$ 1 mm, which agrees with simulation. The γ-ray beam diameter value is large, but it corresponds to a beam profile with a full width at tenth maximum of $\sim$1.7 mm, such that most interactions are focused in a smaller diameter. The curve in fig. 3.7 is very close to a straight line, a linear fit is performed: the abscissa value at half height of the maximal plateau gives a boundary localized at X = -170.82 mm. Both x_0 and X values are in agreement, the linear fit methodology will be used for further investigations, as it is easier to implement in a serial data-analysis algorithm.

3.5 Mechanical alignment of the detector

The major drawback of the χ^2 test comparison is that it always gives a result, even when the two compared series of pulses shapes are not virtually crossing. Thus, a miss-alignment will hardly be determined by analyzing the output of the PSCS and an extreme care is required for the detector positioning.

A method has been developed in order to guarantee that the virtual 3D scanned points are the result of the true crossing of the corresponding vertical and horizontal measurements. It is based on two elements:

1. a laser beam can replace the collimated γ-ray beam in order to visualize its direction,

2. an optical element, used with the laser beam, defines a reference alignment.

The optical element consists of a pair of calibrated pin holes, spaced by 16.5 cm. The diameters of the holes are 200 μm for the first and 50 μm for the second, both can be finely positioned in a plane perpendicular to the laser beam. The centers of the two pin holes define a direction. The whole piece is called the target and it is fixed on the cryostat. When the laser beam crosses exactly the center of the two pin holes, an intense diffraction figure is

visible at the target output. This means that the direction defined by the target is parallel to the laser beam.

In order to precisely set the verticality of the AGATA crystal, a 200 μm pitch scan is performed (see section 3.6.2). Once the crystal axis is parallel to the γ-ray beam, the pin holes are set in order to see the best and most intense diffraction figure. The setting of the target is then fixed. It will be used as a reference orientation. Now, if the detector has to be moved, it is possible to retrieve the verticality at any time using the laser and the target.

When the detector is in the horizontal position, the laser can be deflected at 90° with a deflection piece. A reference mark has been placed on the walls of the scanning room, which guarantees that the X axis of the scanning table is parallel to the deflected laser beam. The micrometric screws of the frame are used to get the most intense diffraction figure after the target. At this moment, the crystal Z axis is properly aligned with the scanning-table X axis.

The alignment procedure for an AGATA detector is the following, a crystal referential (X_C, Y_C, Z_C) and a scanning-table referential (X_T, Y_T) are used :

1. The cryostat is set in the vertical position. The verticality is roughly adjusted when the cryostat end cap is perpendicular to the collimator surface.

2. The detector is rotated along its axis Z_C such that the segmentation line between sections A and F is parallel to the Y_T axis of the scanning table.

3. A ^{137}Cs scan is performed around the central hole, along the X_T and Y_T axes, with little steps and high statistics. The analysis of the 662 keV photopeak net area in each crystal slice allows to precisely determine a possible tilt of the Z_C axis of the crystal compared to the γ-ray beam. If a tilt is detected, it is then corrected using the micrometric screws of the frame. At this stage, the crystal axis Z_C and the γ-ray beam are aligned. The crystal axes X_C and Y_C are also aligned with the axes X_T and Y_T of the scanning table (second item).

4. The ^{137}Cs source is replaced by the laser beam. The target is then adjusted, such that the most intense diffraction figure is reached at the target output. At this point, the target is collinear to the crystal axis Z_C and the pin holes are definitely set until the end of all measurements.

5. All measurements in the vertical position can be performed.

6. The cryostat is set in the horizontal position.

7. The laser beam at the output of the collimator is reflected perpendicularly with a prism. The 90° elevation angle is set by the prism, the azimuthal angle is set parallel to the X_T axis thanks to the reference mark on the wall. The orientation of the detector is adjusted with the micrometric screws, in order to allow the laser beam to pass through the target. At this point, the detector axis Z_C is perpendicular to the γ-ray beam and also parallel to the X_T axis.

8. All measurements in the horizontal position can be performed.

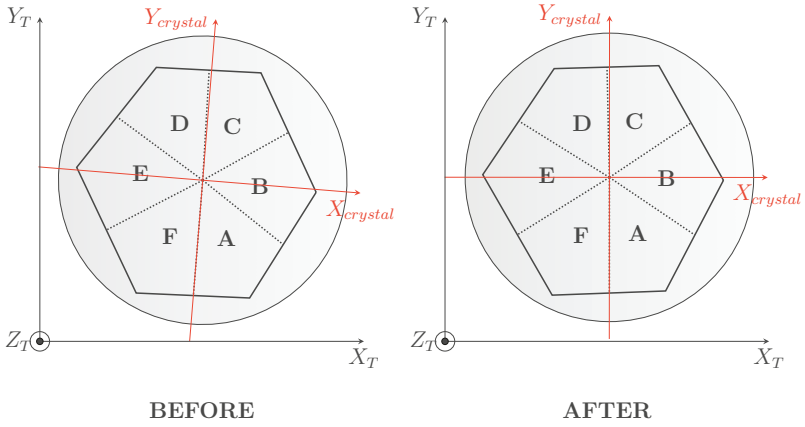

Figure 3.8: Principle of the rotation alignment in vertical position.

3.6 Crystal alignment check

It is of primary importance that the scanning table Cartesian coordinates system is collinear with the detector Cartesian coordinates system for each scan required for the PSCS. This way, the vertical and the horizontal scanning grids are well crossing in three-dimensions in the crystal, leading to the 3D scanning grid in the detector reference system. Each step of the crystal alignment has to be validated by a specific scan in order to guarantee the positioning. The various alignment checks for the scan of an AGATA crystal are described in this section.

3.6.1 Vertical rotation

This step allows to align the axes X_T and Y_T of the scanning table with the axes X_C and Y_C of the detector reference system, as shown in fig. 3.8. Once the detector is placed in vertical position on the scanning table, it is rotated along the Z_C axis of the crystal, such that the front segmentation line between segments A1 and F1 is parallel to the Y_T axis of the scanning table. This operation is done using the ^{241}Am source: the collimated beam is exactly on the middle of the segmentation line when the 60 keV photopeak areas are identical in both neighboring segments. The detector is rotated until the X position of the segmentation line AF is identical all along the Y-axis. A specific scan is performed in order to check the result of this procedure: lines with 200 μm steps along X_T are scanned for various fixed Y_T positions. A decreasing/increasing profile of the photopeak area appears, which is identical to the one shown in fig. 3.7. A linear fit on the slope allows to determine precisely the location of segment boundaries following section 3.4.4. Results are plotted in fig. 3.9. Thanks to the tight X-range, it is possible to consider that the AF line is sufficiently well aligned with the Y-axis (the tilt of less than 0.1 mm along 25 mm corresponds to an angle of less than 0.2°). Both AF and CD segmentation lines are not aligned, as expected with segmentation patterns defined for AGATA asymmetric crystals.

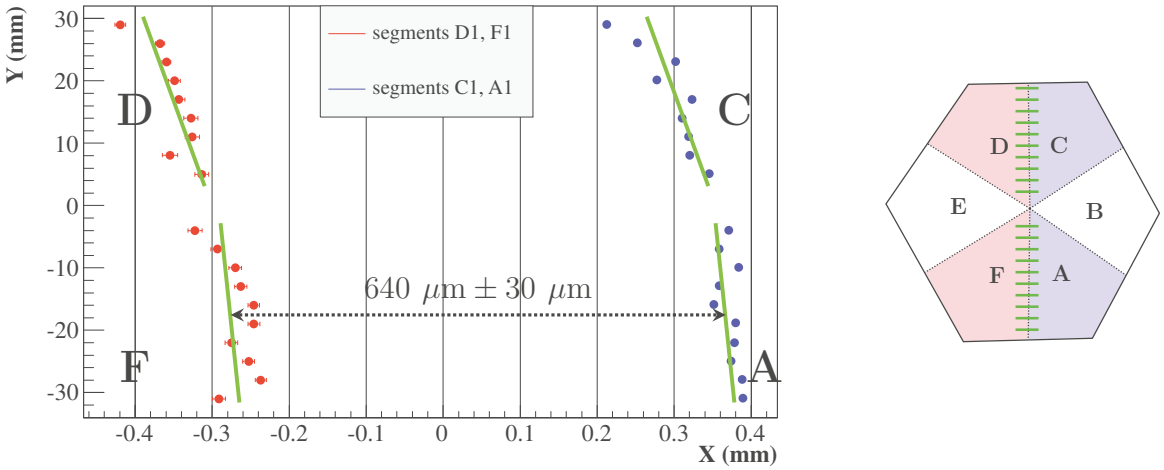

Figure 3.9: Location of the segment boundaries along the X axis of the scanning table, deduced from the intensity profile of the 60 keV peak seen by segments D1, F1, A1 and C1. Care has to be taken to the scale of the figure, with a Y range 60 times higher than the X one. The green lines on the right scheme represent the corresponding scanning lines. The segmentation line width averaged over the 2 times 10 lower points is 640±30 μm.

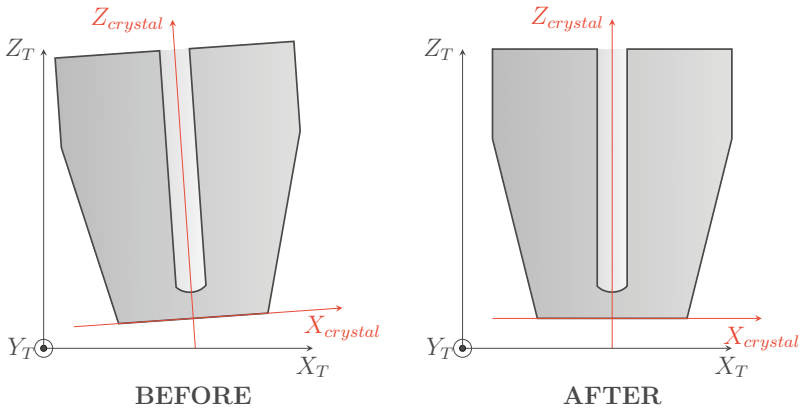

Figure 3.10: Principle of the vertical alignment.

3.6.2 Verticality

Another point is to be sure that the collimated beam is collinear to the Z_C axis of the detector, see fig. 3.10. A good mechanical alignment of the cryostat in not enough, as previous work proved that a crystal tilt within its cryostat is possible [52]. A miss-alignment results in a systematic XY shift between the front and the rear of the crystal. Therefore, it has to be measured and corrected. Because of the external asymmetric shape of the crystal, the only reliable reference is the bored hole. By making fine ^{137}Cs scans along the bored hole, it is possible to measure its position towards each slice and to check for a possible tilt. Two scanning lines crossing the center, with 200 μm steps and huge statistics, along axes X_T and Y_T are performed, as shown in fig. 3.11(a). For each slice, the γ-ray spectra of the 6 segments in addback mode are analyzed. The behavior of the photopeak area in slice 3 is shown in fig. 3.11(b). Values are shifted and normalized so that the value of the photopeak area in the hole is zero, and the maximal value is 1. This filtering allows to use the same serial analysis for each slice, whatever the statistics or slope variations. From this figure, the hole position and width is clearly shown by a drastic decrease of the 662 keV photopeak area. The reason is that the crystal has 13 mm thickness in front of the bored hole, compared to a 90 mm thickness in the bulk just around. Three behaviors arise from this plot :

- in the hole region the 662 keV area is small and its profile is flat due to the small amount of HPGe material which is crossed by the γ-ray beam,
- on the bored hole surface, while the γ-ray beam crosses its boundary, the photopeak area is proportional to the surface of the γ-ray spot overlapping the detector active volume (see section 3.4.4) (peak area between 0 and 0.8),
- in the bulk, the photopeak area behavior is driven by the secondary Compton scattered photon re-absorption probability (peak area larger than 0.8).

The center of slice 3 is computed from fig. 3.11(b). The falling and raising slopes on the bored-hole boundary are fitted separately by a linear function. In each case, the X position at 0.2 maximum peak area is deduced from the slope of the fit equation. The barycenter of these two values is the position of the center of the slice. It has to be noticed that the real boundary position should be at half maximum of the slope. As it is tricky to determine where the slope stops, the 0.2 amplitude value is chosen, leading to an underestimation of the hole diameter, without any effect on its center determination. This analysis is performed for slices 2 to 6 along both X and Y axes. Results are plotted in fig. 3.12. Error bars are wider for the slices at the rear of the crystal, i.e. for larger depth, because of the progressive decrease of the statistics. The first scan allows to measure the crystal tilt. A 180 μm shift in the XY plan between the front and the rear of the crystal is measured. The detector angle of incidence is then corrected using the micrometric screws of the frame. The second scan allows to verify that the tilt correction is valid. Indeed, after correction the remaining XY shift is negligible.

At this point, the Z-axis of the detector is collinear to the collimated γ-ray beam. The radioactive source is replaced by a laser beam in order to setup the optical alignment system.

A secondary result of this analysis is the measurement of the hole diameter, which is on average around 14-14.5 mm. This value is larger than expected, and was confirmed on several 2D scans. A detailed study of this region will be described in section 4.7.

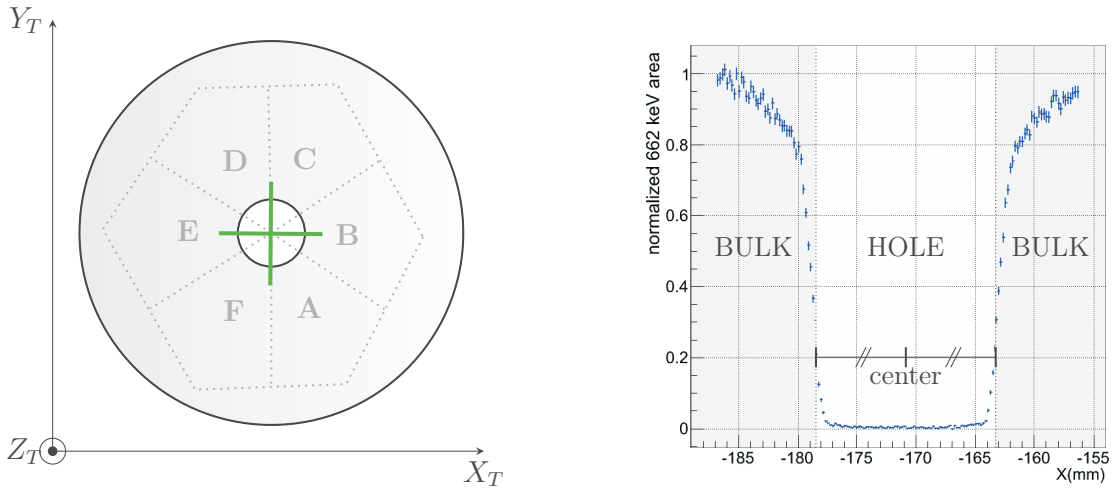

(a) (b)

Figure 3.11: (a) Scanning lines (green) for the verticality check. (b) ^{137}Cs normalized photopeak area profile within slice 3 as a function of the collimator position crossing the bored hole along the X axis.

3.6.3 Horizontal placement

In the horizontal position, the Z_C axis of the crystal is set collinear to the X_T axis of the scanning table, as shown in fig. 3.13, by the use of the optical laser system. The accuracy of such an alignment is checked once for good with a dedicated scan, shown in fig. 3.14(a). The procedure is similar to the one presented in section 3.6.2. Instead of analyzing slice spectra, as in the vertical placement, the Core spectra are analyzed. The absence of active material in the bored hole creates a slight bump in the Core photopeak area, due to a lack of counts. However, the photopeak area within the bored hole is around 90% of the one within the bulk (see fig. 3.14(b)). The slope analysis is therefore not as straightforward as for the vertical analysis, leading to larger error bars in the final plot shown in fig. 3.14(c). The crystal Z-axis is considered to be well aligned with the scanning table X-axis.

(a) BEFORE ALIGNEMENT

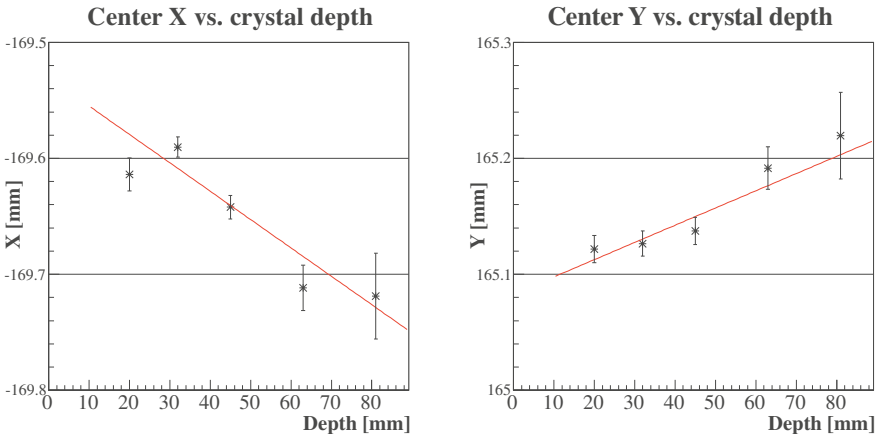

(b) AFTER ALIGNEMENT

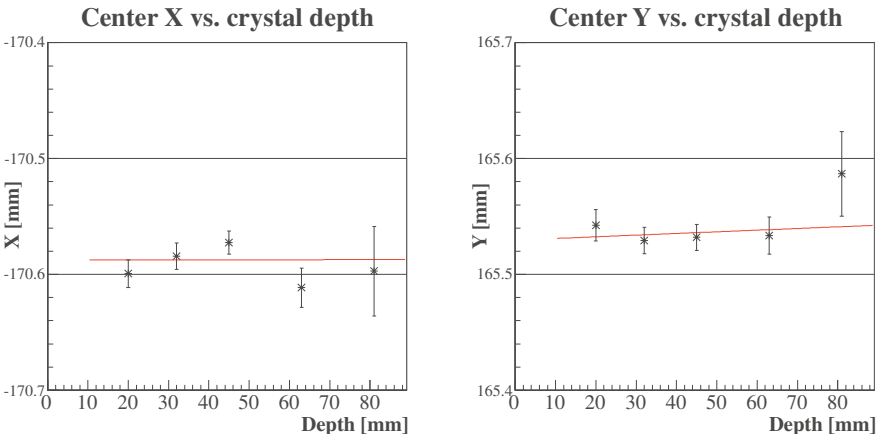

Figure 3.12: Position of the center of the bored hole of each slice along X and Y axes as a function of slice depth before (a) and after (b) alignment.

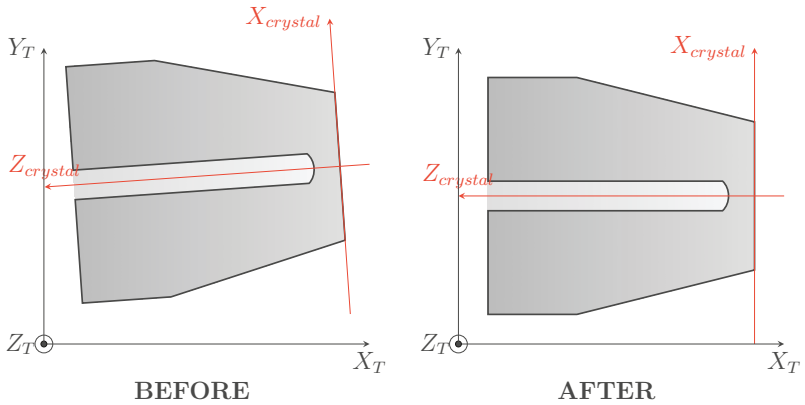

Figure 3.13: Principle of the horizontal alignment.

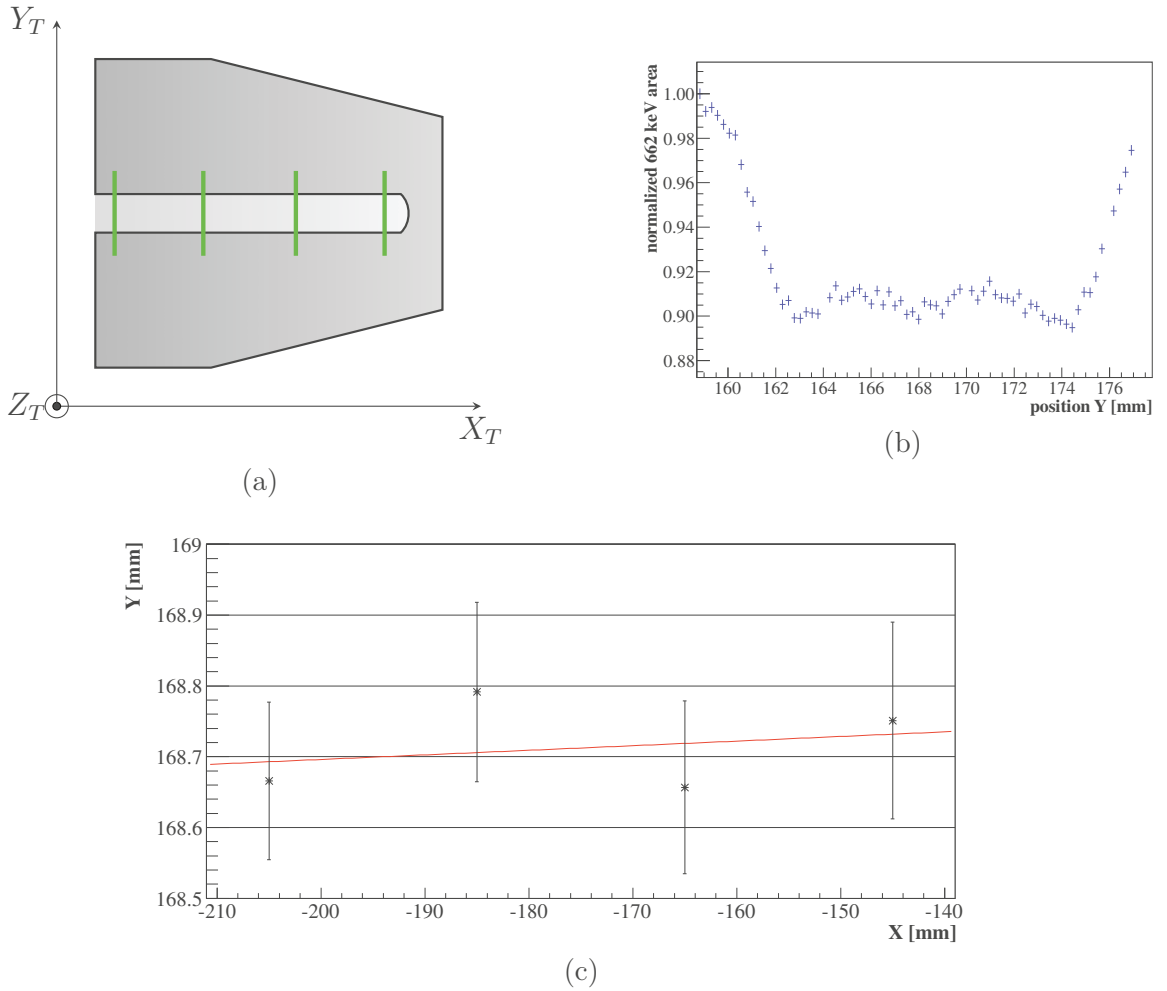

(a) (b) (c)

Figure 3.14: (a) Scanning lines (green) for the horizontal tilt check. (b) Example of normalized Core 662 keV photopeak area distribution along the bored hole. (c) Position of the center of the bored hole for the 4 scanning lines, in the scanning table referential (X_T, Y_T).

Chapter 4

AGATA B006 characterization

AGATA B006 capsule was mounted in a specific single-crystal test cryostat for measurements. An adaptation mechanical frame allows to place the cryostat into the frame for the detector scan in vertical and horizontal positions. It appeared during the first scans, that the coupling between the AGATA test cryostat and the LN2 automatic filling (autofill) system affects the readout. Indeed, the centroid of segments and the FWHM of the Core are significantly degraded during the LN2 autofill. It takes few hours for these parameters to retrieve progressively their initial values. Similar issues where mentioned in ref. [45]. For these reasons, the LN2 filling was operated manually during all measurements. An exception lies for the 7-days long vertical scan which was performed with the LN2 automatic fill system.

4.1 Energy resolution

Analog energy resolution was measured with a spectroscopic amplifier set to 6 μs shaping time, the source was placed near the segment with a total count rate below 1000 Hz. All channels where not measured due to time schedule. Low-energy resolution measurements were performed with a ^{241}Am source.

Digital energy resolution was measured with TNT2 boards during the calibration runs. The trapezoidal digital filtering parameters were:

- risetime length: 8 μs,
- flat top length: 4 μs,
- baseline reference: average of 4096 sampled points.

These parameters were optimized for improving the resolution with another detector in a former scan. For the 1332 keV measurement: two identical ^{60}Co sources were facing the opposite sides of the detector. The 122 keV line was measured with the same procedure using two ^{152}Eu sources. In both cases, the source-to-detector distance was set in order to have a Core total count-rate around 2000 ct/s.

The delivered cryostat had some noise issues affecting the resolution, mostly on the Core channel which is slightly above specification (see table 4.2). Most segment values were good enough but even so, better resolutions were obtained at Cologne, Liverpool and Saclay during customer acceptance tests. Values in table 4.2 are measured after a first step of repairing

	Core	Segments
FWHM @ 122 keV	1.35	1.30
FWHM @ 1332 keV	2.35	2.30

Table 4.1: AGATA specifications concerning energy resolutions. At 122 keV (1332 keV), the average segment energy resolution must be below 1.20 keV (2.15 keV).

which demonstrated that an improvement of the Core channel leads to better performances on all segments. Due to the limited time-scale of this PhD work the full scan of B006 has been performed in these conditions which are good enough to perform scans and validate the PSCS technique.

4.2 List of scans

All scans performed on B006 and analyzed in this work are listed in table 4.3.

4.3 Photopeak area with ^{137}Cs source, single scans

4.3.1 Central Core contact

The 662 keV photopeak net area of the ^{137}Cs source is determined for each collimator position, as shown in fig. 4.1. The area variations are due to both detector geometry and Compton scattering. The probability for a Compton scattered secondary gamma to escape the detector is much higher if the primary interaction occurs near the external surface, resulting in a decrease of the full-energy peak intensity near the outside boundary. The hexagonal shape arising in fig. 4.1(a) is a result of the detector front-face tapering which can be seen in fig. 4.1(b).

An unexpected effect on the vertical scan is the slight efficiency decrease along the section interfaces. It means that in this specific region, some full-energy deposit events lead to incomplete collection, so that they do not contribute to the photopeak area. This behavior is not visible on the horizontal scan, probably because of the lower granularity of the scan and due to volume effects. Also, the blank point on the center of the detector on the vertical scan is due to the impossibility for the analyzing routine to perform a coherent fit. The γ-ray spectrum is very odd in this precise point where all the segmentation lines are crossing: the photopeak line is very low, with a non-Gaussian shape and a large tailing between 640 keV and 662 keV. This affects also the horizontal scan with a lower photopeak intensity at Y=0 in the front of the detector. In the latter case, the effect is moderate because this odd area is small compared to the amount of HPGe crossed by the collimated beam.

These types of charge collection issues are discussed in details in section 4.6.

4.3.2 Segments

A similar analysis was carried out considering each segment individually. The results for the vertical scan are shown in fig. 4.2, gated on the 36 segments. The external shape of the

		DIGITAL		ANALOG	
channel	segment	@ 122 keV	@ 1332 keV	@ 60 keV	@ 1332 keV
0	CORE	1.74	2.78	1.47	2.31
1	A1	1.29	2.52		
2	B1	1.26	2.22	1.1	
3	C1	1.20	2.12		
4	D1	1.23	2.21		
5	E1	1.20	2.20		
6	F1	1.28	2.15		
7	A2	1.14	2.47		
8	B2	1.19	2.24		1.81
9	C2	1.07	2.24	0.98	
10	D2	1.19	2.24		
11	E2	1.12	2.21		
12	F2	1.17	2.14		
13	A3	1.16	2.30	1.04	
14	B3	1.23	2.01		
15	C3	1.12	2.08		
16	D3	1.21	2.11		
17	E3	1.13	2.17		
18	F3	1.15	2.14		
19	A4	1.22	no data		
20	B4	1.21	2.26		
21	C4	1.18	2.28		
22	D4	1.21	2.26	1.03	
23	E4	1.15	2.23		
24	F4	1.19	2.20		
25	A5	1.24	2.42		1.96
26	B5	1.28	2.23		
27	C5	1.22	2.20		2.01
28	D5	1.26	2.21		
29	E5	1.21	2.15		1.82
30	F5	1.20	2.18	1.04	
31	A6	1.17	2.30		
32	B6	1.11	2.15		
33	C6	1.15	2.12		
34	D6	1.17	2.15		1.90
35	E6	1.19	2.15	0.97	
36	F6	1.13	2.08		1.82
mean value		1.18	2.21		

Table 4.2: Energy resolution (FWHM values in keV) obtained with digital and analog electronics. Values labeled in red are out of specification.

	Source	Mode	Pitch [mm]	Timeout [s]	Number of points	Total time [days]	Volume of raw data [Go]	Remarks
VERTICAL POSITION								
1	^{137}Cs	E	1	100	5520	7.5	260	charge collection analysis
2	^{137}Cs	M	2	110	1310	2	1 500	PSCS
3	^{137}Cs	E	0.2	150	300	0.6	22	check for vertical tilt 4×
4	^{241}Am	E	0.05	60	160	0.1	41	segmentation line analysis
HORIZONTAL POSITION								
5	^{137}Cs	M	2	110	1840	2.7	1 400	PSCS 0°
6	^{137}Cs	M	2	120	1840	3	1 500	PSCS 90°
7	^{137}Cs	E	0.2	150	400	0.8	25	check for lateral tilt

Table 4.3: List of scans used in the present work with several pieces of information concerning scanning parameters. In the "Mode" column, E stands for energy only and M for mixed mode (energy + pulse-shape readout). Scan number 1 is the only one which was performed using the LN2 autofill system which creates slight issues concerning energy resolutions.

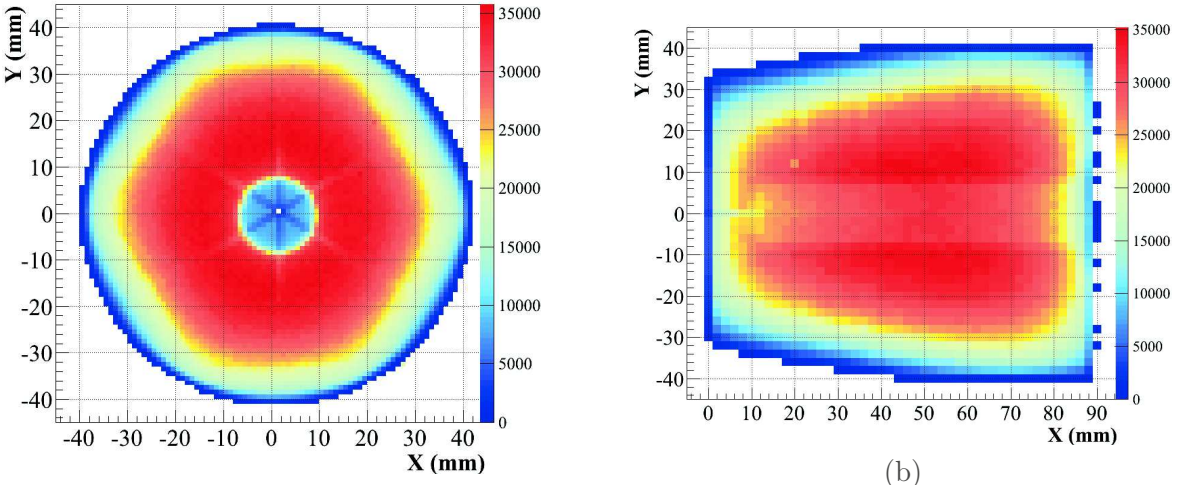

(a) (b)

Figure 4.1: Distribution of the Core 662 keV photopeak net area as a function of the position of the collimator for the vertical (a) and horizontal (b) scans performed with a 1 mm pitch and a 2 mm pitch, respectively.

crystal is precisely reconstructed. The intensity profile of slice 1 is completely determined by the segment geometry. For slices 2 to 6, the incoming γ-rays are attenuated by the front slices. The outer ring of these slices is very intense compared to the central hexagonal part. This is a result of the tapered crystal shape: front slices absorb most of the γ-rays along the central part whereas the outer ring is directly illuminated by γ-rays.

The internal segmentation lines of slice 1 are determined by the front face external seg-

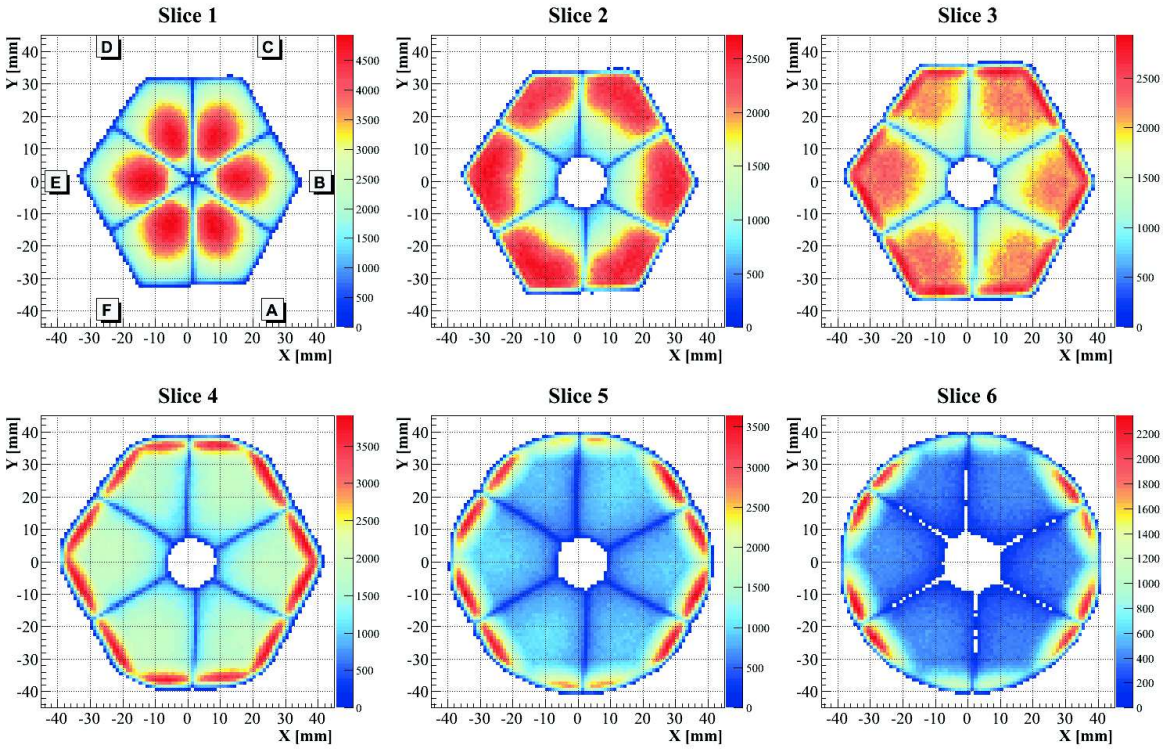

Figure 4.2: Distribution of segments 662 keV photopeak net area as a function of the position of the collimator for the vertical scan performed with a 1 mm pitch.

mentation. Segment boundaries within the bulk are bent due to the tangential mobility anisotropy of charge carriers, so that they are not aligned towards the central point. The segment boundaries are not identical for each slice. This can be seen by looking at the point (X=20, Y=10) on each slice: the segmentation interface between sections B and C is moving a few millimeters towards negative Y. This behavior could be due to the asymmetric shape of the crystal or possibly to variation of electric field and impurity gradient along the crystal length.

Figure 4.3 shows the horizontal scan, where only segments of sections B and E are plotted. There is again an important attenuation effect toward each sector center due to the γ-ray attenuation within sectors C and D before reaching sectors B and E, respectively. Segments also present a very reduced HPGe volume near the bored hole, which results in a lower intensity in this area. This explains also the void on the front face of the detector. Sector E is on average more intense than sector B because of the larger size of segments shown in panel (b), which results in a larger detection volume. This figure allows to check the segment geometry along the Z axis of the detector, i.e. the X axis of the scan. Due to the electrical field lines, the volume segmentation is far more complex than the external segmentation pattern. The 2D segmentation defines an external depth of 8 mm for the first slice, but this one goes quite deeply toward the bored hole, resulting in a maximum depth around 16 mm, close to the central hole (see fig. 4.3). As a result, slice 2 is very thin in the center of the crystal and

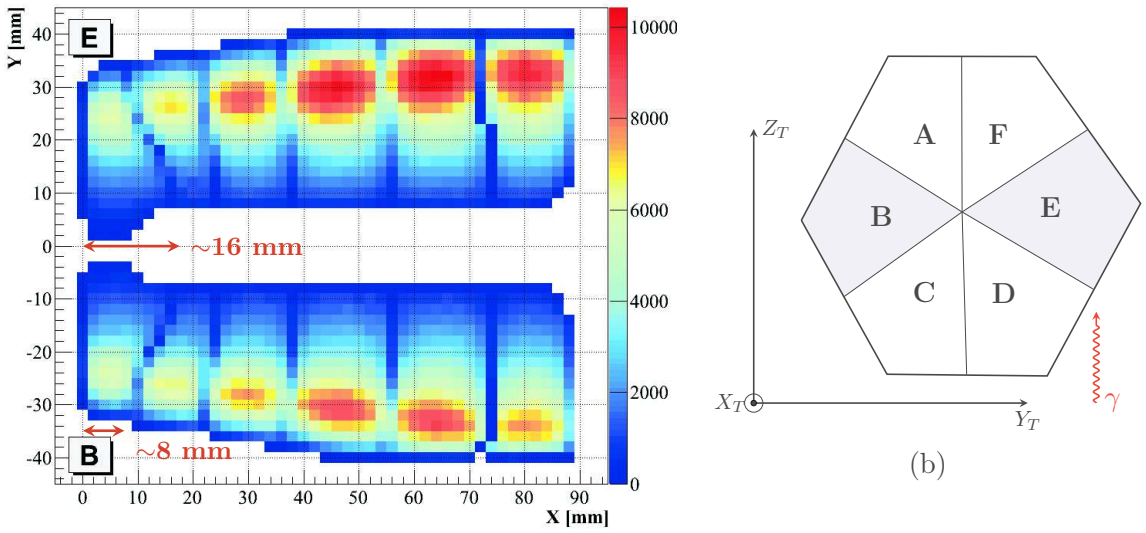

(a) (b)

Figure 4.3: Panel (a): distribution of 662 keV photopeak net area for each segment of sectors B and E as a function of the collimator position for the horizontal scan performed with a 2 mm pitch. Panel (b) shows the crystal orientation and the γ incident direction.

provides a lower detection efficiency compared to the other slices.

4.4 Charge collection characterization

Charge collection characterizes the ability for charge carriers to be collected by the electrodes within the integration time of the readout system. The more efficient and homogeneous the charge collection, the better the final spectrum resolution. Generally, these collection issues affect both electrons and holes, and result from non-uniform distribution of electric field, drift lengths or defects in the crystal. It is possible to characterize such behavior by looking at the slight peak-position shifts as a function of the scanning position.

4.4.1 Peak position distribution of the Core spectra, in the Ge crystal bulk

The peak position of the ^{137}Cs line measured with the Core signal is plotted in figures 4.4 (a) and (b) for a front and a side enlightening, respectively. For clarity, the energy calibration is set such that the average peak position among all scanned points is 661.7 keV. Some vertical lines appear on panel (a) as a result of the influence of the LN2 autofill system, this scan only is concerned by such slight trouble. The maximum amplitude between two points is 1.2 keV but most points are within a 0.5 keV range. This behavior is normal and emphases the drawback of using large volume detector instead of small ones: as charge carriers have a larger drift distance until the collection, they are more sensitive to trapping. Also it is more

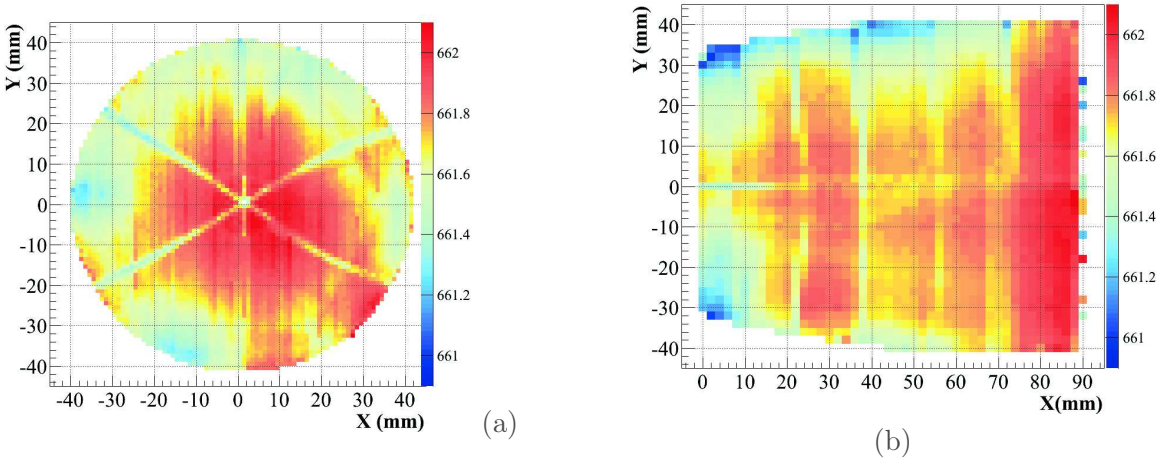

Figure 4.4: Distribution of Core 662 keV photopeak centroid position as a function of the position of the collimator for the vertical (a) and horizontal (b) scans.

probable to see inhomogeneities in large volume of HPGe. For these reasons large volume detectors have a slight degradation of the energy resolution compared to small ones.

No clear correlation can be found between the crystallographic orientation and peak position shifts, meaning that, with an integration time long enough, both effects are independent. Both figures show clearly that, on average, the peak position is higher near the bored hole than near the external contact. It means that charge collection is more efficient when the interaction occurs near the bored hole. As the Core contact collects the electrons, a first approximation is that there is an electron trapping which is related to the mean distance traveled by the electron cloud until collection.

A striking effect is that internal segmentation lines appear as a result of an incomplete charge collection from the Core point of view. Probable reasons of this effect will be investigated in detail in the next section.

4.4.2 Peak-position distribution gated on segments

4.4.2.1 Core spectra

It is possible to investigate locally the Core response using the segments as gates. Figure 4.5 shows the Core peak position gated on 1-fold, 662 keV, full energy deposits. Raw results are plotted on panel (a). Despite only one channel is analyzed, the Core one, peak positions coming from the coincidence with specific segments have a constant shift, leading to a higher centroid position. This is obvious for segments A6 and B6 for example. This kind of effect has already been observed in ref. [45] and was attributed to electron trapping. However, the work presented here shows that this behavior is localized in the whole volume of some segments. Trapping cannot explain such behavior and it is more likely that it is due to an electronic effect.

In order to make a proper analysis, peak positions corresponding to each segment were

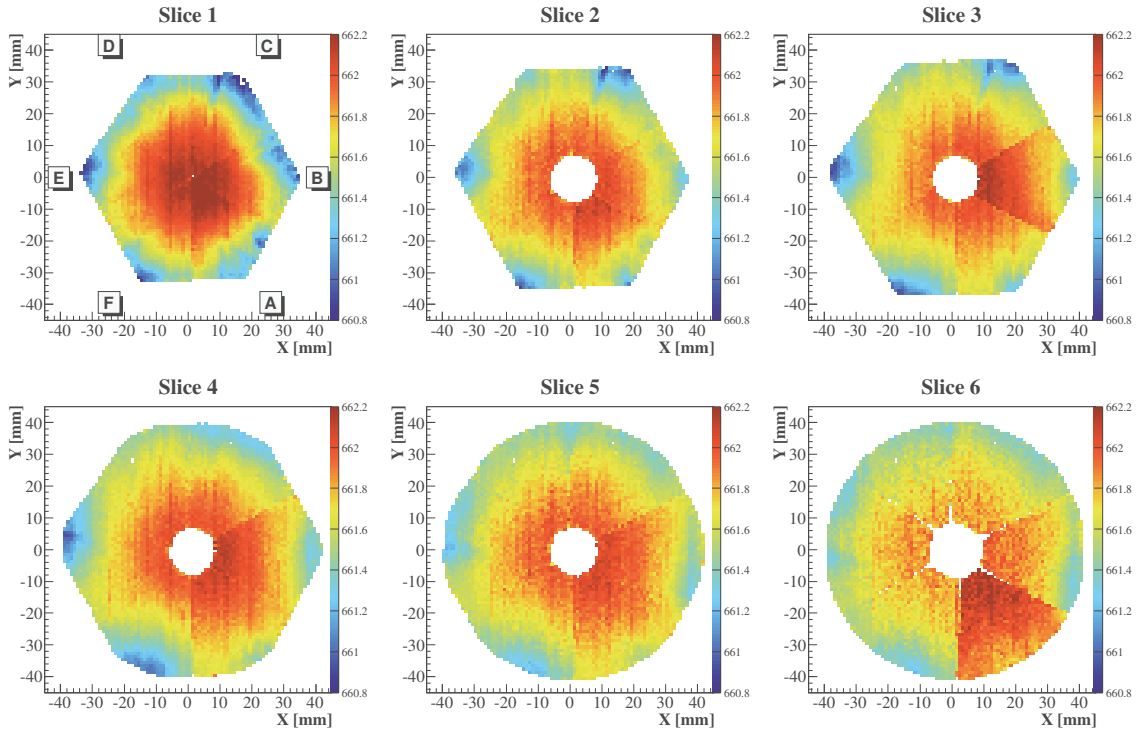

(a)

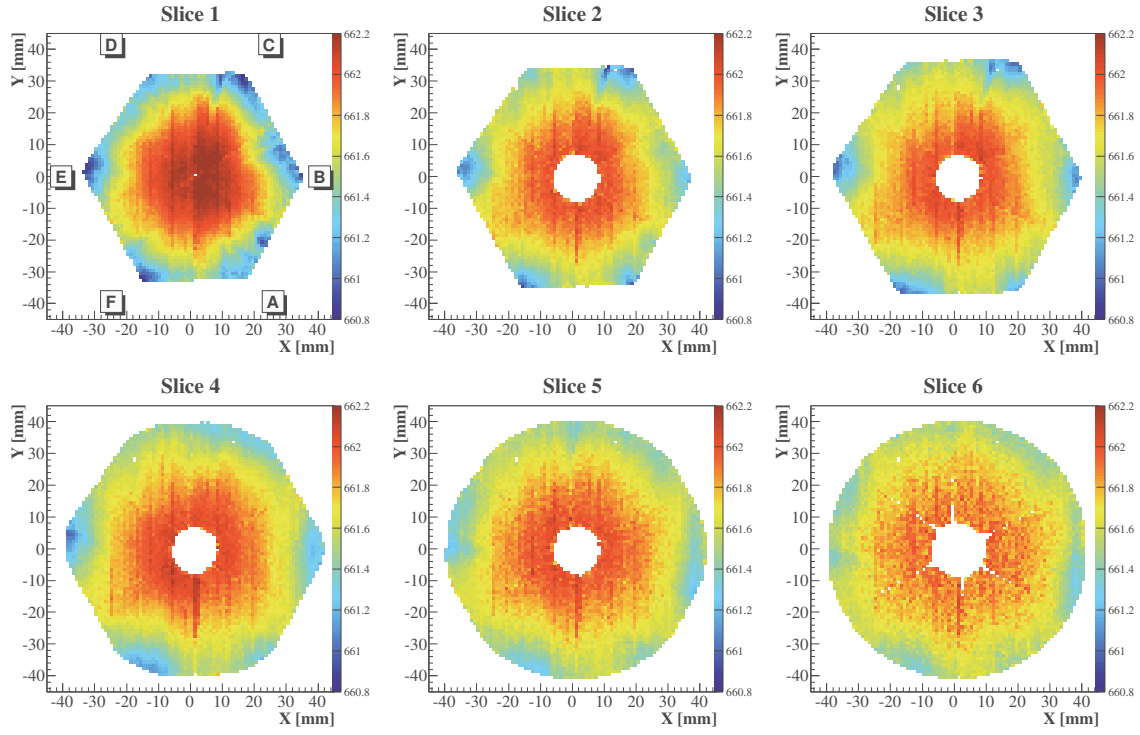

(b)

Figure 4.5: Distribution of the Core 662 keV photopeak centroid position gated on 1-fold events in the 36 segments as a function of the position of the collimator. Panel (a): raw data revealing shifts localized in several segments, panel (b): for each segment region, the average centroid is normalized to 661.7 keV for analysis.

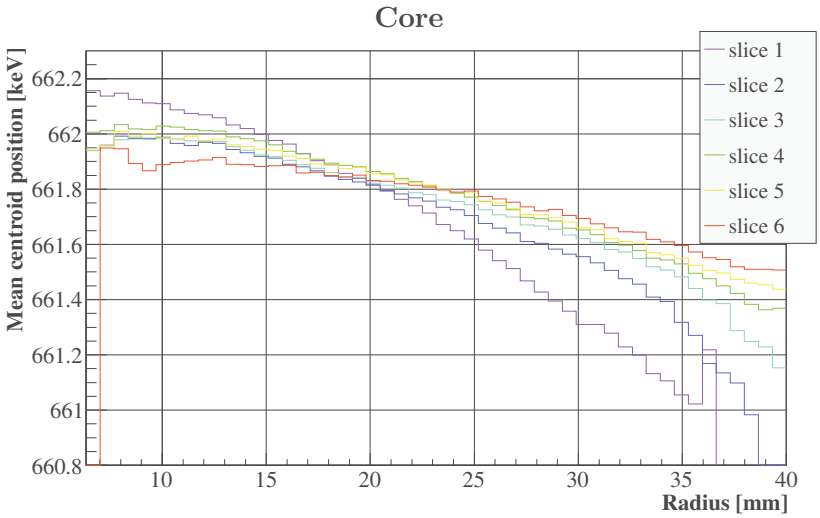

Figure 4.6: Distribution of average Core 662 keV photopeak centroid position gated on 1-fold events in the 6 slices as a function of the interaction radius.

normalized such that the global mean is 661.7 keV. The result is shown in fig4.5(b). For each pixel of this figure, the corresponding radius is computed. The mean Core centroid shift is plotted as a function of the interaction radius in fig. 4.6. Some trends are observed in these figures:

- anywhere in the crystal, the centroid is higher near the bored hole than near the external electrodes,
- centroid values decrease even more in the corners of the tapered region,
- the amplitude difference between the highest and the lowest centroid value decreases from the front hexagonal slice to the rear coaxial slice.

This is a characteristic of electron trapping in the crystal. When electrons have more distance to travel, i.e. for large radii, there is a charge deficit because some of them are trapped along the trajectory and remain uncollected during the electronics integration time. The energy readout is then slightly lower than expected. As trapping is highly related to the electric-field strength, this effect is enhanced on the hexagonal edges where the electric field magnitude is lower. For the same reason, trapping is larger in front slices than in rear slices. The density of impurity is lower on the rear than on the front, which leads to electrical-field strengths more homogeneous in the rear (see fig. 2.1(a)), and finally to less trapping, i.e. a better charge collection.

4.4.2.2 Segment spectra

A similar centroid versus radius analysis was carried out for each segment channel, and is shown in fig. 4.7. Centroids of slices 2 to 6 are almost constant along the radius, which means that segments are less sensitive to electron trapping than the Core. This is what is expected because electrons drift toward the center of the detector where the segments weighting potential decreases, such that electrons are mostly trapped in regions where their

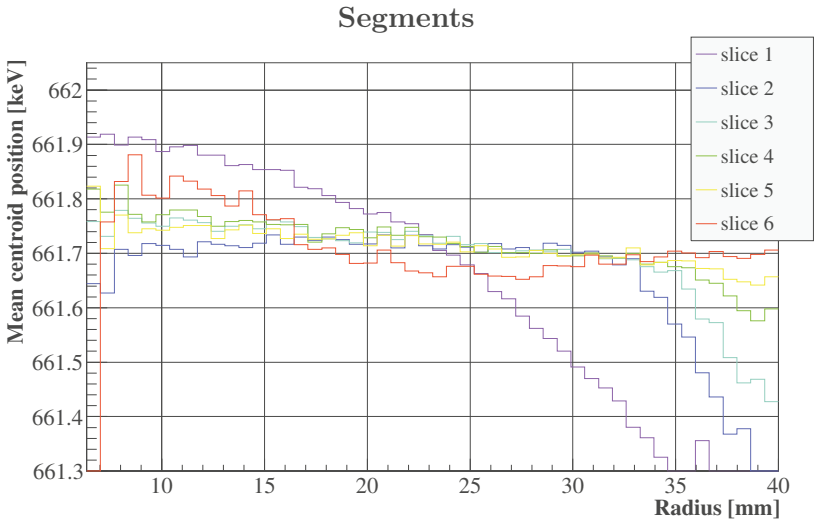

Figure 4.7: Distribution of average segments 662 keV photopeak centroid position gated on 1-fold events in the 6 slices as a function of the interaction radius.

contribution to segment signals is low. However, there is a bump for large radii in slices 2,3 and 4, where centroids decrease abruptly. This bump corresponds to radii located in the edges of the hexagonal tapering. As explained previously, electron trapping is enhanced in this area because of the lower electric field and longer drift path. It is also a region where the segment weighting potential is high, so that any trapped charge has a large effect on the final readout energy.

This analysis concludes to a global electron trapping in the crystal, which is known in n-type HPGe. It reveals also that a tapered crystal induces complex electric-field distributions and inhomogeneities. The resulting energy resolution is therefore slightly worse than a more classical detector (non-segmented p-type). A hole trapping behavior, which characterizes neutron-damaged detectors, would lead to a reversed slope in fig. 4.6 and 4.7.

4.5 Signal risetime

Pulse-shape risetime is also a way to characterize charge collection but in a different time scale. Centroid shifts correspond to an energy measured after 8 μs integration whereas risetimes are measured on pulse shapes with a timescale typically around 0.5 μs. A parameter which defines the risetime is the T90: it corresponds to the time needed for the signal to rise from 10% to 90% of its maximum amplitude (also noted T_{10-90} or T_{10}^{90}). It is generally considered as a rough estimation of the total duration of the pulse. T90 values are averaged for each segment, among the pulse shape distributions of the vertical scan (2 mm pitch).

4.5.1 Core T90 risetime distribution

The Core weighting potential has a quasi-cylindrical symmetry, slightly affected by the external complex geometry of the tapered crystal. The response should then be driven mostly

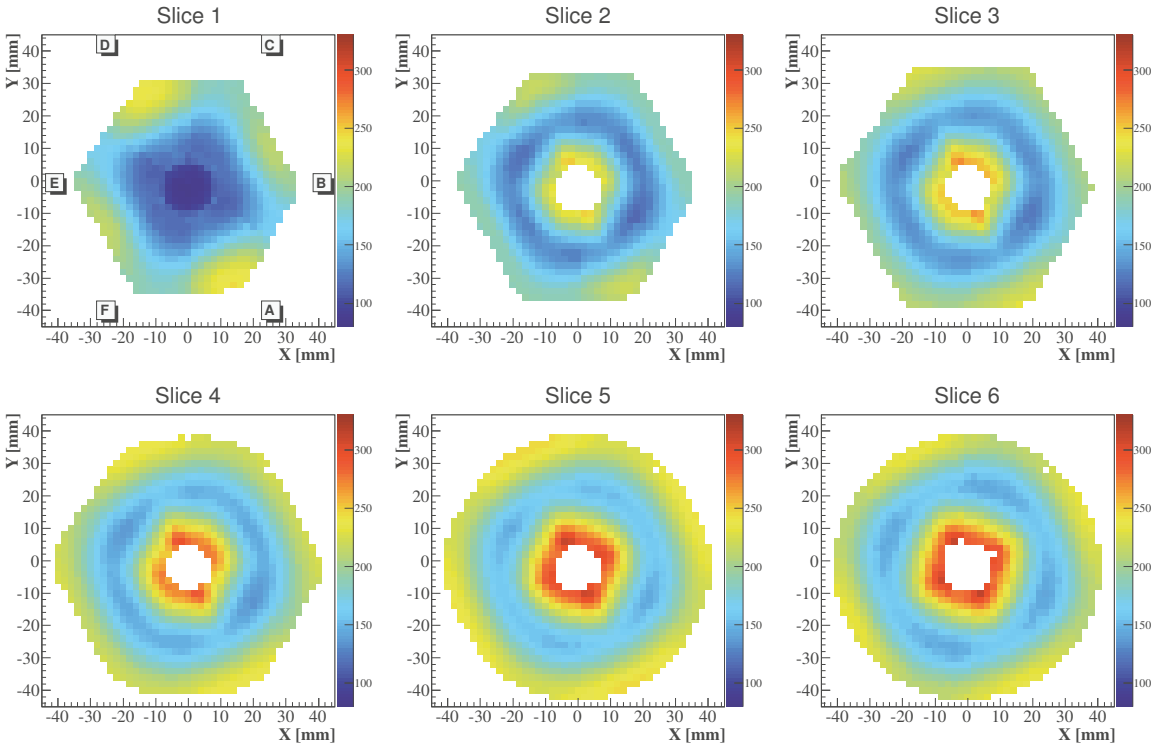

Figure 4.8: Core T90 [ns] distribution for each slice of the detector.

by radial variations with few angular dependence. The core T90 distribution is shown in fig. 4.8. The fastest risetime occurs on the "semi-planar" region between the center of the front face of the detector and the bored hole (slice 1). There, the drift path is very short and the electric-field magnitude is large, leading to the fastest charge collection. For slices 2 to 6, the fastest risetime occurs for intermediate radii where both electrons and holes need the same time to reach their collection electrode, considering the electric-field distribution and their associated drift velocities. The longest risetime occurs at minimum and maximum radii because electrons and holes, respectively, have to drift through the whole detector radius.
For the hexagonal-shaped first slices (number 1-3), the Core risetime is barely affected by this complex external geometry. A square symmetry arises clearly, which results from the longitudinal mobility anisotropy of charge carriers in Ge lattice. As both holes and electrons have the fastest drift velocity along the <100> axis and a slower one along the <110> axis, both contribute to have extrema localized along the same orientation, leading to such pattern. This effect is even more important in the first slice, where the electric field drives charges to drift along the slowest <111> axis. This property will be used in section 4.5.3 in order to check the crystallographic axis orientation.

4.5.2 Segment T90 risetime distribution

The 6 segments of the forward slices have slight variations of their weighting potential distribution, due to the crystal asymmetry. Nevertheless it results in an hexagonal symmetry due to the repetition of a similar pattern for each segment of a given slice. The risetime map of the segment (shown in fig. 4.9) is then a combination of the hexagonal symmetry due to the segmentation, and the square symmetry due to the mobility anisotropy of charge carriers. Same considerations as for the Core map are valid concerning pulse-shape durations.

4.5.3 Crystallographic axis orientation determination

Checking the crystal axis orientation is very important because, as seen in the previous sections, charge carrier mobility anisotropy affects significantly the pulse shapes. The right alignment has to be taken into account in pulse-shape simulations for proper PSA treatment.

AGATA HPGe crystal specification defines the <100> axis oriented along the corner of segment A. In reality, the slower axis <110> had been mistakenly aligned with A corner for the first manufactured AGATA crystals; it was then decided to keep this alignment for the following manufacturing. This modification has no major effect on the global detector performance but it has to be considered for pulse-shape simulations. The cylindrical coordinates are set with the same origin as the Cartesian coordinates, as shown in fig. 4.10(a). Angle $\phi = 0$ is on the X axis, ϕ varies from 0° to 180° anti-clockwise. Because of the asymmetry of the crystal front face, the corner of segment A is localized at $\phi \sim 63°$ in cylindrical coordinates. This value is measured with the use of scanning data such as fig. 4.1 and 4.9. The T90 parameter is plotted as a function of the angle ϕ for a fixed radius in fig. 4.10(b). Periodic variations arise from the alternate of fast and slow equivalent crystallographic axes. The distribution of T90 values is fitted versus ϕ over the $-180° < \phi < 180°$ range with a periodic function described in [39]:

$$\mathrm{T90} = \mathrm{A} + \mathrm{B}(1 + \mathrm{R_{an}}\cos(4(\phi - \phi_0))(1 + \mathrm{R_{geo}}|\sin(3\theta)|)) \tag{4.1}$$

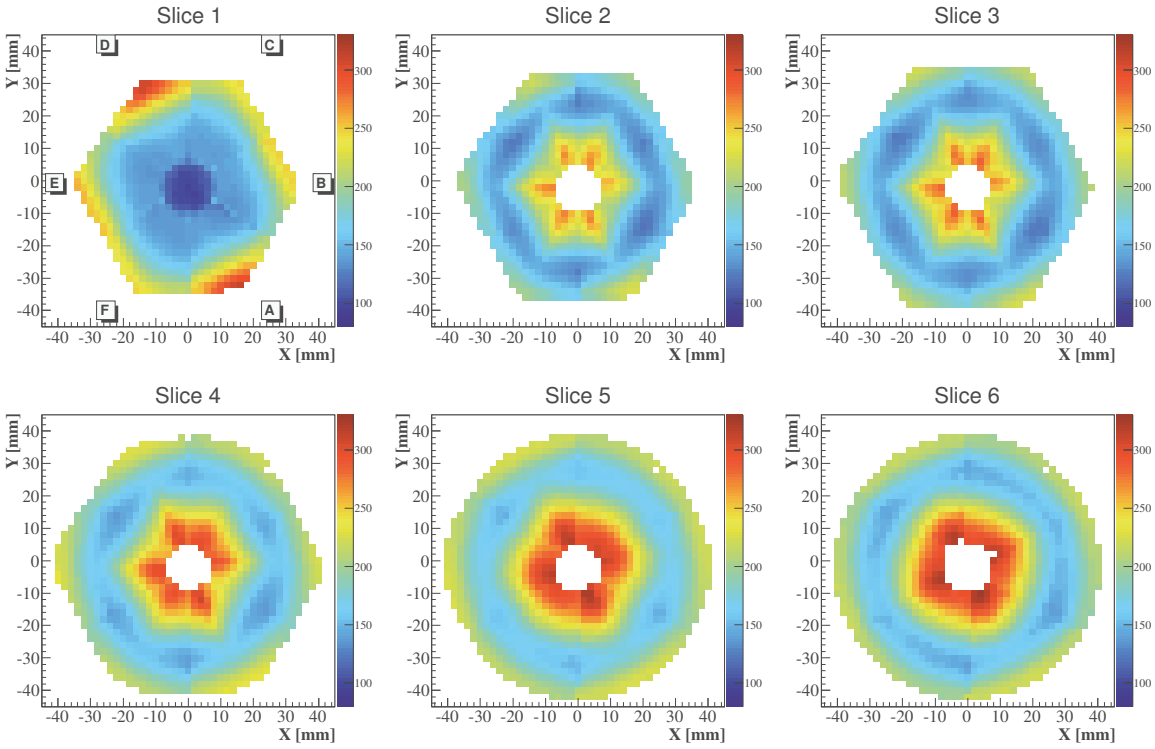

Figure 4.9: Segment T90 [ns] distribution for each slice of the detector.

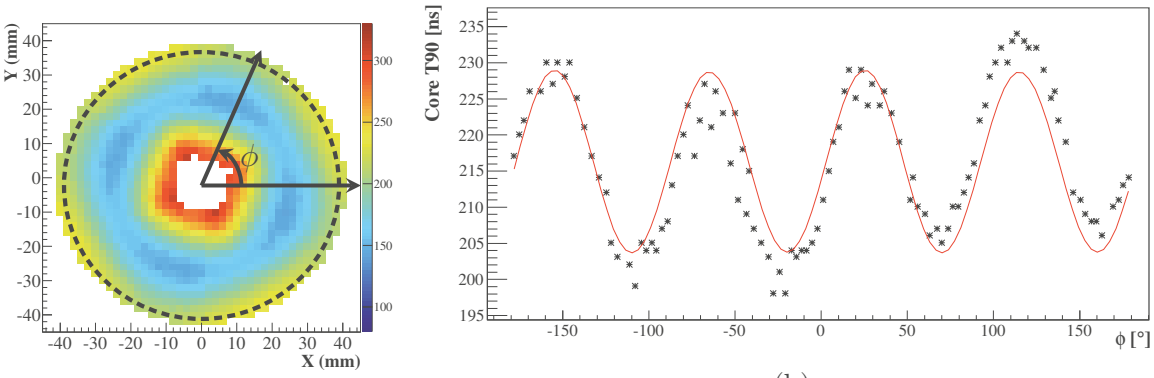

(a) (b)

Figure 4.10: (a) Core T90 of slice 6. Each pixel or the scan grid the closest to the dotted line are plotted in (b) with crosses, as a function of the azimuthal angle ϕ. The red line corresponds to the fit of eq. 4.1, used for an accurate determination of the maximum around -65°.

slice	T90 Core <110> position	T90 segment <110> position
1	-65.2° ± 0.6	-65.6° ± 0.9
2	-65.5° ± 1.1	-67.3° ± 1.4
3	-64.0° ± 1.8	-61.8° ± 2.6
4	-65.4° ± 1.5	-65.7° ± 2.6
5	-65.6° ± 0.9	-65.2° ± 2.3
6	-64.5° ± 0.6	-63.1° ± 1.8
average	-65.0° ± 1.1	-65.4°± 1.9

Table 4.4: <110> axis orientation results. Axis <110> is expected to be aligned with -63°.

where A and B are fitting parameters. The first factor describes the four fold symmetry of the charge mobility anisotropy and the phase shift θ_0 which gives the crystal orientation. The second factor accounts for a symmetric hexagonal cut shape geometry of the detector. The irregular distribution of the points around the fitted curve from eq.4.1 is due to the fact that the scan grid do not follow the dotted circle. The experimental points chosen are the closest to the dotted circle. The position of the maximum is determined for each slice by analyzing both Core and segment risetimes. Core risetime variations along the azimuth are much smoother than segment risetime variations. This leads to a more accurate result for the Core analysis. Results are listed in table 4.4.

Table 4.4 shows that the <110> axis is well aligned towards the corner of section A at -65° which is in the capsule specifications (given this reference coordinates: -63° ± 3°). This result agrees with data coming from similar measurements published in ref. [60, 61] even if in the latter the conclusion disagrees.

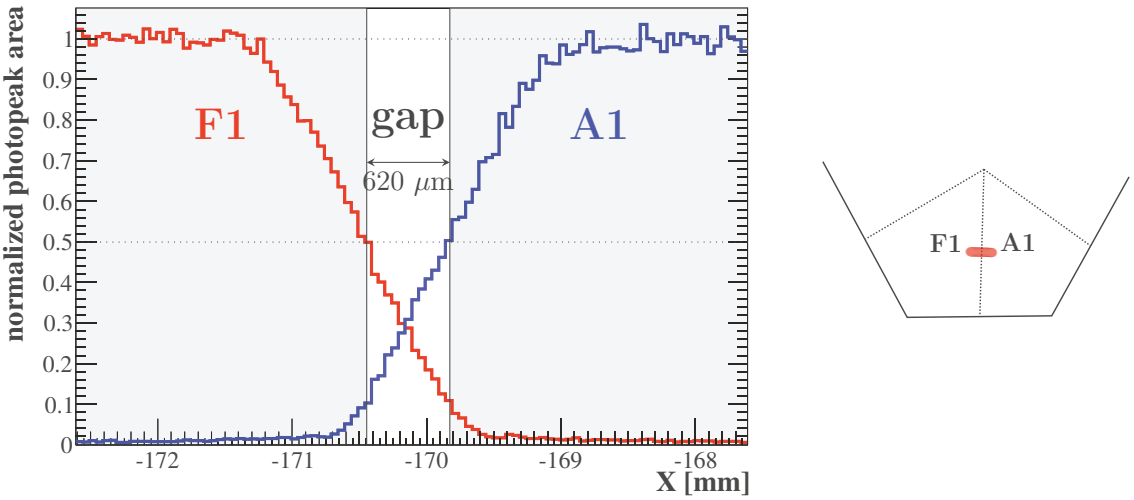

Figure 4.11: Normalized ^{241}Am photopeak area measured in segments F1 and A1 along the inter-electrode gap. The pitch between two points is 50 μm and the location of the scanning line is shown in the right panel.

4.6 Inter-electrode gap investigation

The passivated area separating two neighboring segment electrodes is called inter-electrode, or inter-segment line. Results of these subsection derive mainly from the data analysis of a fine ^{241}Am scanning line across the inter-electrode line between segments F1 and A1 on the front face of the detector. The scan with 50 μm pitch was perpendicular to the inter-electrode line (see right panel of fig. 4.11).

4.6.1 Gap width

Two neighboring-segment boundaries are determined with the methodology described in section 3.4.4. The distance between their limit is a measurement of the gap width. Figure 4.11 shows the ^{241}Am normalized photopeak area of segments A1 and F1 as a function of the position of the collimated beam. Since both curves are symmetric, segments behave in the same manner, as expected. A linear fit of the raising edge of both slopes is performed which results in a segment F1 boundary localized at X = -170.45 mm and segment A1 limit localized at X = -169.83 mm, corresponding to a gap width of 620 μm. Due to statistical variations between each photopeak area, there is an uncertainty on the normalization, which leads to a typical uncertainty of 50 μm on the measured gap width.

Several similar measurements were performed on the front face of the detector, on A1/F1 and D1/C1 interfaces, mainly for the vertical rotation check (see section 3.6.1). The resulting gap width, averaged over 10 measurements in various locations, is 640$\pm$30 μm (see fig. 3.9). The width distribution is homogeneous which means that the inter-segmentation line has a constant width along its whole length.

Following AGATA crystal specification, the gap between two electrodes is physically of 500 μm. Although slightly larger, the value measured in this work is very consistent given

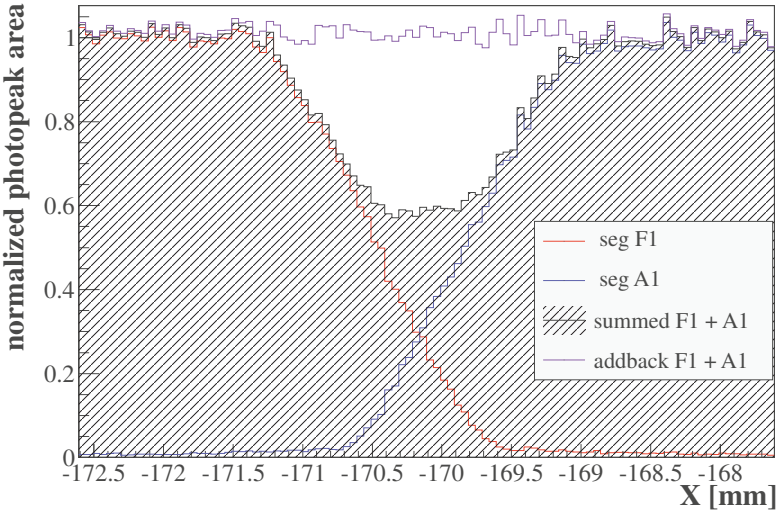

Figure 4.12: Same figure as 4.11 with photopeak area of A1/F1 summed spectra (filled area) and add-back spectra (purple line).

uncertainties and possible side effects taking place in this region (discussed in following sections).

4.6.2 Photopeak area

A deficit in the photopeak is observed when the energy is deposited on the inter-electrode: the same figure as 4.11 is plotted with additional information in fig. 4.12. In a first step, one can consider that counts in segments A1 and F1 are independent events. When the photopeak area of segments A1 and F1 are summed, there is a large count deficit leading to a loss of up to 40% (see hatched area in fig. 4.12). In a second step, two fold events in A1 and F1 are supposed to be correlated and the segment energies are summed in a single spectrum (add-back mode). The missing counts are retrieved (purple line in fig. 4.12), showing that there is no loss of active volume in the inter-electrode region, but an energy split between two electrodes. Note that the photopeak area of the segment add-back spectrum is computed with an integration over a wide energy range 55 keV $<$ E $<$ 62 keV, which means that there is still somehow an energy loss.

An easy explanation of such effect is to consider Compton scattering between neighboring segments. However, γ-ray interactions at 60 keV are dominated by photoelectric effect and only 20% of γ-rays undergo scattering, both Compton and coherent scattering included. In the case of scattering, the secondary very low energy γ-ray (below 12 keV) is unlikely to cross hundreds of micrometers of germanium. It would then hardly deposit energy in two segments. Note that the loss of counts it strictly limited to collimator positions X where the γ-ray beam crosses the inter-electrode. Figure 4.13(a) shows the Core centroid evolution versus X, which is affected by incomplete charge collection: there is a slight energy deficit which reaches 0.1 keV in the worst case, that is to say 0.17% of the energy. This is one decade larger than what is expected with Core/segments crosstalk [45] and cannot be attributed to

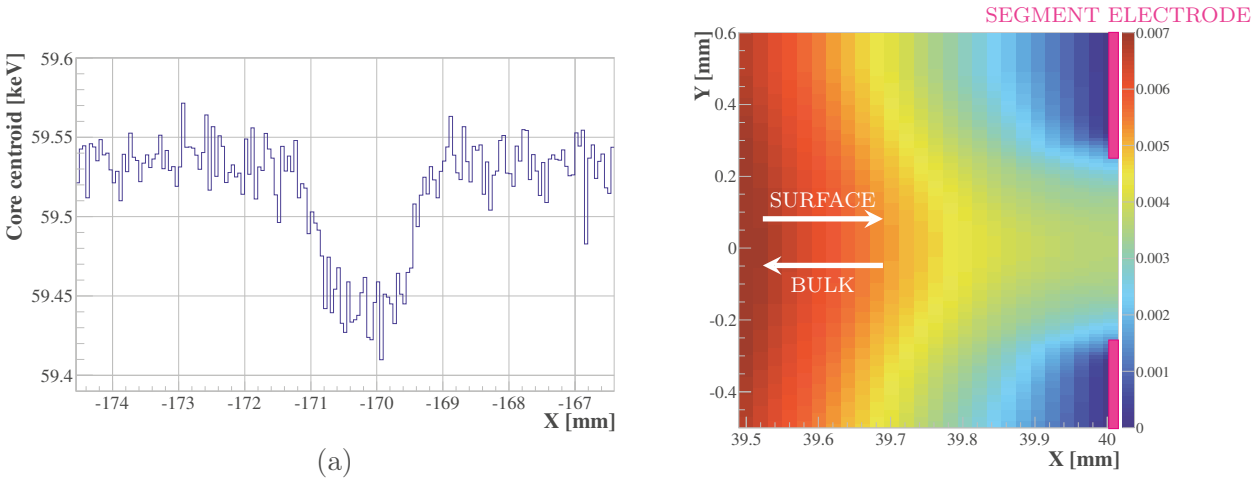

(a) (b)

Figure 4.13: (a) Core ^{241}Am centroid as a function of the collimator position across the inter-electrode gap, (b) Core weighting potential distribution near the crystal surface along the segment inter-electrode gap. It is slightly higher than zero on the gap.

Compton scattering.

4.6.3 Charge sharing on inter-segment gap

Inter-electrode charge sharing have already been observed on planar segmented detectors [62, 63, 64] but also on AGATA detectors [65]. When the charge cloud resulting from a single γ-ray interaction reaches the inter-electrode gap, the energy is split between neighboring electrodes, and a global energy loss is observed. Various scenarii exist to explain the evolution of the charge cloud:

1. The inter-electrode area is naturally charged, resulting in a potential which is different from the grounded neighboring electrodes. A sufficient transversal electric field is created, which drives charges towards the electrodes. This scenario hardly explains how the cloud can be split between two electrodes.

2. There is no sufficient transversal electric field, charges reach the surface and are blocked during a much longer time than the energy integration and readout time (few μs). The measured energy corresponds to weighting potential value of both neighboring segments at the location of the blocked charge cloud. As it is very close to electrodes, the weighing potential is close to 1, which means that the full energy is almost reached. Same consideration is true for the Core; following Shockley-Ramo theorem, the Core hole contribution is not zero until they are collected. There is therefore an energy deficit due to holes, which is very low because they are located where the Core weighting potential is close to zero.

As a matter of facts, there is an energy loss of the Core for such collection process. It is clearly shown on fig. 4.13(a): there is a 0.17% energy deficit in the Core when the γ-

ray spot illuminates the inter-segment gap. This value is even lower than the simulated Core weighing potential value near segment electrodes which is about 0.35%, see fig. 4.13(b). This is because the γ-ray spot is larger than the inter-electrode gap, resulting in a readout value which is an average between inter-electrode events and classical events, as shown in fig. 4.14(a). One can approximate the situation as follows: one half of the pencil beam crosses the inter-electrode with a 0.35% energy deficit and the other half crosses the electrodes with full energy measurement. The resulting peak has a centroid with 0.17% energy deficit and larger resolution compared to a normal measurement. This is effectively what results from these measurements.

Data from a measurement with a ^{241}Am pencil beam centered on the inter-segment gap are plotted in a 2D-plot in fig. 4.14(b). The sum of A1 and F1 segment energies versus F1 energy counts along the diagonal corresponds to interactions happening only in segment F1. Counts along the vertical line at $E_{F1} = 0$ correspond to interactions happening only in segment A1. Both lines are due to the sides of the beam spot enlightening these segments (fig. 4.14(a)). There is a third region on the top of fig. 4.14(b) where almost full photopeak energy is reached by sharing the energy between both segments. These counts correspond to interactions at the inter-electrode and are assigned to charge sharing which follows the second scenario.

The segment sum energy of this 2D-plot is shown in fig. 4.15. A double peak is clearly seen and well fitted with a double Gaussian function. The high-energy part is related to the γ-beam spot fraction illuminating segments A1 or F1. The low-energy part corresponds to γ-beam spot fraction illuminating the inter-electrode. Indeed the low-energy component represents 48% of the double-photopeak area. It means that inter-electrode events have almost a constant energy deficit which corresponds to the projection on Y axis of the distribution of counts in region 3 of fig. 4.14(b). Most of the counts are centered at low energy and only few counts are placed between the low and full-energy component. The difference between both photopeak centroids is $\sim$4.2 % of the full energy (see table 4.5). Both FWHM are large due to noise summing and proportional cross-talk. We can conclude that inter-electrode events are identified when the segment sum energy of 2-fold events is too low compared to the Core energy to be due only to cross-talk (difference larger than 4%). This explains why the full energy in add-back mode is recovered by using a large integration window (55-62 keV) as mentioned before.

A possible third scenario is that charges at the surface undergo drift at the surface. After reaching the inter-electrode gap, they drift towards the electrodes with an abnormally long drift time due to the reduced transversal component of the electric field. Energy losses would then be due to surface trapping. This case would hardly explains how can the charge cloud be split between segments but it explains the energy deficit. Near-electrode energy deposits on the inter-electrode gap would have on the closer electrode a large energy readout with few trapping and on the farther electrode small energy readout and large trapping. This would lead to a unique and broad photopeak shape with continuous energies depending on the hole-deposit location, on contrary to the double humped peak observed.

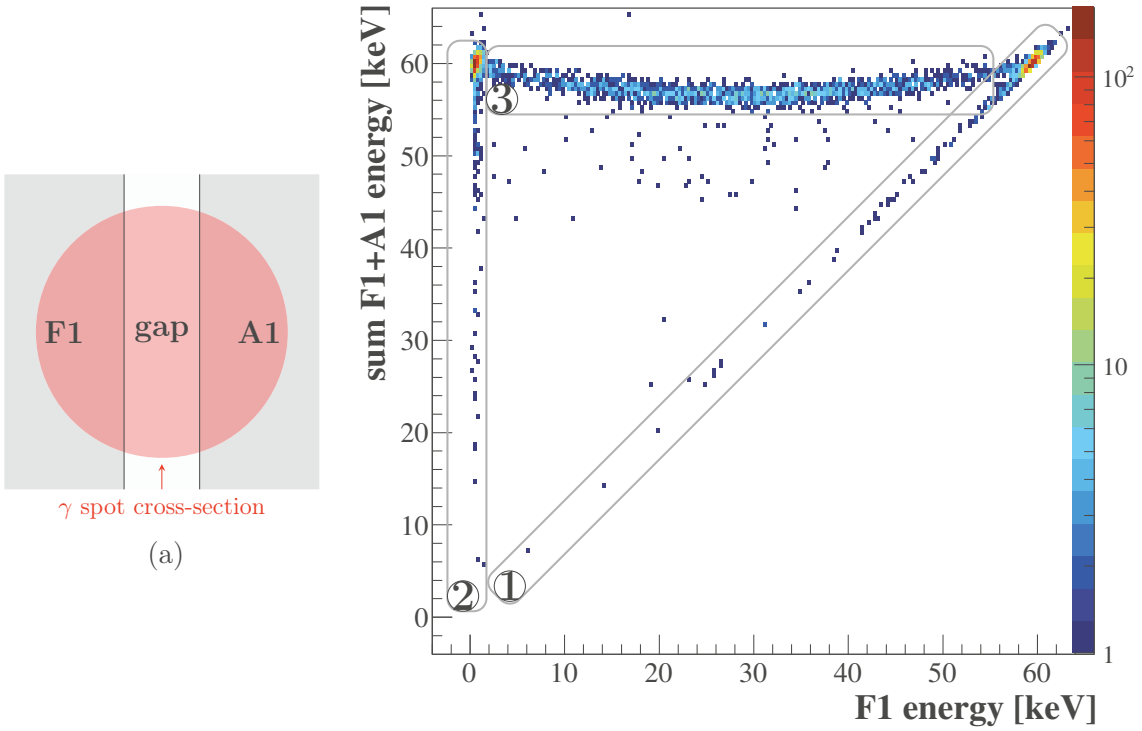

(a) (b)

Figure 4.14: (a) Cross-section of the γ-ray spot centered on the inter-segment gap. (b) 2D-plot with segments F1+A1 energy versus segment F1 energy for a ^{241}Am measurement corresponding to the one shown in panel (a). Typical regions are: 1) segment F1 spectrum, 2) segment A1 spectrum, 3) energy split between A1 anf F1.

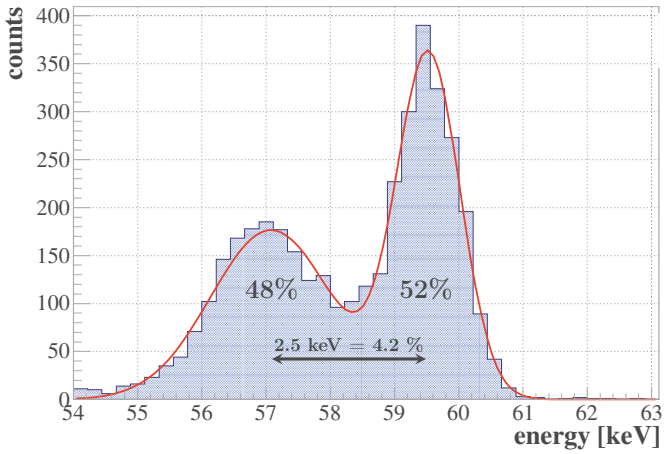

Figure 4.15: ^{241}Am add-back A1+F1 neighboring segments sum energy spectrum for the case of inter-electrode illumination (see fig. 4.14(a)). The red line is a double Gaussian fit which parameters are listed in table 4.5.

	Low-energy component	Full-energy component
Centroid [keV]	57.0	59.5
FWHM [keV]	2.20	1.16
Area [counts]	416	441

Table 4.5: Gaussian parameters of the fit of fig. 4.15.

4.6.4 Spectra shape along inter-electrode

Full spectra of F1, A1 and their add-back spectra as a function of the pencil beam position are plotted in fig. 4.16(a,b,c). A minimum threshold of 4 counts within each pixel is required in order to remove background. Energies below 5 keV are not shown because of the Core trigger threshold. Any event occurring in another segment than the one readout leads to noise detection typically < 5 keV. The low energy part of spectra in the 5 to 50 keV range in fig. 4.16(a,b) will be called *partial collection tail* in this section.

As the beam crosses gradually the inter-electrode from segment A1 to segment F1, there are 3 characteristic regions which are shown in fig. 4.16(a):

1. photopeak intensity is maximal, partial collection tail is null, X $>$ -169 mm
2. photopeak intensity decreases, partial collection tail appears , -169 $<$ X $<$ -171.2 mm
3. both photopeak and partial collection tail intensities are null, X $<$ -171.2 mm

Regions 1 and 3 are well explained: in the first case, each ^{241}Am γ-ray is fully detected in the segment leading to full photopeak efficiency while in the second case, there is no γ-ray to detect because the beam spot is outside the segment. The line around 50 keV in region 1 corresponds to few Compton back-scattering events where the secondary γ-ray escapes the detector.

Region 2 is more complex. The behavior of segment A1 in fig. 4.16(a) is explained as follows:

- Starting from X = -169 mm, the spot begins to cover the inter-electrode. The partial collection tail begins to increase at high energies (50-55 keV).
- As the spot position is incremented, i.e. as the spot illuminates deeper in the inter-electrode, the photopeak area decreases, the partial collection tail is more pronounced and extends at lower energies.
- At X = -169.6 mm the spot covers the full inter-electrode width, energies comprised between 0 and 60 keV are measured.
- At X = -170.6, the spot begins to illuminate only partially the inter-electrode. The contribution of partial collection tail at high energies disappears. There are no more full energy events because the spot does not cover segment A1 anymore.
- At X = -171.2, the spot is outside the inter-electrode.

Segment F1 pattern shown in fig. 4.16(b) is symmetric to the one of segment A1 which means that it behaves exactly in a mirror-like way as for segment A1.

Figure 4.16(c) presents a similar plot as panels (a) and (b) for add-backed energies of segments A1 and F1. However, no partial charge collection tail is visible. All counts in tails of panels (a) and (b) are gathered in the second peak seen at 57 keV in the -171 < X < -169.2 domain. Simultaneously, the photopeak intensity is reduced in the same X range as expected.

The above mentioned data indicate that, when the hole cloud reaches the inter-electrode, the energy which is measured by the neighboring electrodes is directly related to the location X of this charge between the electrodes. This can be only interpreted considering the second scenario, where charges are not drifting significantly through the inter-electrode surface within the energy integration time. Readout energies do not result in a real charge collection, but are entirely driven by Shockley-Ramo theorem application.

A remaining question is to know what is the becoming of these holes at the inter-electrode gap. In the case of ^{241}Am measurements, the 60 keV count rate is about 100 ct/s, i.e. one event every 10 ms. Jordanov trapezoid parameters are set such that the energy is readout 10 μs after triggering. There is plenty of time for trapped charges to recombine with thermal carriers or to disappear with leakage current between two γ-ray interactions. They might also drift at the surface with reduced velocity, such that they are immobile in the time scale of the energy readout.

4.6.5 γ-beam spot profile reconstruction

Any cut in energy in fig. 4.16 (a) and (b) can actually provide the γ-ray spot profile. As a first reasonable assumption, we can consider cuts of 3 keV width in the 10 to 48 keV range. This corresponds to 50 μm width spatial cuts, i.e. the pitch of the scan. Thirteen profiles shifted in X are obtained, they are all centered in the same origin and incremented in a unique profile shown in fig. 4.17.

The experimental reconstructed profile is compared to a similar projection of simulated data (see section 3.3). There is only a slight difference of the profile shape. The 1.7 mm full width at tenth maximum is identical for top-collimator to crystal front face distance of 20-30 mm, in agreement with the experimental conditions ($\sim$ 25 mm).

4.6.6 Experimental inter-electrode weighting potential determination

Based on the hypothesis that charges reaching the inter-electrode are immobile within the energy readout integration time, the amount of energy measured by each electrode as a function of the location on the inter-electrode gap can be considered as a direct measurement of the weighing potential of each electrode.

Figures 4.16 (a) and (b) are analyzed in order to extract the mean hole-cloud position as a function of the energy collected. The mean position is computed for each constant-energy vertical slice by bins of 0.33 keV over the range X $\in [-171.2, -169.0]$. Results are shown in fig 4.18. At low energy (E < 10 keV), variations are due to the noise of the measurement while for near-photopeak energy (E$\sim$50 keV), Compton edge counts are increasing the average position towards the considered segment. In the intermediate energy range, there is an almost linear variation of the position as a function of the energy. A1 and F1 weighting potentials straight lines are crossing nearby 28 keV, the weighing potential sum for a ^{241}Am event at this location is then 56 keV, leading to a 3.5 keV energy deficit to reach the expected 59.5 keV

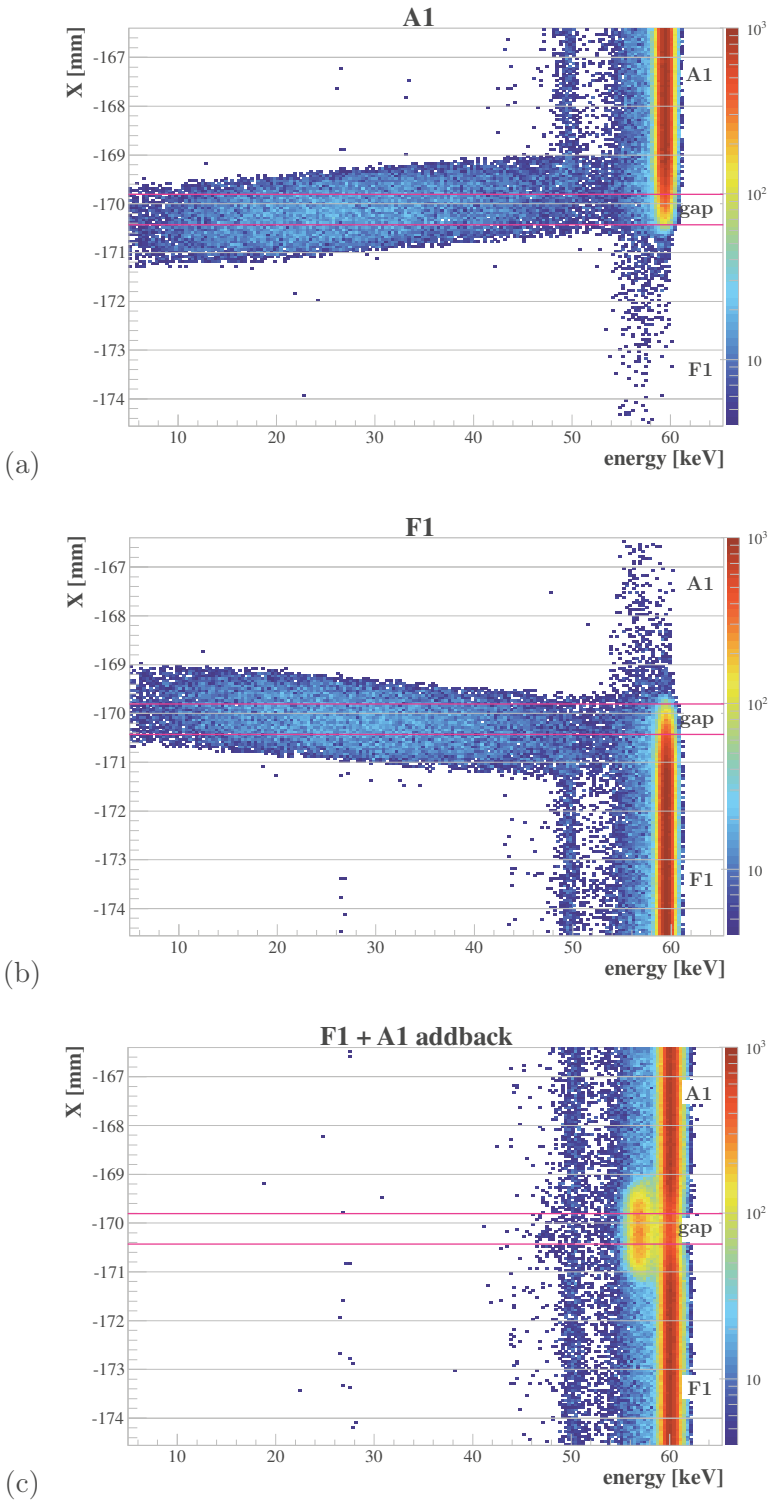

Figure 4.16: ^{241}Am spectra of segment A1 (a), F1 (b) and A1+F1 in add-back mode (c), along the scanning line crossing the inter-electrode. The two magenta lines show the inter-electrode limits between segments A1 and F1.

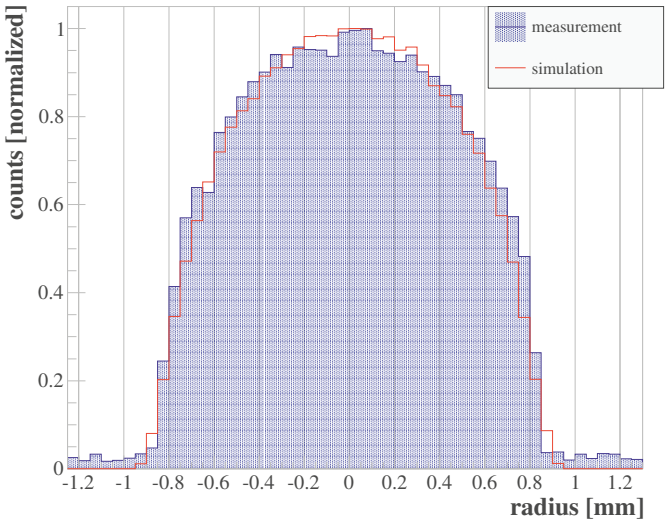

Figure 4.17: Reconstructed γ-ray spot 1D profile (filled blue) along X corresponding to the sum of 3 keV vertical cuts of fig. 4.16(a,b). Simulated ^{241}Am spot 1D profile (red line) at 28 mm from the top of the collimator.

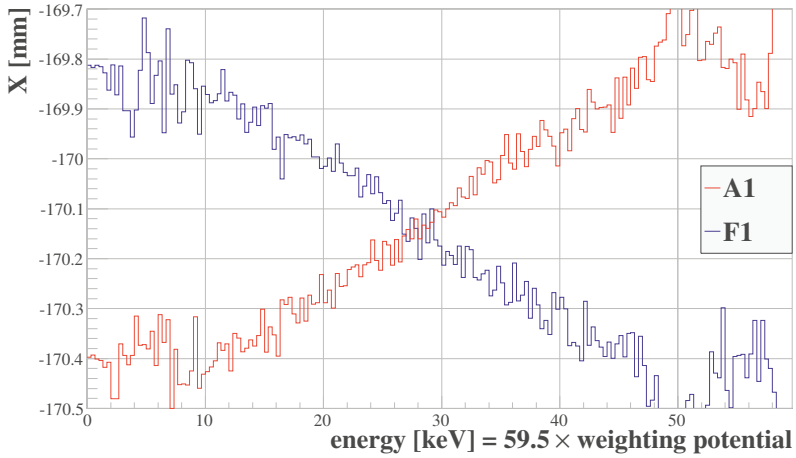

Figure 4.18: Position in the inter-electrode gap (Y-axis) as a function of measured weighting potential (X-axis) of segments A1 (red line) and F1 (blue line).

line. Because both weighting-potentials are linear and symmetric, their sum will be about 57 keV all along the inter-electrode gap, which explains the double photopeak in fig. 4.15.

The fact that the measured inter-electrode width (640 μm) is larger than the physical separation (500 μm) could be attributed to transition effects between the p+ electrode and the inter-electrode passivated surface. Recent studies [66] demonstrated that energy losses for charges collected at the inter-electrodes can be adapted in trade-off with other parameters in the semiconductor layer by treatment processes. In other words, it is possible to control the electric field distribution underneath the inter-electrode area.

4.6.7 High-precision interaction location - low energy imaging

The inter-electrode region shows outstanding position sensitivity due to charge sharing. The energy accuracy is given by the FWHM of the photopeak which is about 1 keV at 60 keV. In first approximation, the partial energy measured in neighboring segments, A1 and F1 in our example, corresponds to a measurement of the X location of the hole cloud in the inter-electrode. For an average gap width of 640 μm, a position accuracy of $\sim$11 μm is deduced. Figure 4.18 shows however that there is almost no spatial sensitivity for partial energy below 10 keV and above 48 keV. X varies about 650 μm over 40 keV leading to an effective sensitivity of $\sim$16 μm/keV.

Since a 1D hit determination is possible between two segments, it should also be possible to have direct 2D hit determination if the inter-electrode area is surrounded by at least 3 segments. This is the case in the front face of the crystal location, were 6 inter-electrode lines cross themselves in one point. A ^{241}Am scan, by steps of 200 μm pitch, partially covering this area has been used to test a new imaging capability. Results are shown in fig. 4.19.

Holes blocked in the 6 inter-electrode lines crossing point are detected by 6 neighbor segments each placed, nearly 60° to each other (asymmetric crystal). The interaction location is related to the energetic barycenter of the 6 segments, given by :

$$(\mathrm{X},\mathrm{Y})_{\mathrm{interaction}} = \frac{1}{\mathrm{E}_{\mathrm{total}}} \cdot \sum_{\mathrm{seg}=1}^{\mathrm{seg}=6} \mathrm{E}_{\mathrm{seg}} \cdot (\mathrm{X},\mathrm{Y})_{\mathrm{seg}} \tag{4.2}$$

where $(\mathrm{X},\mathrm{Y})_{\mathrm{interaction}}$ are the coordinates of the reconstructed hole surface collection location, $(\mathrm{X},\mathrm{Y})_{\mathrm{seg}}$ are the coordinates of the edges of the central corners of the 6 segments, $\mathrm{E}_{\mathrm{total}}$ is the summed 6-segments energy and $\mathrm{E}_{\mathrm{seg}}$ is the individual segment energy. The active area for 2D surface hole collection localization is tiny. It has an hexagonal shape with 640 μm length per side (the thickness of the inter-electrode). This represents approximately 0.7 mm^2 in surface.

The 9 panels in fig. 4.19 represent a sequence of the γ-ray spot traveling from segments E1 to B1 through F1, A1 and the corresponding inter-electrode regions. They are explained one by one, a minimap indicates in each sequence the relative position of the γ spot compared to the front face of the crystal:

(a) : the beam spot is fully on segment E1, counts are gathered in one single point corresponding to E1 position

(b) : the beam spot is still on segment E1, but it covers also partly E1/F1 interface. E1 and F1 are reading each an energy but not the other segments, therefore the interaction location draw an arc between E1 and F1 segment position (only 1D localization information).

(c) : the beam spot is mostly on E1, it covers fully E1/F1 inter-electrode, also partially F1; it begins to be detected in the 2D area.

(d) : same as (c) but the beam spot covers a large part of the 2D area. Within the 2D area, all segments readout a non-negligible energy value which pulls the event barycenter deeper in the 2D area. These events give an estimation of the γ-beam spot 2D profile.

(e) : the beam spot does not cover E1 anymore, it illuminates F1, A1, the F1/A1 inter-electrode and half of the 2D area

(f) : the beam spot does not cover F1 anymore, it illuminates A1, B1, A1/B1 inter-electrode and still the 2D area

(g,h,i) : reverse effect of (a,b,c) with the beam spot moving away from the 2D active area towards B1 segment.

The issue with this measurement is that the inter-electrode area is so sensitive to the location that the spot is too wide to enable precise and further studies.

Technical development involving semiconductor detectors which detection surface is mainly covered by crossing segmentation lines surrounding tiny active pixels could lead to new fine imaging applications (while keeping high energy resolution).

4.6.8 Inter-electrode energy-split effect in the detector bulk

Inter-electrodes are localized on the external surface of the crystal. However, holes generated in the bulk (for higher γ-ray energies) might also be affected by this inter-electrode region. Since these events lead to significant energy deficits, any interaction undergoing this effect do not lead to full-energy detection. This effect has a larger occurrence probability in the case of multiple Compton scattering with several hit segments, as it is sufficient that only one interaction leads to a charge sharing to get an energy deficit in the sum energy.

As inter-electrode events are easy to detect, it is possible to use scanning data in order to draw a map of the detector regions affected by incomplete energy readout. The vertical 1 mm-pitch ^{137}Cs scan is analyzed in the following conditions :

- 2-fold events are requested,
- direct neighboring segments are hit,
- summed energy is more than 5 keV inferior to the Core energy (such large shift is too large to be due only to segment/segment crosstalk).

The two first criteria are mandatory for inter-electrode event selection and the third allows to reject most of classical Compton scattering. These conditions are selecting single-interaction events leading to charge sharing between two neighboring segments, but also Compton scattering events with one interaction localized on a region leading to inter-electrode events, and the other interaction in one of the two adjacent segments.

The analysis was performed for each event in the 150 keV to 700 keV range, the amount of inter-electrode events which were observed is 3.5% of both 1-fold and 2-fold events, and 8.2% considering 2-fold events only.

The inter-electrode energy deficit map is shown in fig. 4.20. It represents the number of events where holes are collected on longitudinal inter-electrodes (the gap between sections, i.e. vertical segmentation) as a function of the γ-ray spot position for the ^{137}Cs scan. Indeed, the segment boundaries are clearly visible and lead to significant crystal volume. Concerning PSA in AGATA, the localization of such event is straightforward and accurate: the azimuthal angle is given precisely by the segmentation line position and the location along the radius is given by the net-charge signal shape.

This emphasizes the fact that inter-electrode energy loss may concern any γ-ray whatever its energy or angle of incidence. A direct consequence is that surface segmentation of n-type detectors leads to photopeak losses on summed-segments and to tailing on the Core if these events are not taken into account and/or corrected.

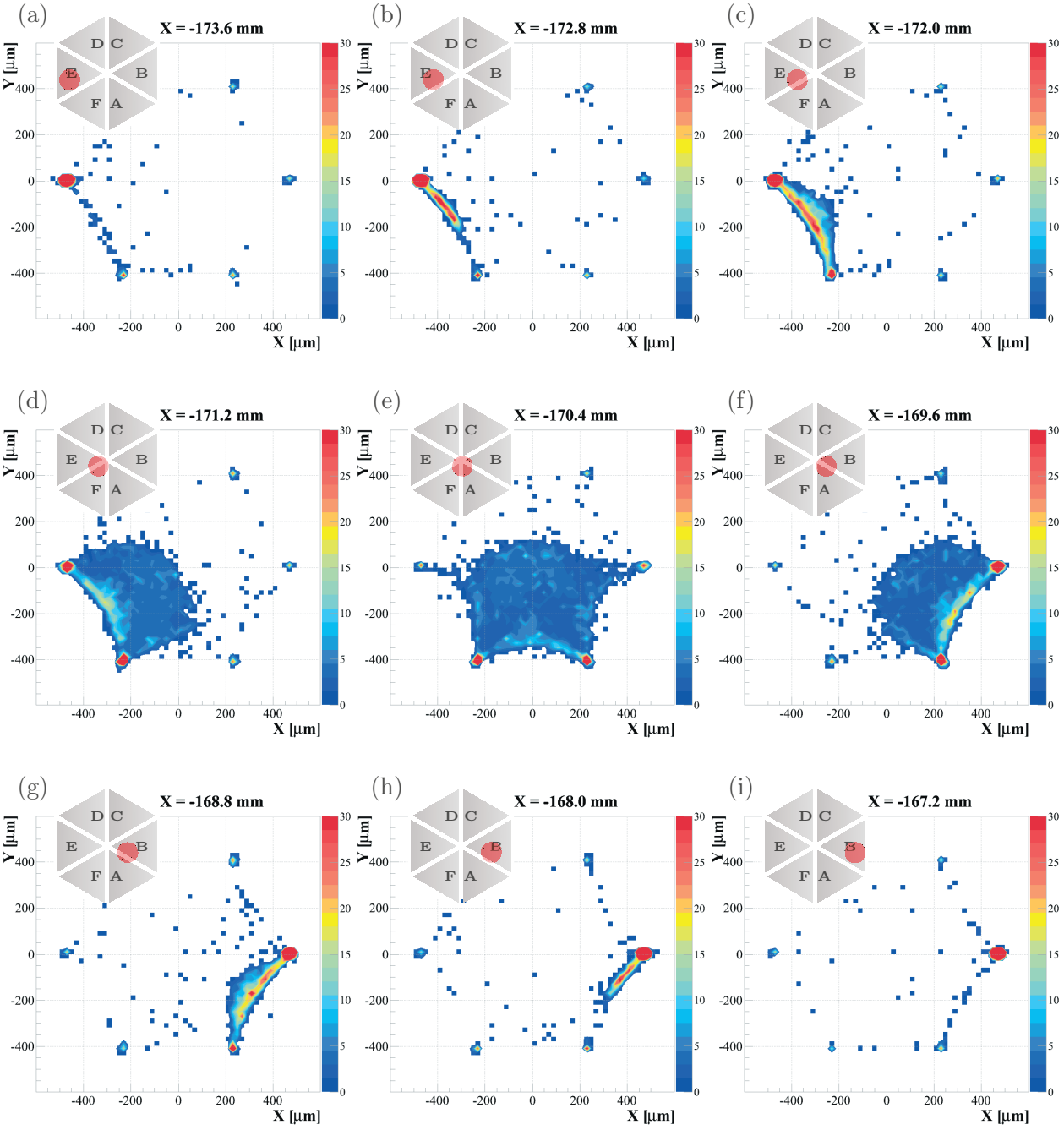

Figure 4.19: Imaging ability in the crystal front-face, center crossing point of inter-electrode lines. (a) spot fully in segment E, (b) spot partially covering inter-electrode E/F, (c) spot fully covering inter-electrode E/F, (d,e,f) half spot gradually covering the 2D sensitive central inter-electrode, (g) spot fully covering inter-electrode A/B, (h) spot partially covering inter-electrode A/B, (i) spot fully in segment B. For more details see text.

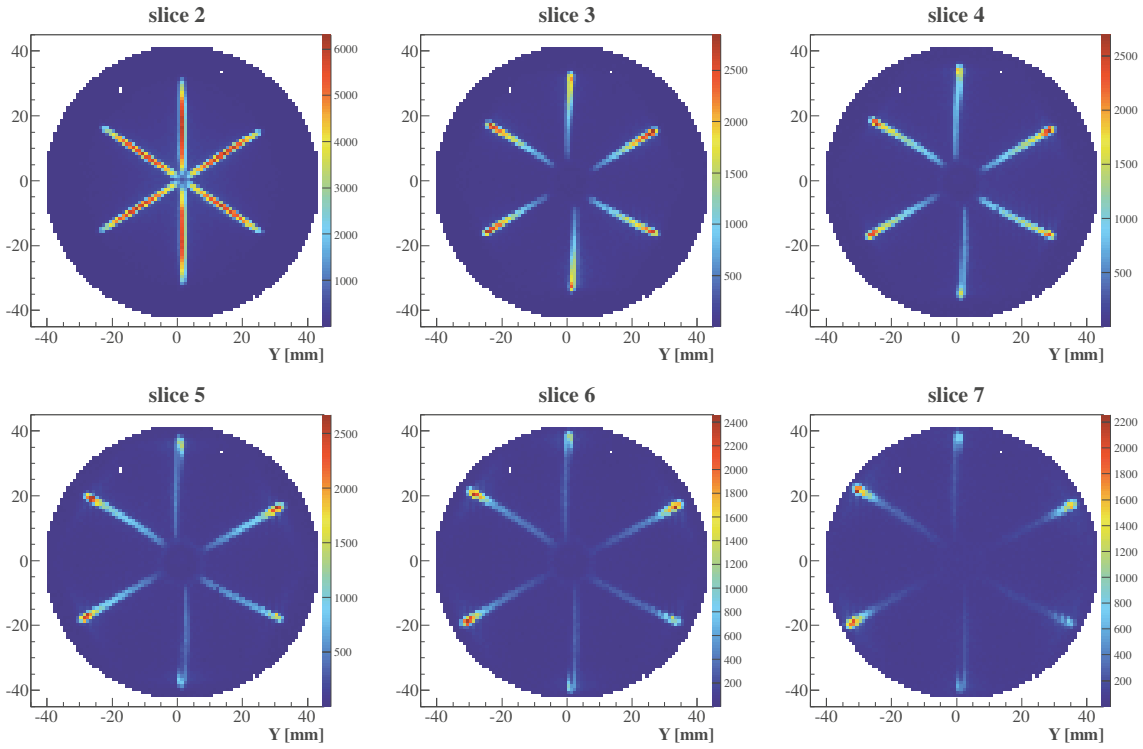

Figure 4.20: ^{137}Cs scan: distribution of inter-electrode events occurring in the longitudinal segmentation lines as a function of the collimator position for AGATA slices.

For each segment longitudinal interface, the number of counts affected by charge sharing increases as the interaction is closer to the external surface. Consequently, the probability for an interaction to conduce to hole inter-electrode collection is lower if the hole drift distance/time is longer. This can be understood as follows: at low radius, a small variation of the interaction location results in a large variation of the hole collection location. The region affected by surface charge sharing has then a kind of triangular shape: very thin for small radii, and increasing until 500 μm large on the external surface.

An identical map can be drawn in order to visualize regions in the bulk which lead to inter-electrode events on the segmentation line separating slices. This one is not shown here due to the rather complex behaviors on these maps.

4.6.9 Charge sharing summary

As shown in the previous subsections, the inter-electrode hole collection presents complex effects. To summarize, here are the features observed from low count-rate measurements on AGATA B006 crystal:

- the electrical field distribution allows hole clouds to drift towards the inter-segmentation line,
- a hole cloud reaching the inter-electrode is not collected. During the time for energy integration, it is blocked at the surface and does not drift anymore,
- the energy is split between two adjacent electrodes, the energy partition depends quasi-linearly with the relative location of the hole cloud on the inter-electrode gap,
- full energy readout is not reached probably because charges are blocked in a region where the weighting potential is not full, for the same reasons there is a slight deficit in the Core readout energy,
- there is no experimental indication on the baseline allowing to guess what happens to blocked charges, there is no effect of charge stacking for low-energy measurement and low count rates (this work).

Once these events are pointed out, they can be corrected (the fraction of energy deficit is virtually added back) so that the full-energy efficiency is retrieved. This process allows an outstanding position sensitivity for X-rays and low-energy γ-rays with a simple pulse-height readout. New applications could result such as very high resolution imaging or online low-energy beam profile monitoring.

4.7 Bored hole investigation

Precise scans along the bored hole were performed for crystal alignment purposes. They revealed several issues about the detector such as charge collection defects in the front of the crystal, and a large effective bored-hole diameter. It has to be noticed that the first event filter is the digital trigger system. This one is based on a simple first difference stage [58], i.e. a derivative of the signal. It is not set to detect possible negative signals on the Core, and it might fail to trigger on signals with abnormally long risetime (> 1 μs). The discussion in

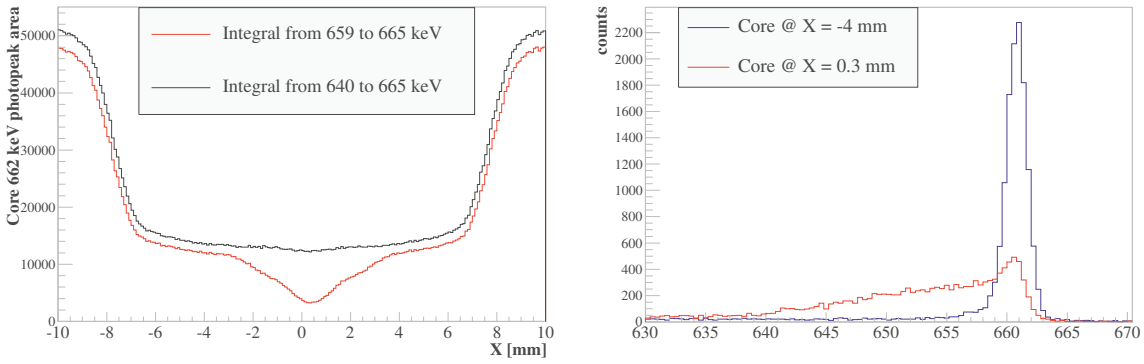

(a) (b)

Figure 4.21: (a): Core photopeak area along the X axis for a thin (red line) and large (black line) energy range of integration.(b): Core normal spectrum (blue line) and degraded spectrum (red line) with charge-collection issues. The latter spectrum corresponds to the ^{137}Cs beam pointing at the location where the 6 segmentation lines intersect on the front of the crystal, the beam only crosses the first slice.

this section focuses on events with shapes and risetimes typical of a coaxial HPGe detector in standard conditions for which the digital trigger is well suited.

4.7.1 Front crystal charge collection issues

The front part of the detector, ahead the bored hole, undergoes misleading effects which change the Core photopeak shape. Core photopeak area along the X-axis is plotted in fig. 4.21(a). The red line is the figure obtained with a typical energy range of integration of 662 $\pm$ 3 keV. The negative bump around X = 0, over a 5 mm wide area, is due to a lack of photopeak counts which is unexpected here. Indeed, it arises in the area of the crystal where the electric field is the most intense, due to the proximity of positive and negative electrodes. Charge collection should therefore be optimal. If the photopeak area integration range is raised to the 640-665 keV range, counts are retrieved (black line). The offset between both figures is due to the superposition of radioactive background while integrating in a wider energy range. Figure 4.21(b) shows an example of spectra coming from both normal and abnormal regions. In the worst case, events corresponding to full-energy deposits are spread over $\sim$20 keV below the expected photopeak energy. This behavior corresponds to charge collection defects: the digital energy readout occurs when some charge carriers are still drifting, leading to energy losses.

The negative bump in fig. 4.21(a) is not centered on X = 0 but slightly shifted. This is in agreement with the crossing point position of the front face segmentation lines which is shifted in the same way (see fig. 4.2(a)). In this specific area, few millimeter square of the crystal surface gather six different segment electrode edges and a relatively large proportion of inter-segmentation line. Core charge-collection defects at the center of the first crystal slice is then a side effect of the external segmentation. One possible explanation is charge sharing, as explained in section 4.6.8.

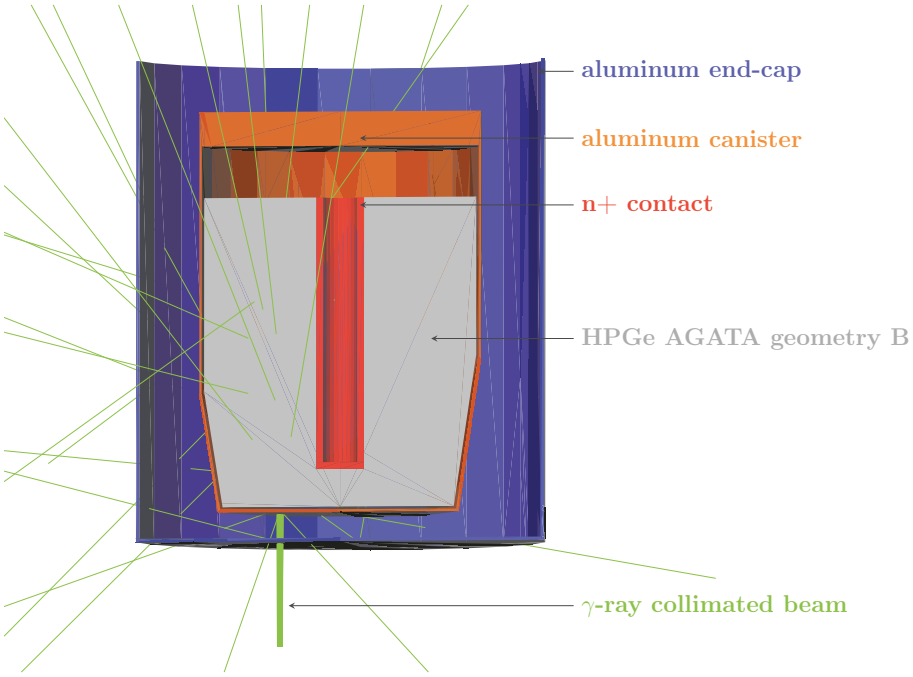

Figure 4.22: 3D cut view of Geant4 geometry used for bored-hole investigations.

4.7.2 Geant4 simulation

A Geant4 simulation has been set up specifically to investigate γ-ray scanning along the n+ contact, i.e. the bored hole. It is based on an AGATA HPGe crystal of geometry B, encapsulated within a 0.8 mm thick aluminum canister. The capsule is surrounded by a 1 mm-thick aluminum end-cap. A bored-hole of 10 mm diameter is placed in the crystal center, from the rear side down to 13 mm to the front side. A Ge dead layer surrounds the hole to simulate the Li-diffused contact, with a thickness that can be varied. The geometry is shown in fig. 4.22, a half cut to distinguish each element. The pencil beam is based on mono-energetic 661.7 keV γ-rays. The collimated γ-ray beam is simulated as follows: the γ-rays originate randomly from a disc of 2 mm diameter, which is representative of the spot diameter in the middle of the crystlal. This source is placed at 4 cm from the front of the crystal. The γ-rays are oriented towards the detector along the Z-axis, with a random shift in the 0° to 0.5° range. Several runs with 100 000 γ-rays emitted from various X positions are performed in order to simulate the detector scanning. The scanning pitch is 0.1 mm between two points and the collimator translation is performed along the crystal diameter. The X=0 value corresponds to the center of the crystal.

In order to perform realistic simulations, Geant4 data are uncalibrated from energy to ADC channels, following experimental calibration. This enables to apply exactly the same analysis procedure to both simulated and experimental data. At the end of this pre-sorting step, both experimental and simulated spectra have the same binning.

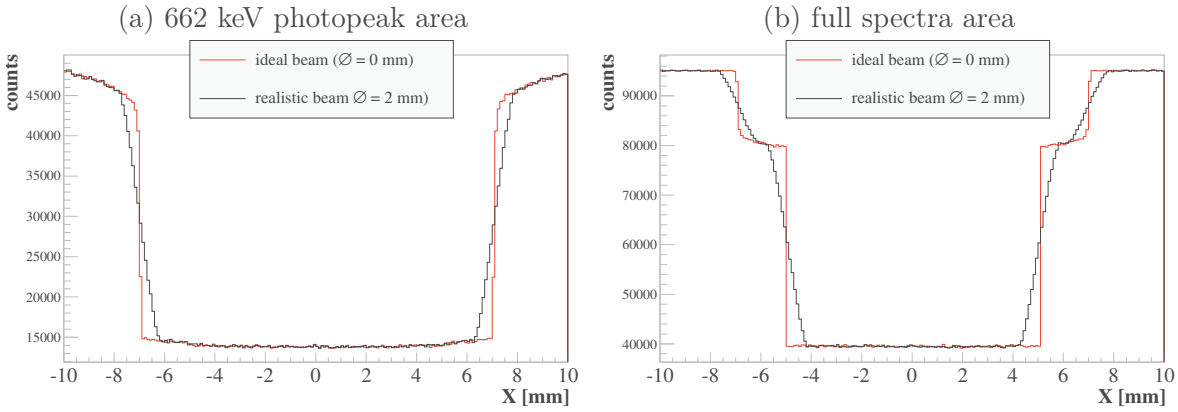

Figure 4.23: Geant4 simulations: area of 662 keV Core photopeak (a) and Core full spectra area (b) along the X-axis for scans with an ideal spot (red line) and a realistic spot (black line).

4.7.3 Effect of the beam spot diameter

The beam spot diameter influences the final response as already mentioned in section 3.4.4. If odd effects are localized within an area with a characteristic length inferior than to spot size, these effects are averaged. Two simulated scans are compared, one with a standard pencil beam, the other one with an ideal beam (0 mm diameter and γ-rays are oriented exactly along the Z-axis of the detector). The scan with the ideal pencil beam gives the response of the detector with an exact location. The pencil-beam response is a convolution of the ideal response, integrated over the pencil-beam area. This averaging effect is shown in fig. 4.23. A 2 mm dead-layer thickness has been chosen to account for the n+ contact surrounding the bored hole. The full energy was requested in the Core, no conditions were set on the segments.

The photopeak area with the ideal beam is plotted in red color on panel (a). It shows the following standard behavior:

- a constant low counts in the range -7 mm to 7 mm which corresponds to γ-rays undergoing their first interaction in the first slice of the detector. The lack of counts is due to the void within the bored hole,
- left and right large counts ($|X| > 7.5$ mm) correspond to γ-rays interacting in all the detector volume. The top plateau is not flat because of Compton scattering,
- the sharpness of the beam allows to separate both regions with a sharp drop in the photopeak area (around $|X| = 7$ mm).

The same figure is plotted in black color using a realistic beam. It is a smoothed copy of the previous plot. Drops at $|X| = 7$ mm are no more frank and their width correspond to the one of the pencil beam. As explained in section 3.4.4, the effective volume boundary is measured on the abscissa at half height (or half counts) of the quasi-linear drop due to pencil beam penetration. Care has to be taken to the transition between the part of the slope driven by the pencil beam penetration and the part driven by Compton scattering. Red and black lines cross at 30 000 counts, half way between 15 000 counts (the bottom) and 45 000 counts

(maximum in the hole), exactly at |X| = 7mm.

A similar analysis is performed with the full histogram area (no energy condition), results are plotted in fig. 4.23(b). The same distinction as explained previously appears when the spot points towards the bored hole or the germanium bulk. An additional structure appears however, which marks the n+ layer boundaries between 5 and 7 mm radii in accordance with simulation parameters. It is due to undetected Compton interactions occurring in the n+ dead layer, which scattered low-energy photon is detected in the active Ge volume. The real beam simulation has a smoothing effect but boundaries determination are still feasible. If the dead layer thickness is thinner than the beam diameter, the transition location between the dead layer and the active volume is not straightforward. However, if statistics is large enough, two slopes are visible in the real beam conditions, the steepest crossing the red curve at 62000 counts for |X| = 5 mm which gives the size of the bored hole and the slightest crossing the red curve at 87000 counts for |X| = 7 mm which gives the external limit of the Li-diffused, n+ contact.

4.7.4 N+ layer thickness adjustment

Several simulation iterations were performed to reproduce the full area of the Core spectrum as a function of the pencil-beam position. The n+ dead-layer thickness is the adjustment parameter. Note that simulated spectra are corrected by a systematic offset which takes into account experimental radioactive background. Simulation results are in fair agreement with experimental data considering a 2.5 mm thick n+ dead layer as shown in fig. 4.24. Left and right decreasing and increasing slopes agreed well with each other. The change in slope observed at X = -6.5 mm and X = 6.5 mm, is still smoother on the experimental plot because 1) the transition between the dead layer and the active volume is not as abrupt as simulated, 2) as the Core is investigated, results are integrated over the whole length of the bored hole. A simulated 2.5 mm-thick n+ layer reproduces quite accurately the experimental behavior. However, diameter measurement on slices give a hole diameter closer to 14-14.5 mm.

Particular features (bumps) emerge from the low-count plateau in the bored hole in experimental data. They are assigned to the detection of scattered γ-rays after Compton scattering localized on inert material in or near the bored hole.

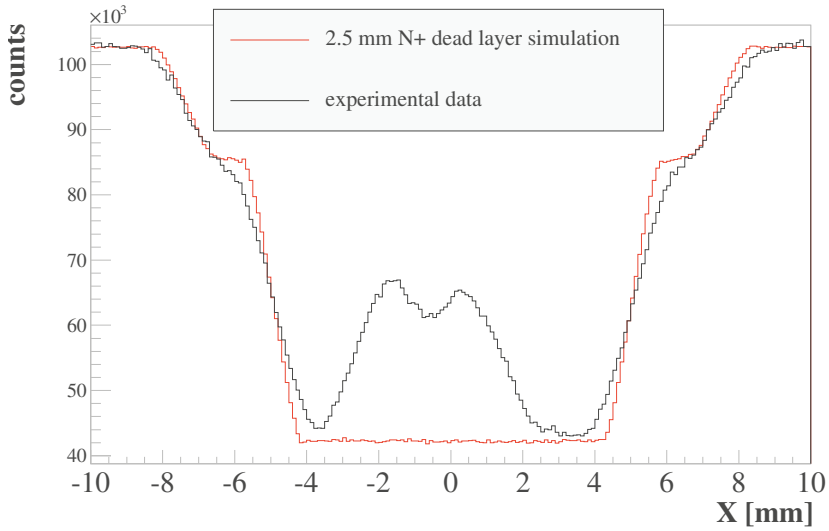

Figure 4.24: Core full spectrum area as a function of the X position for simulated (red line) and experimental data (black line).

Chapter 5

Pulse Shape Comparison Scan of B006

5.1 Pulse Shape Comparison Scan Experiment

5.1.1 Optimization of the computation time for χ^2 offline analysis

Pulse shape comparison scan is based on serial comparisons between pulse shapes in order to determine if they are similar or not. A widely used technique to do such work is the χ^2 test. In the present case, a list A of supertraces measured at one collimator position for a given Ge crystal orientation is compared to a list B of supertraces measured at another collimator position for another Ge crystal orientation. The supertraces are composed of the 120-sample pulse shapes of the 37 channels of the multi-segmented crystal. The χ^2 test is expressed as follows:

$$\chi^2 = \frac{\sum_{ch=0}^{36} \sum_{i=1}^{120} (A_{ch}(i) - B_{ch}(i))^2}{\sigma^2 \cdot N} \tag{5.1}$$

where $A_{ch}(i)$ and $B_{ch}(i)$ are the samples of channel ch at time t (t = i×10 ns), σ is the amplitude of the noise during the measurement and N is the total number of samples compared (37×120). At the end of the test, the χ^2 value is small if both supertraces are similar and may be very large is they are very different. Each pulse shape combination between lists A and B are tested this way.

Two strictly identical supertraces should have a null χ^2 value, but experimental signals suffer from noise which tends to raise the χ^2 value. The σ parameter in eq. 5.1 allows to normalize the χ^2 such that the minimal value should be 1.

The amount of data to test for a complete PSCS analysis is evaluated with following considerations :

- each supertrace corresponds to 4440 time samples,
- each scanning position contains about 15 000 relevant supertraces,
- each supertrace of one scanning position is compared to each supertrace of another crossing scanning position, which is 15000×15000 comparisons,
- about 48500 experimental crossing points are scanned in one AGATA crystal volume.

The number of samples to be compared for a full detector scan is $\sim 5 \cdot 10^{16}$. Considering that each sample has a 2 bytes length, the whole χ^2 test would correspond to the process of 100 petabyte of data. Even with a very fast processor, the readout of data in hard drives would restrain the analysis speed. Assuming that the χ^2 test for each experimental point requires 5 min of data analysis, the whole PSCS analysis would take ∼170 days. Some tricks have to be used in order to get the result in a reasonable time.

Hit segment check: each segment which is physically on the γ-ray beam path can undergo an interaction. Thus each distribution contains events with several segment hits. The first natural criterion for comparing two supertraces is to check that the same segment is hit. Many supertraces are rejected before any χ^2 evaluation with this condition.

χ^2 test simplification: in practice, the noise is not evaluated within each pulse shape, a global noise equivalent to $6\sigma = 10$ keV is considered for each pulse shape of each channel. Such a noise is larger than the experimental one. As a consequence, typical χ^2 values which are given further are below 1. The number of sampled data is also constant for each traces, so that eq. 5.1 can be written as:

$$\chi^2 \times \sigma^2 \times N = \sum_{ch=0}^{36} \sum_{i=1}^{120} (A_{ch}(i) - B_{ch}(i))^2 \tag{5.2}$$

This reduces the number of software operations to perform for the offline test, by avoiding a division in the χ^2 test cycle. In addition, only the lowest χ^2 values are of interest, and an ongoing χ^2 evaluation can only increase. The comparison is stopped if the incremented ongoing χ^2 value is higher than a maximal threshold value before the end of the χ^2 test. Using these two conditions, the test is significantly faster.

Supertrace optimization: the comparison is performed with selected one-fold events. Only few channels contain localization information for such events: there is a net charge signal in the Core and in the hit segment, relevant transient signals in the nearest neighbor segments, small transient signals in the secondary neighbors and only tiny capacitive-induced signals for the other channels. Each channel contributes to the global information of a supertrace, as a function of its maximum amplitude. So, near-interaction channels contribute significantly to the signal information whereas the other channels contribute mostly to the noise. In order to avoid useless comparisons, only 6 channels are used for the χ^2 test: the Core, the hit segment and the 4 nearest neighbor segments, thus improving the global signal-to-noise ratio of the reduced supertrace, which is called trace. With the above-mentioned procedure, 85% of the samples are neglected.

Signal over noise optimization: similar considerations apply to each sample. Relevant information for a χ^2 comparison is restrained to samples corresponding to the signal risetime which is typically ∼500 ns long, or 50 samples. However, 120 samples are digitized for the offline normalization of pulse shapes (see sub-section 3.4.3). The first part of pulses corresponds to the signal baseline noise and the last part to the slow exponential preamplifier decay. Thus the χ^2 test only needs to run over the samples where the signal is changing due to charge collection. In this case, about 60% of the samples are not considered.

Sliding χ^2 threshold: as explained above, a χ^2 threshold is set in order to stop the comparison for obvious diverging traces. It has to be low enough to be useful, and high

enough to perform the test, even in hard conditions (low statistics for example). A problem arises considering the variety of pulses shapes within the crystal: they can be fast or slow and transient charges can have significant amplitudes or not, depending on the local position sensitivity of the detector. As a result, a χ^2 comparison between similar shapes in different locations lead to various χ^2 values. The threshold must be adapted to the local expected type of shape. This is done using a sliding threshold. At the beginning of the comparison of two sets of data, the χ^2 threshold is set high. As χ^2 tests are performed between traces, the N_{good} best χ^2 values are kept. The largest of these N_{good} values is considered as the χ^2 threshold. As the χ^2 comparison proceeds, new low χ^2 values are obtained, leading to decrease the χ^2 threshold. Typically, 200 χ^2 tests are kept, corresponding to 400 traces which will contribute to the final experimental pulse-shape determination. With such an algorithm, only about 2000 tests among 15000^2 are performed for each point.

By applying the above-mentioned selections, the offline-analysis time required to extract 48500 experimental points is reduced to 5 days. It can even be faster with several analyzing codes running simultaneously.

5.1.2 Mean pulse-shape refinement

The χ^2 test which was described above is very efficient to select pairs of similar pulse shapes. However, it does not ensure that selected pairs are similar with each others. In the case of natural radioactive background, or even multiple Compton-scattered γ-ray, an interaction can happen anywhere in the crystal. While comparing two pulse-shape distributions which are supposed to cross at a given point (X,Y,Z) in the detector, these kind of events might be accidentally selected and yet their pulse shape can be very different from the expected one. If such false pulses are used to calculate the experimental mean pulse shape for position (X,Y,Z), the resulting pulse may be affected.

An iterative automatic process has been developed in order to clean the selected pulse-shape distribution from these fake events. At the end of the χ^2 test, some pulse shapes are selected and are averaged. Each one is compared to the average with a χ^2 test. Those which have the worst χ^2 values are rejected from the group of valid pulses. This process proceeds several times as shown in fig. 5.1. Typically, 10 iterations are used, each time rejecting $\sim$5% of the pulse shapes. At the end, 40% of the pulse shapes farthest from the average are rejected.

There is also a possibility that the χ^2-selected pulse shapes come from various segments. This is particularly the case when the crossing voxel is near an effective 3D segmentation boundary. In this case, the mean pulse shape is averaged with pulse shapes of the segment which has been the most hit.

5.2 Pulse Shape Comparison Scan simulation

Although it has been demonstrated that the PSCS technique works well within AGATA detectors (see [35]), some uncertainties remain. A major one is the issue of the Compton effect which is predominant at 662 keV in Ge. Any measured full-energy 662 keV event has a large probability to be the result of multiple Compton interactions. The location information given by the collimator position is then not reliable anymore and the experimental mean pulse shape could be wrong. Also, several choices for the χ^2 test optimization could affect the

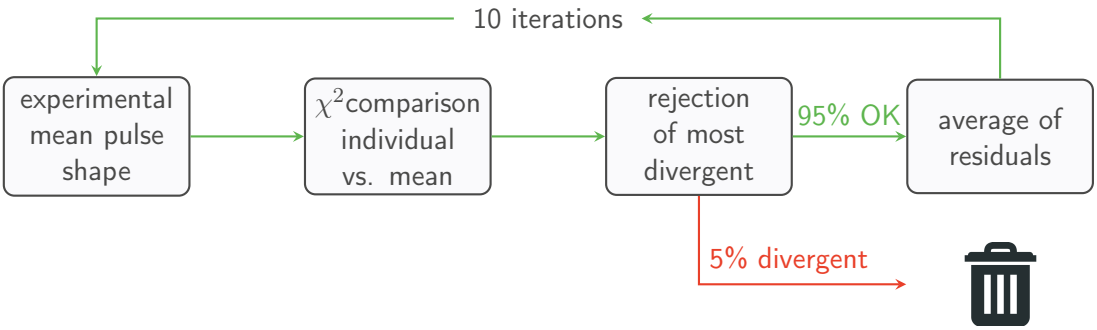

Figure 5.1: Principle of the mean pulse shape refinement.

results and need to be benchmarked, such as: reduction of relevant channels, fast χ^2 test with sliding threshold or the effect of the iterative mean pulse-shape refinement. These questions deserve simulation calculations for check and clarification.

5.2.1 Geometry and procedure

The PSCS simulation is composed of three steps :

1. Determination of collimated γ-ray interactions for a vertical and an horizontal scan with Geant4.

2. Generation of raw pulse shapes corresponding to simulated scans.

3. Electronic filtering of pulse shapes and determination of mean pulse shape with PSCS χ^2 algorithm.

At the end of this procedure, the mean pulse shape is based on several selected pulse shapes for which positions and energies of interactions are known. This allows to check if the mean pulse shape originates truly from the crossing point of the two vertical and horizontal scans. A way to determine the quality of the reconstructed mean pulse shape is to compute the energy release barycenter of all PSCS-selected pulse shapes. It is calculated by weighting each interaction point position by the corresponding energy deposit. The closer this barycenter from the crossing point, the better the mean pulse shape. In addition, the simulated mean pulse obtained by the PSCS technique is compared to the simulated pulse shape at the very crossing point in order to ensure that both are similar.

The detector geometry is the one described in chapter 2: a simplified coaxial slice close to the rear of an AGATA detector. As there is only one slice, no information along the Z-axis can be extracted and there are only two direct neighbor segments : those from the left and the right of the hit segment. Geant4 scan simulation uses mono-energetic 662 keV γ-rays emitted from a fake-collimator moving along a 2D grid. The γ-ray source is identical to the one described in section 4.7.2. A 1 mm thick aluminum end-cap surrounds the germanium crystal in order to take into account possible scatterings. No natural γ-ray background is considered in the simulation. The electron cut parameter was set high, such that their energy

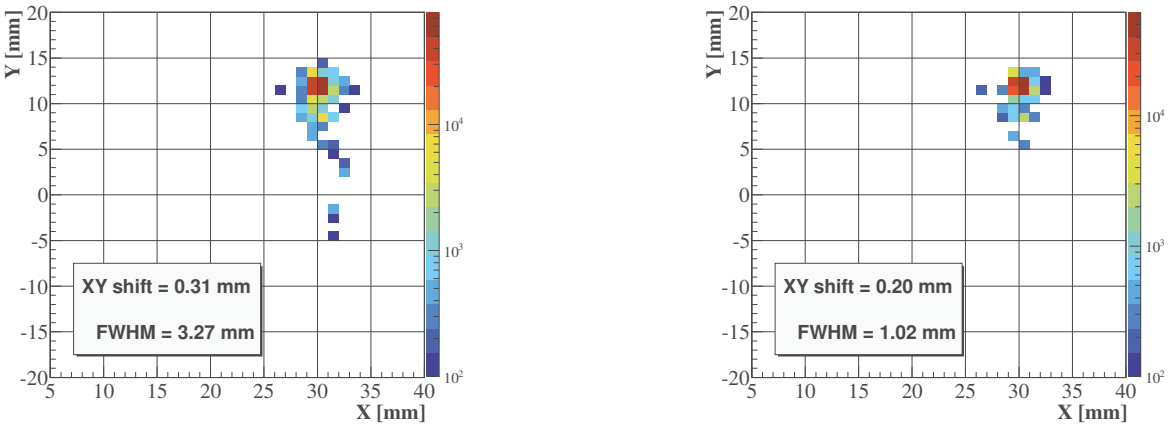

(a) (b)

Figure 5.2: Simulation of energy release distribution after PSCS selection for two collimated beams crossing at X=30 mm, Y=12 mm in the detector, before (a) and after (b) mean pulse-shape refinement. The bin size is 1×1 mm, the XY shift is the distance between the crossing point and the energy release barycenter, the FWHM is the one of the distribution around (XY).

is fully absorbed at their creation location, i.e. the electron ionization through their drift within HPGe is not considered. This allows to limit the amount of pulse shape to simulate in order to perform simulations in reasonable time. The simulated scan is performed on a XY plane, at a fixed Z position.

5.2.2 Results in standard conditions

As many points need to be checked, some relevant parameters are used in order to estimate the quality of the test. Due to the geometry of the simulated detector, there is only an estimation in the XY plane.

- **XY shift** is the distance between the exact crossing point of the two beams and the barycenter of selected γ-ray interactions in the XY plane,
- **FWHM** corresponds to the XY standard deviation of the selected interaction distribution, multiplied by factor 2.35,
- **singles percentage** is the proportion of pulse shapes corresponding to single-hit events among all selected pulse shapes, i.e photoelectric absorption interactions in the case of 662 keV events.

Typical energy distribution at the output of the PSCS algorithm are shown in fig. 5.2. The energy of 400 pulse shapes validated by the software are plotted in panel (a). Energy deposits corresponding to selected pulse shapes are focused on the crossing point but some come farther. The barycenter of this figure is well centered where expected (low XY shift) but pulse-shape variation is not linear with position. Therefore, pulses coming far from the crossing point do not necessarily cancel themselves and they are degrading the final PSCS

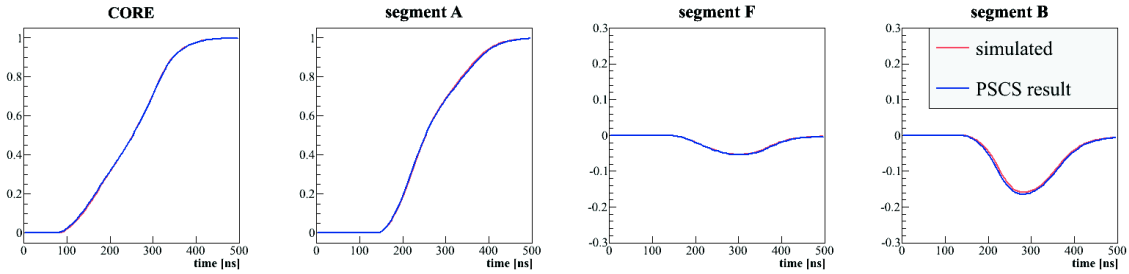

Figure 5.3: Simulated pulse shapes corresponding to the energy distribution of fig. 5.2(b) at X=30 mm, Y=12 mm after electronic filtering (red) and after PSCS mean pulse shape with simulated database (blue).

mean pulse shape.

The mean pulse-shape refinement procedure is performed with these results and allows to select pulses more focused on the spot, as shown in fig. 5.2(b). The XY shift of the barycenter is slightly improved by the procedure, but the energy-release spread is obviously more compact. The corresponding PSCS mean pulse shape in shown in fig. 5.3 along with the true simulated pulse shape at the exact crossing position. Both are almost identical demonstrating the effectiveness of the mean pulse-shape refinement technique. Some problems are identified at segment boundaries as seen in fig. 5.4. Almost all XY shifts are pointing towards the segment center but only those near segment interfaces have a relevant amplitude. It is noteworthy that XY shift results are homogeneous in the segment, which demonstrates that PSCS is efficient whether transient pulses have large amplitude or not. In fact, a null amplitude transient pulse is also a useful information: as only a limited region within segments have such properties, it contributes also to the positioning information. Two reasons explain the larger XY shift in the vicinity of the segment boundaries:

- the technique selects only hits in the segment of interest and, therefore, cannot consider energy deposits extending in another segment, which pulls the barycenter towards the hit-segment center,
- this region is very sensitive due to large variations of transient charge amplitude, so that the probability to identify similar pulses between two crossing distributions is lower in this region than towards the segment center.

In conclusion, PSCS mean pulses are very similar to simulated ones, except along segment interfaces, where the transient pulse of a direct neighbor is slightly under-estimated.

5.2.3 Various test conditions

Several test parameters (listed in table 5.1) are investigated in order to optimize the PSCS algorithm selection. Low values of XY shift and FWHM combined with a high percentage of single hit indicate an efficient test. Results of this analysis confirm that the standard PSCS conditions which were chosen are optimized :

- Refinement iteration obviously improves the result by rejecting some fake coincidences not coming from the expected point.

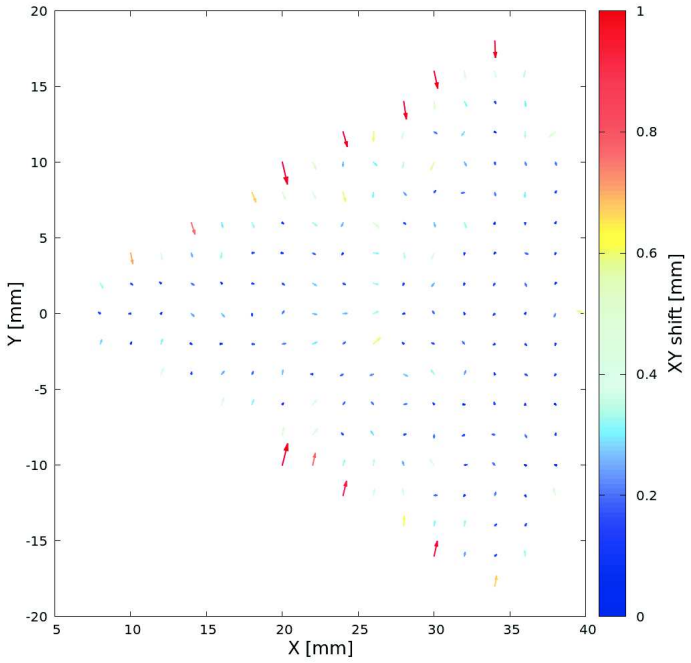

Figure 5.4: Arrow plot of the XY shift for each scanned point of segment B. Arrows start at the simulated beams crossing position and point towards the barycenter of the energy distribution selected by PSCS.

Run	XY shift [mm]	FWHM [mm]	Fraction of single events %	Details
1	0.33	2.9	43.7	standard PSCS conditions
2	0.34	3.1	42.3	no refinement iteration
3	0.37	3.2	42.4	all channels used
4	0.50	5.0	35.3	noise 20 keV
5	0.36	3.0	42.8	alignment on T10
6	0.38	3.5	39.8	low statistic (25%)
7	0.33	3.1	42.7	transient charges weighted by a factor 6
8	0.34	2.8	49.5	no net charge uses
9	1.00	7.0	27.7	shift test

Table 5.1: PSCS simulation results for various parameters. Values are averaged for each point scanned in segment B. Good values are obtained for standard parameters which are : alignment on T50, Gaussian random noise of 10 keV, only net charge deposits and direct neighbor channels used.

- Noise is a limitation factor : a high level of noise leads to inaccuracy in the χ^2 comparison and then to a poorer selection of similar pulse shapes.
- Comparison of transient pulses limited to direct neighbors is a good way to focus on signal evaluation and to reject random noise from the analysis.
- The higher the statistic in the compared series of pulse shapes, the better the selection. This evident result leads to optimize the acquisition time for each scanned point considering the generated data volume and the time for the analysis.

The shift test (run 9 in table 5.1) corresponds to a PSCS with vertical and horizontal beams shifted by 2 mm on purpose, i.e beams are not crossing. By comparing two miss-aligned sets of experimental measurements, experimental mean pulse shapes are obtained and there is no clear indication that the beams are crossing well or not. Moreover, the resulting mean pulse shape result is very similar to valid experimental mean pulse shapes of neighboring crossing points. Simulations, on contrary, show that the PSCS is inefficient when γ-ray beams are not crossing. This is the main disagreement between simulations and experimental data and it is not yet explained. The shift test emphasizes the importance of crystal alignment in order to ensure that vertical and horizontal beams are properly crossing.

5.3 Experimental mean pulse-shape database

Three 2 mm pitch scans were performed for PSCS purpose as shown in fig. 5.5:

- one in vertical position with a front illumination of the crystal (called V),
- one in horizontal position with a side illumination and sectors C and D oriented towards the collimator (H_{CD})
- one in horizontal position at 90° (rotation around the Z-axis of the crystal) relative to H_{CD}, with section E toward the collimator (H_E).

Each scan can be used with each other in order to perform PSCS, such that 3 experimental databases can be generated by comparing V/H_{CD}, V/H_E and H_{CD}/H_E. Of course the three databases should be identical. These scans were performed in order to evaluate the best solution between a vertical/horizontal comparison or a horizontal/horizontal comparison. In the first case, the vertical scan imposes severe restrictions for interaction location radii and the azimuthal angle, at the expense of a lack of statistics in the rear slices of the crystal due to γ-ray attenuation. In the second case, one could expect a better selection along the Z-axis of the detector and distributions with larger statistics. However, the two pulse-shape distributions used for comparison are globally more similar, leading to poorer spatial resolution of selected events or even slower comparison.

5.3.1 Considerations about time and data volume

Any PSCS in the whole volume of an AGATA detector implies a large amount of measured data. Pulse shapes of each 37 channels are digitized and stored for days at a rate of about 1000 ct/s. A lot of data are useless because of a radical selection of events before the χ^2 test:

- only 1-fold events are used such that any linear combination of a net charge signal with a transient signal is rejected

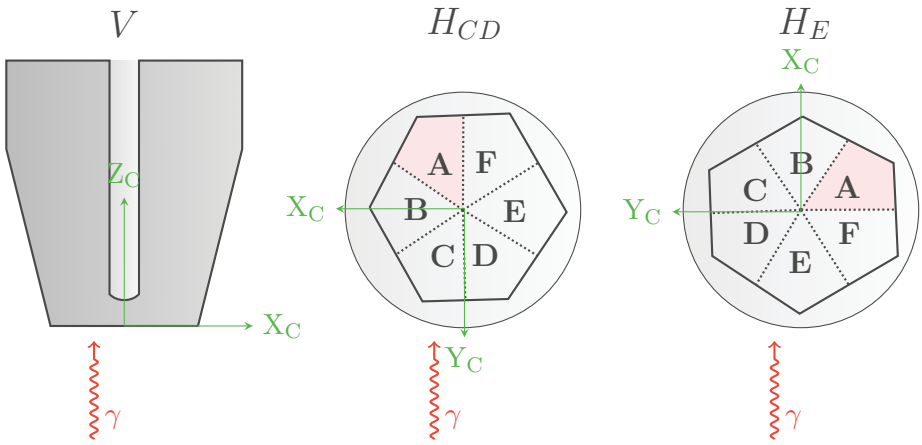

Figure 5.5: Schematic view of the detector orientation relative to γ-ray beam for the three 2 mm pitch scans performed for PSCS purpose. The crystal reference axes are labeled in green color.

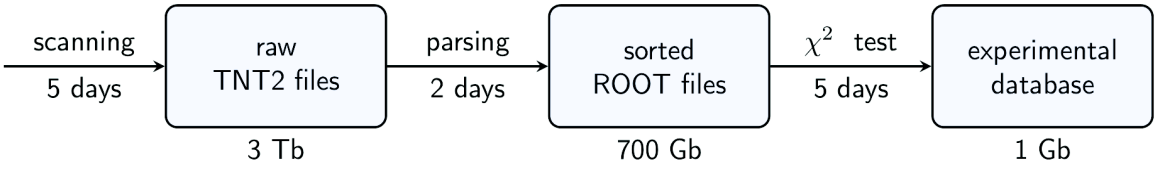

Figure 5.6: Data path from raw files to final database for a typical vertical/horizontal PSCS.

- only 662 keV events are used, this is a way to get rid of any natural radioactive background, and to be sure that the interacting γ-ray comes from the collimator.

After scanning, a first filtering and sorting step is required. Raw TNT2 files are parsed in order to retrieve information coming from a unique event thanks to the timing tag. If the event is complete and if it satisfies the above criteria, pulse shapes are filtered as described in 3.4.3 and the event is stored in a ROOT file [59]. As several tera-bytes of data are to be analyzed by reading 20 files simultaneously (10 TNT2 cards producing each a pulse-shape and an energy file), the speed of this step is limited by the hard drives read/write access of the analyzing computer. Sorted data are stored in ROOT files which are input of the χ^2 test algorithm. A 5 day scan generates 3 tera-bytes of raw TNT2 files which are compressed in 2 day computation to less than 1 tera-bytes of sorted ROOT files (see fig. 5.6).

5.3.2 Raw database sorting after PSCS algorithm

The output of the χ^2 analysis does not reflect exactly the detector pulse-shape response, even after the mean pulse-shape refinement. Some points are validated by the test although they have no physical meaning such as points within the bored hole or points outside of crystal physical boundaries. One crucial point is that the χ^2 test algorithm has no input concerning the detector geometry or internal/external segmentation. Experimental points are evaluated within a volume bigger than the crystal size. If an evaluated point is outside the detector

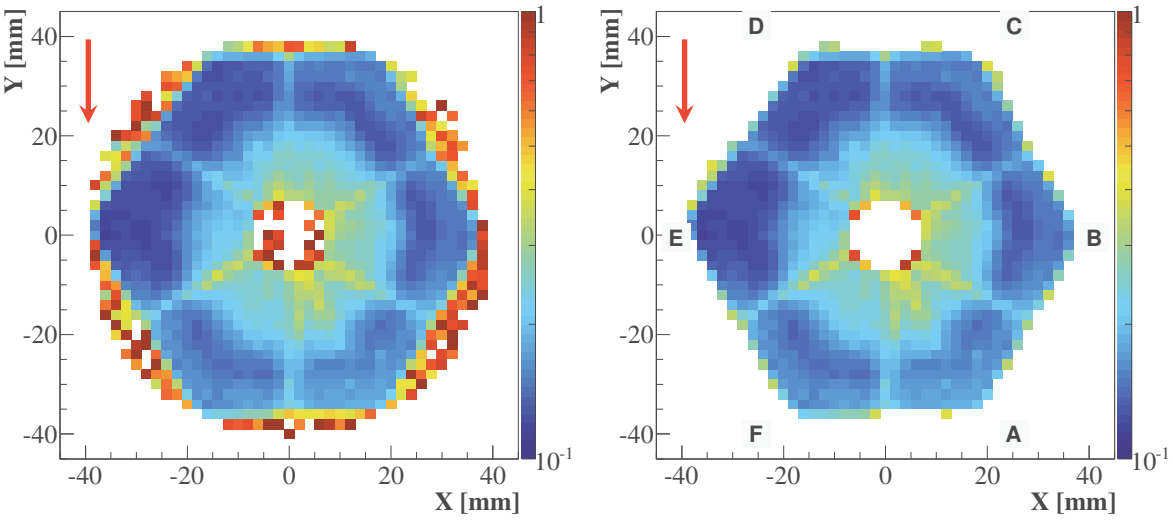

(a) (b)

Figure 5.7: Final χ^2 values after a V/H_{CD} PSCS for evaluated points with Z=28 mm. Panel (a) shows all PSCS results while panel (b) shows remaining points after threshold filtering. The arrows indicate the incident direction of the γ-rays for the lateral scan.

physical boundaries, it is expected that the pulses shapes are too different from each other, leading to a too large final χ^2 value, so high that it can be a rejection condition. This behavior is shown in fig. 5.7(a): the final χ^2 value after PSCS is plotted for a 2 mm thick slice at Z=28 mm for the V/H_{CD} comparison. The crystal hexagonal geometry at this depth is clearly visible in blue, but PSCS gives results even outside the detector or inside the bored hole, regions in which the χ^2 value is close to 1 and anyway larger that 0.5.

For extreme cases, the χ^2 test algorithm is unable to determine any mean pulse shape because there is no similar traces between the two compared distributions. Several reasons can justify this :

- beams are not crossing in the crystal,
- beams are crossing in a location with very low photopeak efficiency: typically on a segment boundary or a segment corner,
- beams are crossing in an uncollecting region of the crystal, on the n+ contact for example.

Most of the time, these points have a final χ^2 value small enough to be validated by the χ^2 test but it is also large enough to reject them using a simple low-pass threshold. As an example, for the V/H_{CD} comparison, 50 000 8mm^3 voxels are validated by the PSCS algorithm, which correspond to about 2100 g of HGPe. According to the manufacturer the B006 crystal weights 2043 g. As there are dead layers and as only points where full charge collection is reached are considered, it is expected that the active volume of the crystal is less than 2043 g.

Two χ^2 thresholds are used in order to reject fake points. They are called internal and

external thresholds. The external threshold allows to reject points which are supposed to be outside of the detector. As the statistics is globally very high close to the crystal external surface, the PSCS is very efficient, which lead to very small final χ^2 values for each scanned point. A low threshold allows to reject points which final χ^2 value is good but not enough for this specific crystal area. The internal threshold is higher in order to take into account the reduction of statistics occurring around the bored hole or around segment interfaces, leading to larger residual χ^2 values around the external boundary.

Using such criterion to reject fake points, only 48000 scanned experimental points remain, corresponding to 2000 g of HPGe. This is in agreement with what is expected. The rejection effect is shown in fig. 5.7(b) where only points matching the crystal geometry remain.

Another information given by this figure is a qualitative evaluation of the local full-energy efficiency of crystal voxels, corresponding to the vertical and the horizontal scan used for pulse shape comparison. It is clear that the χ^2 value is lower towards the outer mantle than towards the bored hole and also lower on segmentation interfaces. This is related to the amount of pulse shapes usable for comparison within each voxel, i.e. a local full energy efficiency. An example is the χ^2 value which is smaller in the DC area than in the AF area (lighter blue). This is due to the H_{CD} scan where sections B and C have more statistics than A and F because of γ-ray attenuation in the crystal (see H_{CD} in fig. 5.5). A corollary is that the final χ^2 value is also a confidence index. As shown in section 5.2, distributions with large statistics as an input to the PSCS software improve the spatial FWHM of selected pulse shapes. Then, mean pulse shapes with very small final χ^2 value are trustful, while those with larger χ^2 value might mismatch reality.

5.3.3 Mean pulse-shape results

Experimental mean-pulse signals have an averaged noise. This could be a drawback for the use of such database for PSA purpose in AGATA, compared to simulated perfect signals, because noise may lead to mistakes during the comparison process. An example of supertrace for a mean pulse shape is plotted in fig. 5.8. The energy deposit is located in segment F4. Relevant transient charge signals are localized in direct neighbor segments left/right (E4/A4) and top/bottom (F3/F5). A zoom on the baseline noise shows typical patterns even for segments far from the γ-ray interaction. This corresponds to Core/segment derivative cross-talk effects described in [8]. Signals rise enough from the baseline noise, such that PSCS manages to evaluate them. Cross-talk is restrained below 0.4% of the maximum signal, which is in good agreement with bibliography, and emerge clearly from the white noise, meaning that the residual noise is very low ($<$0.1%) in the final mean pulse-shape database.

The pulse-shape evolution versus the interaction location is shown in fig. 5.9, 5.10 and 5.11. Each mean pulse shape is aligned at 1 percent of the maximal amplitude set at 10 ns. This is very close to the T0 perfect alignment and it is made possible because the residual noise is very low. These pulse shapes are taken out of the H_{CD}/H_E experimental database.

Pulse shape variations along radius are shown in fig. 5.9. The interaction location goes from the center of the crystal to the external surface in segment E4 by 2 mm steps as shown in the two inserts. The behavior of net charge signals has already been explained in section 4.5. The one of transient pulses is explained here. As electrons (holes) drift towards a decreasing (increasing) weighting potential, the combination of both signal is quite complex.

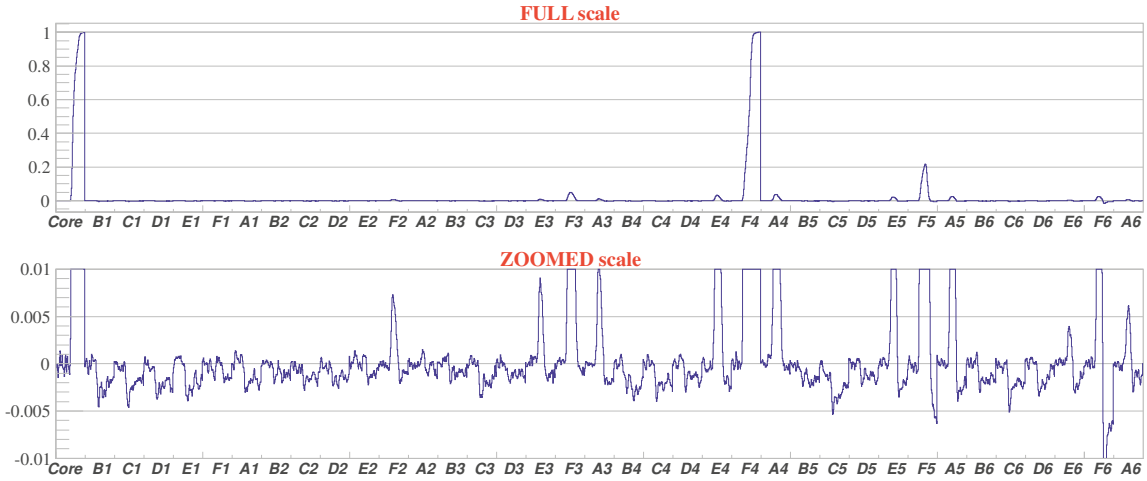

Figure 5.8: Supertrace of one experimental mean pulse shape with a normalized scale (top panel); zoom on the baseline noise (bottom panel).

For small radii, electrons reach quickly the Core electrode while holes have to move along the entire crystal radius. Transient signal is then fully driven by holes contribution and reaches a positive maximum. Reversely, for large radii, holes are immediately collected, and the full electron negative signal is visible. For interaction locations at intermediate radii, hole and electron contribution cancel themselves while both charge clouds are drifting simultaneously, leading to a bipolar, small amplitude pulse shape.

Relative amplitudes of F4 and D4 signals are almost identical because the interaction location is at equal distance of both segments. Amplitudes of E5 are larger than these of E3 because the interaction location is closer to E5 (4 mm) than E3 (14 mm).

The azimuthal position sensitivity is shown in fig. 5.10. The interaction depth is Z=50 mm as in fig. 5.9, in the same segment E4. The points the closest to a radius of 35 mm were chosen among the square grid of the signal basis. Azimuthal position is given by comparing the relative amplitude of D4 and F4 segments (see Image Charge Asymmetry, eq. 5.4). The amplitude difference between the minimum of F4 and the minimum of D4 is due to the asymmetric tapering of the crystal, leading to asymmetries in segment weighting potentials.

Even if depth and radius are identical between all points, Core and segment E4 net charge signals, E3 and E5 transient signals are not identical. As mentioned in section 4.5, the Core risetime for a fixed radius depends mostly on the charge-carrier mobility anisotropy. Indeed, in fig. 5.10, Core pulses shapes are sorted from the slowest to the fastest risetimes going from purple to orange location. Then, risetime goes slower again up to the red location. This behavior matches the crystallographic axis orientation visible in fig. 4.8, with a fast axis towards orange location and a slow axis towards purple location. F4 and D4 segments give the azimuthal location information, the closer the interaction occurs from a neighbor segment, the larger the amplitude of transient charge. This is due to the segment weighting potential profile which increases with segment proximity (see fig. 2.2(b)). In the same way, segment risetime for a fixed radius depends mostly on the electric-field strength, related to the external crystal geometry. Indeed, in fig. 5.10, the fastest segment pulses shapes are located

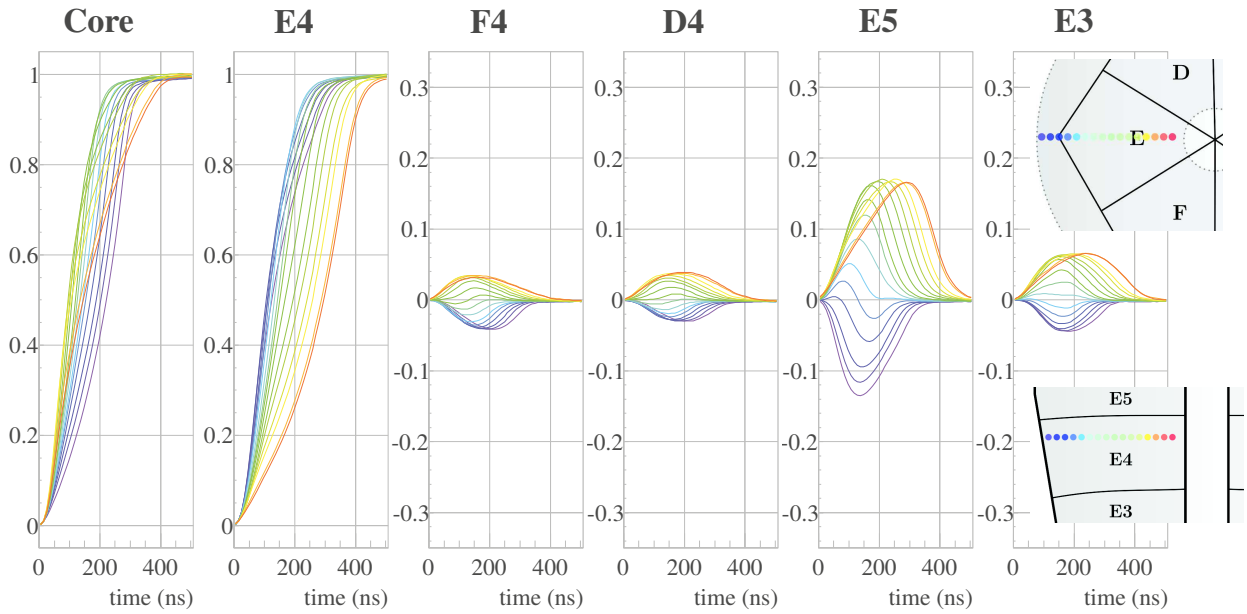

Figure 5.9: Experimental mean pulse shapes along the radius (along X) at Y=0 mm and Z=50 mm. The interaction location goes from the center of the crystal (red, X=8 mm) to the outer edge (purple, X=38 mm) by 2 mm steps.

at the segment boundaries where the crystal radius is minimum (red and purple locations), i.e. the electric field is maximum. The slowest pulse shapes are located on the edge of the crystal where the radius is maximal (light blue / green locations), i.e. where the electric field is minimum.

Segments E3/E5 variations are due to tangential mobility anisotropy of charge carriers, charges drift has a component along the Z axis which is positive or negative, depending on the electrical-field orientation in the Ge lattice (see fig. 1.9(a)). In this cases at large radius, the hole contribution can be excluded from the transient pulses. Segment E5 pulse shape has a larger amplitude when the interaction occurs at the corner edge (green color), which means that along this direction, electrons are drifting towards the upper segment. Reversely, segment E5 amplitude is lower along the segment boundaries, meaning that along this direction, electrons are drifting towards the lower segment.

Depth position sensitivity along the Z-axis is shown in fig. 5.11. The behavior in up and down segments is similar to the one of left and right segments in fig. 5.10. Unlike the azimuthal behavior of fig. 5.10, Core, E4, D4 and F4 channels are almost unchanged. As X and Y positions are fixed, geometrical effects are reduced and there is no charge-carrier mobility variations due to crystallographic anisotropy.

What comes out of these 3 mean pulse-shape figures is that PSCS manages to clearly distinguish pulse shapes for interaction locations separated by 2 mm in any direction. The smooth continuity between two consecutive points is a qualitative proof that the technique works well. Also, results are close enough from what is expected to explain locally weak effects such as mobility anisotropy.

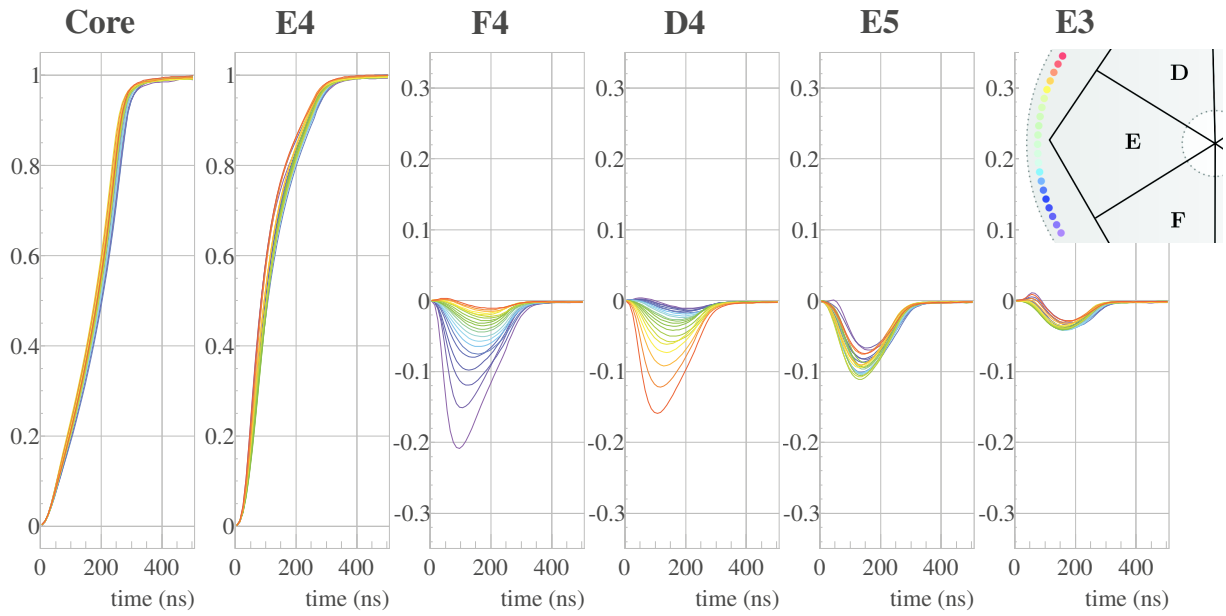

Figure 5.10: Experimental mean pulse shapes in E4, along an azimuthal line at a fixed radius of 35 mm. The interaction location goes from E4/F4 segment interface (purple) to E4/D4 interface (red). The closest points from the expected position are chosen among the 2 mm square grid.

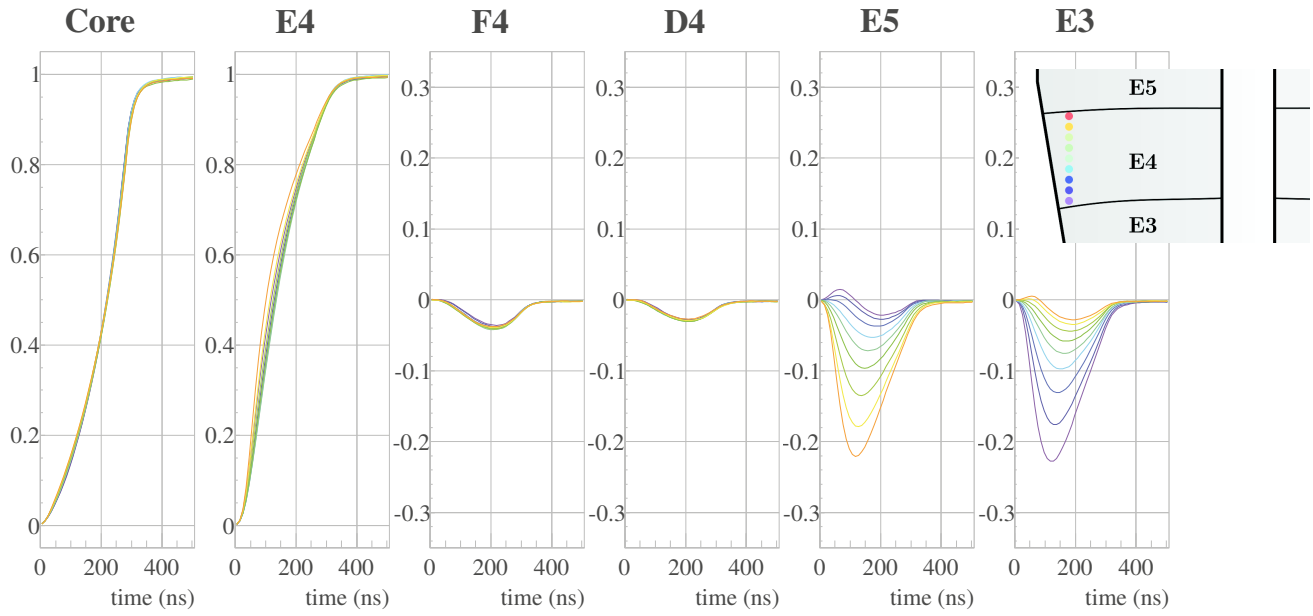

Figure 5.11: Experimental mean pulse shapes in E4, along the Z-axis at fixed X=-38 mm and Y=0 mm. The interaction location goes from E3/E4 segment interface (purple) to E4/E5 interface (red) by 2 mm steps.

An example of the 3D sensitivity of the PSCS technique is shown in fig. 5.12. The segment hit which was determined experimentally with PSCS in each voxel is plotted with a color scheme along several transversal cut of the V/H_E database, covering half-volume of the detector. This pattern arises naturally from the PSCS algorithm, as it has no input concerning crystal geometry. The first panels are filled with few points, corresponding indeed to cuts in the crystal tapering. The internal effective segmentation is well reproduced with the characteristic shape of the first slice, which is 8 mm thick at the detector external surface and goes thicker towards the bored-hole, with a maximum thickness of 16 mm. The following slice 2 is then very thin with a complex shape. The bored hole is also well defined on the last 4 panels with a 14 mm diameter along Y and 7 mm radius along X. The Ge thickness ahead the bored hole is 10 mm thick, which is in agreement with a 13 mm physical thickness and a n+ contact of 2-2.5 mm width.

5.3.4 Determination of the best scan for AGATA PSCS

Three pulse-shape databases are compared in order to determine which one is best for the PSCS thechique. In other words, is a vertical/lateral scan better than a lateral/lateral one. To do so, cuts are done in the 3D database to plot some relevant pulse shape parameters in 2D slices. Three parameters are used :

- final χ^2 value because it is the first parameter to evaluate the quality of the final mean pulse shape,
- segment T90 risetime, thanks to its smooth variation along the crystal radius, any fake mean pulse shape pops up clearly from a 2D plot
- segment image charge asymmetry. It is a widely used indicator allowing to parametrize the interaction location relative to neighbor segments. It is computed as follow :

$$\mathrm{ICA_{left/right}} = \frac{\mathrm{I_{left}} - \mathrm{I_{right}}}{\mathrm{I_{left}} + \mathrm{I_{right}}} + 1 \tag{5.3}$$

$$ICA_{top/down} = \frac{I_{top} - I_{down}}{I_{top} + I_{down}} + 1 \tag{5.4}$$

  where I is the absolute integral of the transient signal of the considered segment. The +1 is an offset in order to have only positive values, comprised in the [0,2] range. Top/down ICA has no meaning for first and the last slices of the detector because they have no down and top neighbor, respectively. For visualization purpose, the parameter plotted for these slices is the integral of the unique neighbor available, multiplied by a normalization factor.

Figure 5.13 shows such comparison between the three types of tests. A first immediate conclusion is that T90 and ICA plots are very similar. It means that PSCS is very efficient whatever are the scanning conditions. The pulse-shape distributions will be the same if the pencil beams cross at the same point whatever their orientation.

The T90 pattern is better defined that the one showed in fig. 4.9. T90 is measured in a 2 mm thick, sub-segment slice (a cut perpendicular to the Z crystal axis), while in fig. 4.9 T90 corresponds to an average over the whole slice thickness.

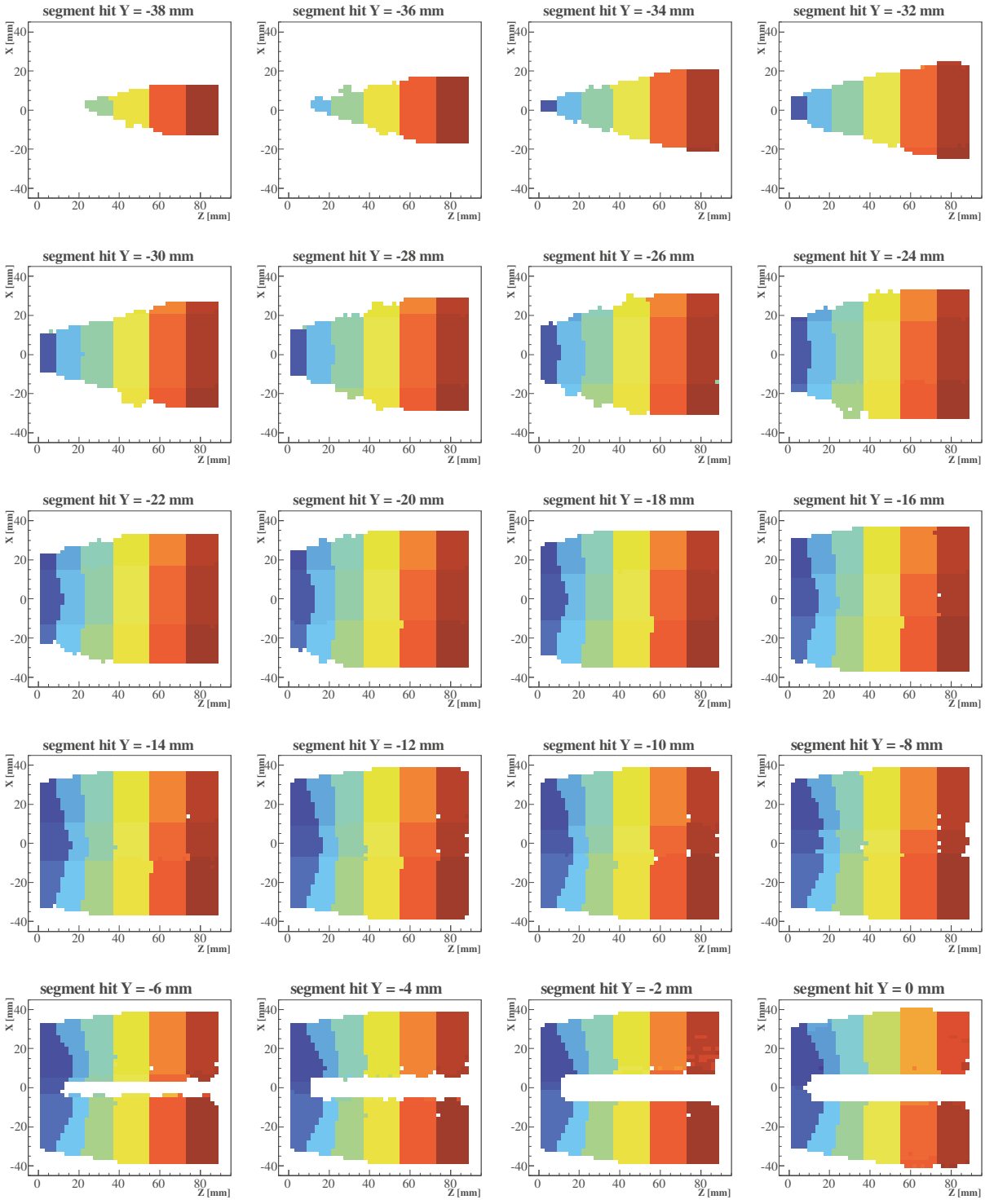

Figure 5.12: Distribution of segment hit for 2 mm thick longitudinal slices along Y. Each color corresponds to a different segment.

The ICA parameter has an almost linear azimuthal variation whatever the radius or the segment geometry. An exception lies in the specific radius in the middle of Ge where transient pules are almost flat, thus with a very poor azimuthal sensitivity.

However, some discrepancies exist between the 3 databases at few points. They are shown as odd single points emerging from the smooth continuum. They come out of segment interfaces or out of the bored hole limit. They are also correlated with a relatively high final χ^2 value. This is typically the result of a lack of statistics at the entry of the χ^2 analysis: first, only a fraction of the pencil beam covers the considered segment in this kind of area, secondly, the interaction occurs on the extreme limit of segments, where the photopeak efficiency is very low.

The lateral/lateral PSCS is affected by a non-expected phenomenon leading to a daisy crystal shape: the external true detector geometry is not exactly recovered. When two pencil beams cross near a corner, the sensitivity of the χ^2 test to induced signals in segments of the same slice is low (small induced signal amplitude) and similar pulse shapes will be selected. This phenomenon is less true when going away from the corners leading to the daisy shape. This is the main drawback of the lateral/lateral scan. The H_{CD}/H_E is therefore not the best one to return the true crystal response in this slice.

The same panels are plotted in fig. 5.14 for a 2 mm thick slice at Z=82 mm. Again, results are similar in the three PSCS. A large difference lies in the final χ^2 values, which are overall smaller in the H_{CD}/H_E comparison. There are also fewer odd points in this PSCS. An obvious explanation is that γ-rays of the vertical scan have to cross 82 mm of HPGe before interacting in this slice and are therefore strongly attenuated leading to lower statistics at this depth. This drawback is a major limitation to classical coincidence scans. It can be easily overcome with PSCS by using the lateral/lateral scan, with higher statistics in the rear crystal slices. It is noteworthy that, for cylindrical crystal geometry, lateral/lateral PSCS retrieves the correct crystal shape.

A similar figure is plotted again in fig. 5.15 for a 2 mm thick slice at Y=0 mm, which corresponds to a cut parallel to the crystal axis (longitudinal cut). Detector boundaries, as well as a 14 mm diameter bored hole are well defined. Again, this arises naturally from the PSCS and no geometrical considerations were imposed except the χ^2 threshold explained in section 5.3.2. In front of the bored hole, the crystal is geometrically 13 mm thick. The front face Ge thickness goes from 10 to 6 mm as the detector radius (X) goes from 6 mm to 2 mm. This may be explained as follows:

- the 2-2.5 mm thick n+ contact (see section 4.7) reduces the 13 mm down to 11-10.5 mm,
- the segmentation lines crossing at the front face of the crystal, resulting in poor charge collection, reduce single-fold efficiency.

Top/down image charge asymmetry ($\mathrm{ICA_{top/down}}$) behavior is similar to left/right ICA. The parameter variation with depth is almost linear except for radii where transient signals have small amplitudes and change polarity. This parameter variation is therefore not straightforward everywhere along the radius.

Finally, PSCS manages to retrieve mean pulse shapes efficiently for the three scanning conditions tested here. However, the PSCS which presently are considered as the most reliable are the V/H ones as they reconstruct naturally the crystal geometry. Nevertheless, it is possible to optimize the final mean pulse-shape basis by mixing the V/H and H/H scans,

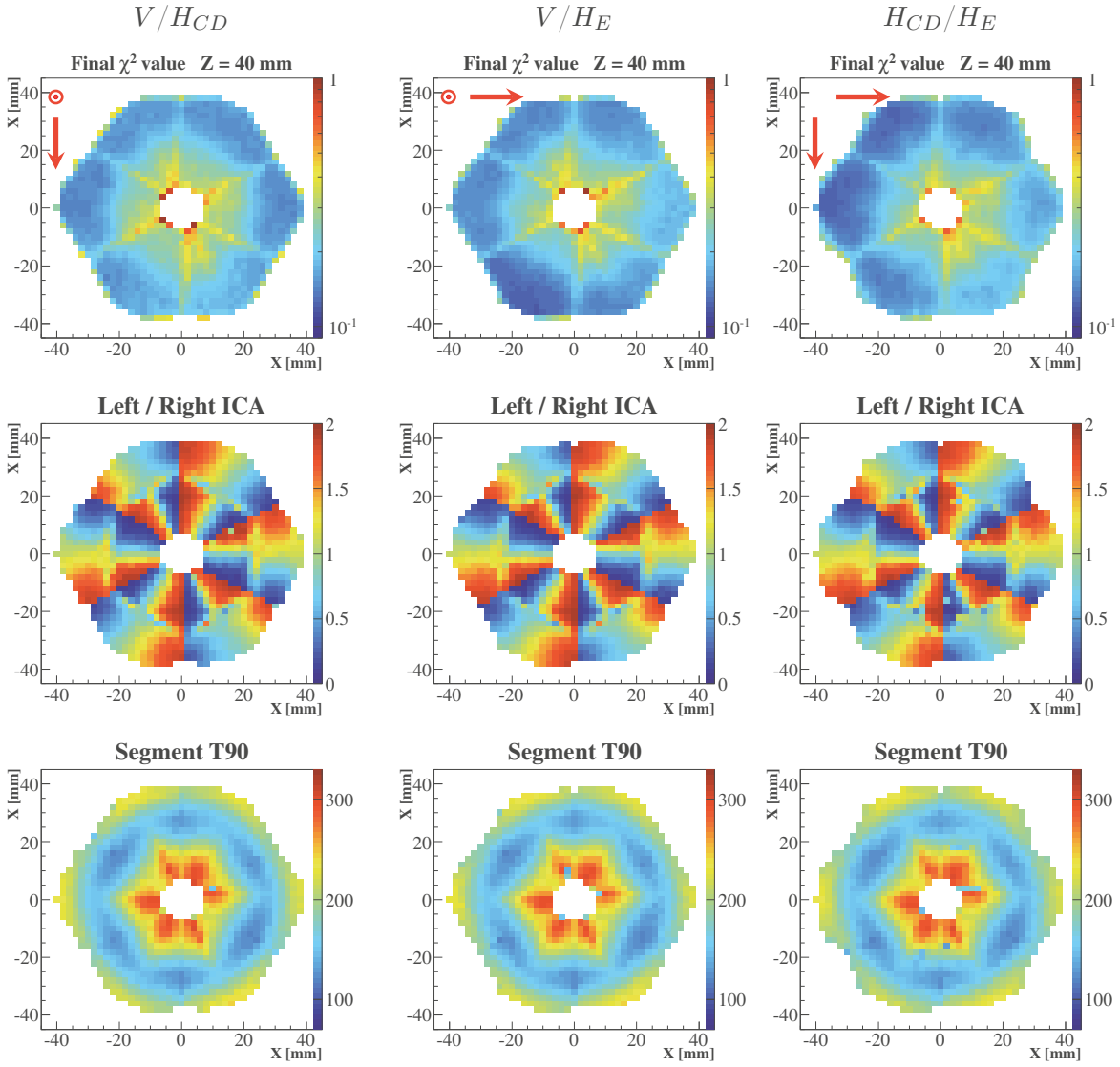

Figure 5.13: Comparison of three PSCS databases for cross-section Z=40 mm, slice 4. Top figures: final χ^2 value after PSCS, middle figures: left/right ICA, bottom figures: segment T90 risetime in nanoseconds. Arrows and points show the incidence direction of γ-ray of the two scans used for mean pulse-shape determination.

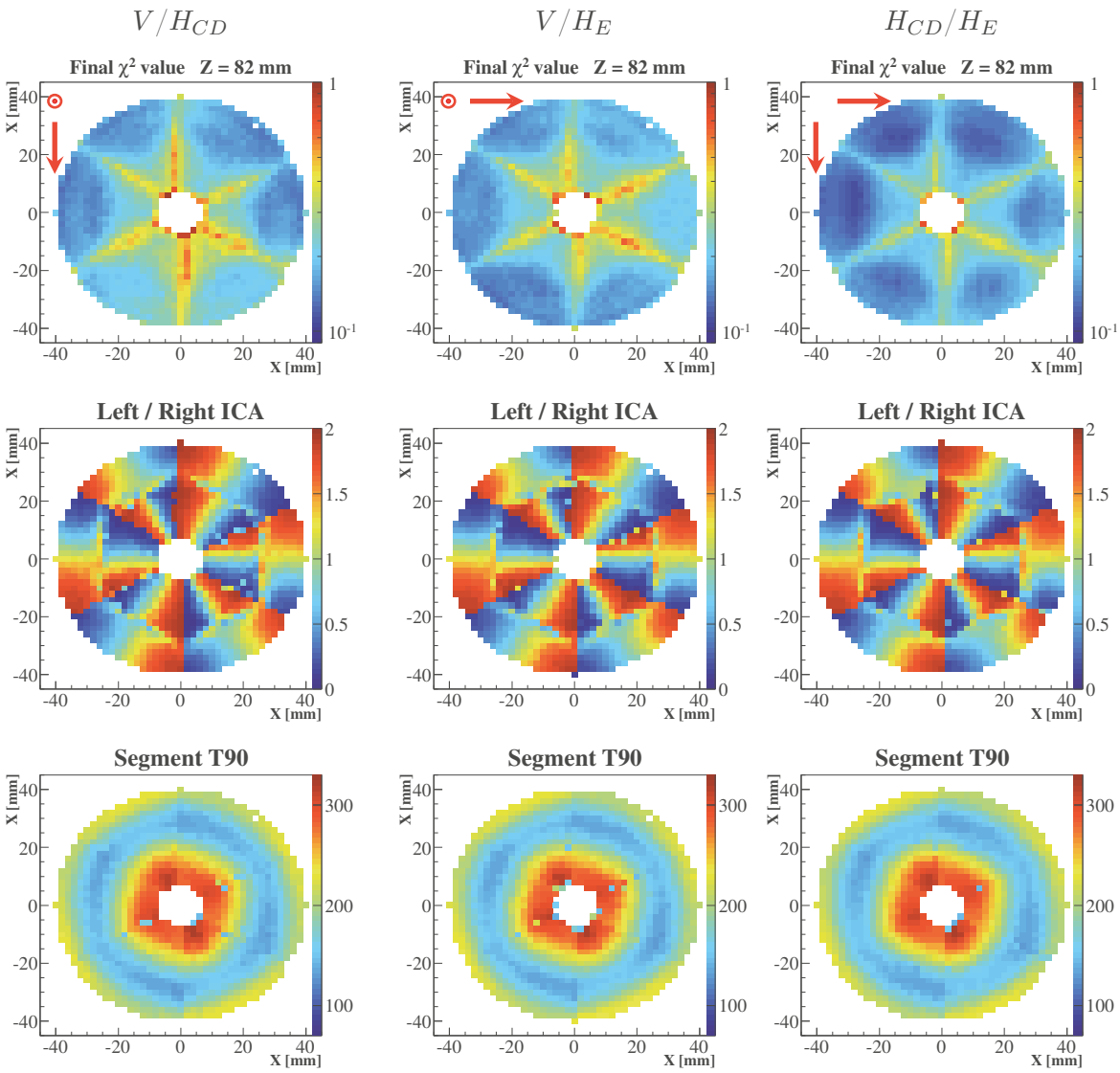

Figure 5.14: Same figure as 5.13 for cross-section Z=82 mm, slice 6.

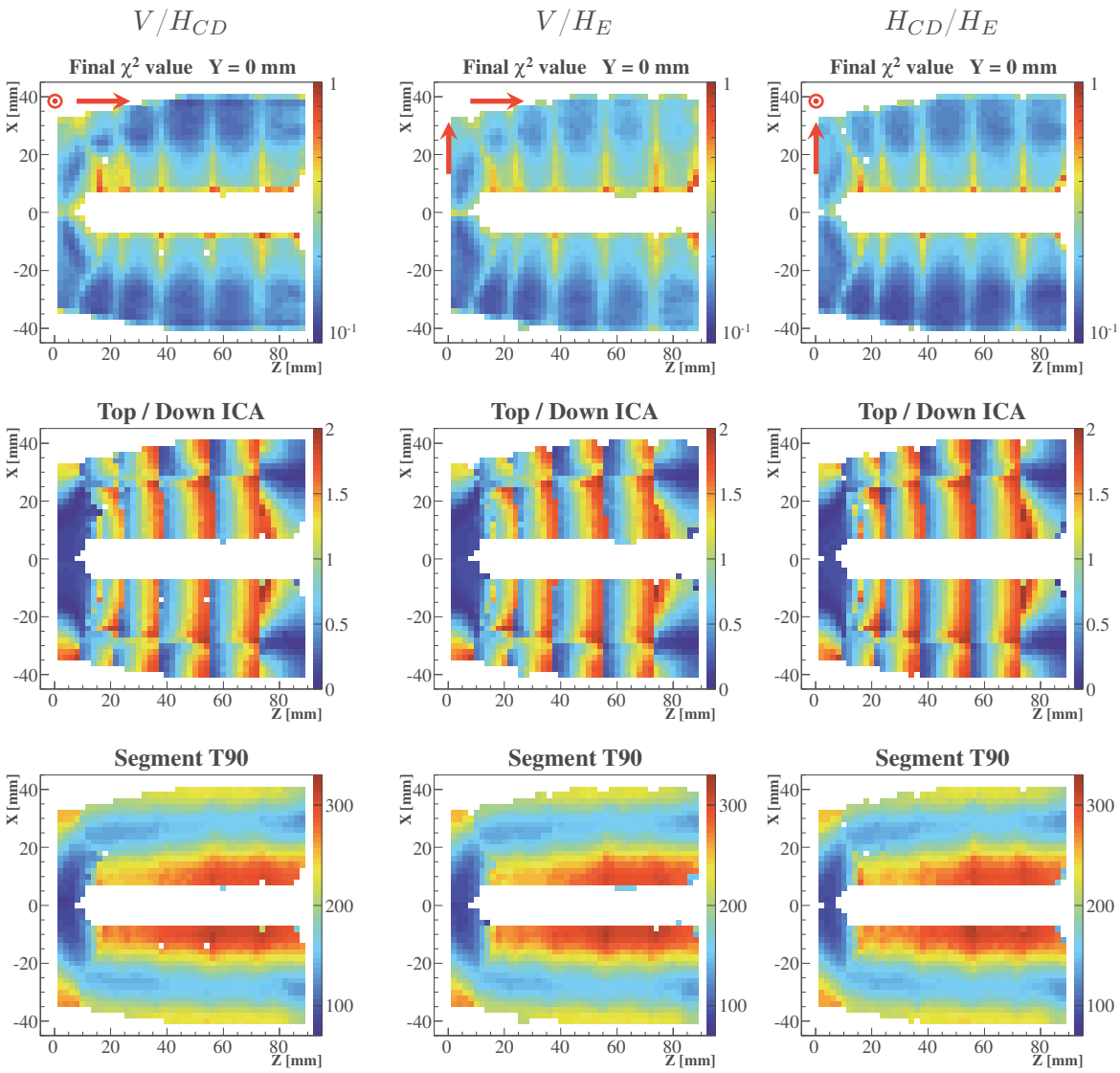

Figure 5.15: Same figure as 5.13 for cross-section Y=0 mm.

the former for the front part of the crystal, the latter for the two last slices of the crystal, improving statistics and consequently the final χ^2 values.

5.3.5 Comparison with ADL basis

The AGATA Detector Library (ADL), is a C++ library which was developed at the Insitut für Kernphysik, Cologne, and which simulates the AGATA detectors pulse-shape response. This is done same-wise as described in Chapter 2. A complete description of the simulation can be found in [67].

The experimental V/H_{CD} pulse-shape basis is compared with the B006 ADL simulated basis currently used for pulse-shape analysis in the AGATA array [68]. Various steps are required to compare this basis to the experimental one:

- ADL coordinate system is changed to the detector scanning system, the ADL basis is tilted by 60° along the Z-axis compared to the experimental basis, such that there is not any identical point between two bases,
- simulated pulses are digitized to 100 MHz, then corrected with a restrictive low-pass filter (see sub-section 2.5.3),
- pulses are aligned in time (see sub-section 3.4.3).

Experimental pulse shapes are also affected by derivative cross-talk, which modifies pulse-shape risetimes. Derivative cross-talk is significant only for direct neighboring segments. Each measured signal in a segment induces to its direct neighbors a derivative signal which amplitude is proportional to the measured signal risetime. These effects can be taken into account by calibrating derivative cross-talk for each channel, using the procedure described in [39]. This has not been done here and there is no derivative cross-talk contribution in simulated signals. However, the experimental signal basis should contain enough information to do such calibration.

The low-filter simulates the long decay and the limited bandwidth of the whole electronic chain. A major effect of this filter is a drastic shape smoothing, which attenuates significantly slight pulse-shape variations. This effect is so strong that, pulse shapes coming from other crystal geometries become similar with each other. This effect is shown in fig. 5.16 and 5.17: an experimental pulse shape measured at position (X,Y,Z) (thick red line) is compared to simulated pulses at the closest location of various ADL databases (<0.5 mm). B006 simulated basis is chosen for main comparison, but also the one of B005, A004 and C003 are chosen arbitrarily for check. Figure 5.16 corresponds to an interaction point in segment B4 close to the bored hole and slightly nearer to slice 5 than 3. The interaction point in fig. 5.17 happens in segment E4, close to D4 on one side and to E5 on the top The comparison of experimental and simulated B006 pulse shapes shows that global pulse lengths, shapes and transient charge amplitude are quite well reproduced which indicates that the electronic filter used is relevant. Note that even without individual time alignment for transient charges, they all start simultaneously which shows that our digital acquisition electronics is intrinsically well aligned. From these plots, it is tricky to determine which simulated basis reproduces best the experimental B006 one.

There are two ways to deal with such results. If one considers that simulation and experiment are in good agreement in fig. 5.16 and 5.17, then one has to accept that the spatial

resolution of PSA has an inferior limit given by the limited bandwidth of the electronics. It would be useless to look for specific crystal pulse-shape variations because they would be completely smoothed out by the electronics. In this case, it would be unnecessary to have a dedicated basis for each crystal but one single experimental basis per crystal geometry would be used, thus simplifying the whole PSA analysis.

On the other hand if one considers that simulation and experiment do not match sufficiently, further investigations have to be done concerning simulation, electronics filtering and detector scanning in order to find which one fails most. What is most probable is that each part of this chain has shortcoming:

- Simulation suffers of simplifications in several domains such as crystal geometry, doping profile, charge-carriers drift, junction properties or passivated surfaces properties. Thus it can not reproduce correctly pulse shapes everywhere in the detector.
- True electronics response is more complicated than the simple convolution described here. Each channel should be calibrated with its own parameters in order to take into account eventual electronics component variation. Also it should include cross-talk effects and particularly derivative cross-talk.
- PSCS retrieves an average pulse shape which does not correspond exactly to the expected one. Although both are often similar, significant differences can arise mostly on interfaces or in low statistic cases. Standard coincidence methods are also averaging the final pulse shape because of the significant width of collimators used.

This means that one is currently limited in pulse-shape simulation as well as in experimental pulse-shape evaluation.

Figures 5.16 and 5.17 show that the core signal is poorly reproduced. This is attributed to the n+ junction properties which have been demonstrated to be different from what is expected (see section 4.7). Also, some figures plotted in [53] show that ADL simulation does not reproduce well the geometry of the bored-hole end. It is simulated as a perfect hemisphere whereas the true geometry is a quasi-hemisphere. The consequences are relevant as it changes the electric field behavior in the front of the crystal. For these reasons, the Core signal is not taken into account for further simulated vs. experimental comparisons.

The whole crystal volume is evaluated as follows: the experimental pulse-shape basis is compared to the simulated one with a χ^2 test in order to find the best fit. The spatial position of the best fit is the result of the test. For each crossing point the shift between the experimental position and the one obtained from the simulated basis after χ^2 test gives an information about the equivalence of experimental and simulated databases. Results are shown in fig. 5.18 for two different depths in the crystal. At Z=6 mm, points are well reconstructed in the peripheral part of the crystal, but not towards its center. There is a strong tendency to aggregate towards lower radii which means that pulse-shape risetime is not well reproduced, i.e, charge-carrier drift in this area is not well simulated. Another possibility is that risetime in this region is so fast that there is a strong derivative cross-talk effect. In these cases, even if transient pulses have the correct amplitudes, they will not have the right length, and the χ^2 test will hardly give an accurate information about lateral location. This may also explain the clustering tendency towards segment center where left and right neighbor transient pulses are almost zero, which minimizes χ^2 value. The two first slices of AGATA detector are of extreme importance because they gather most of the first

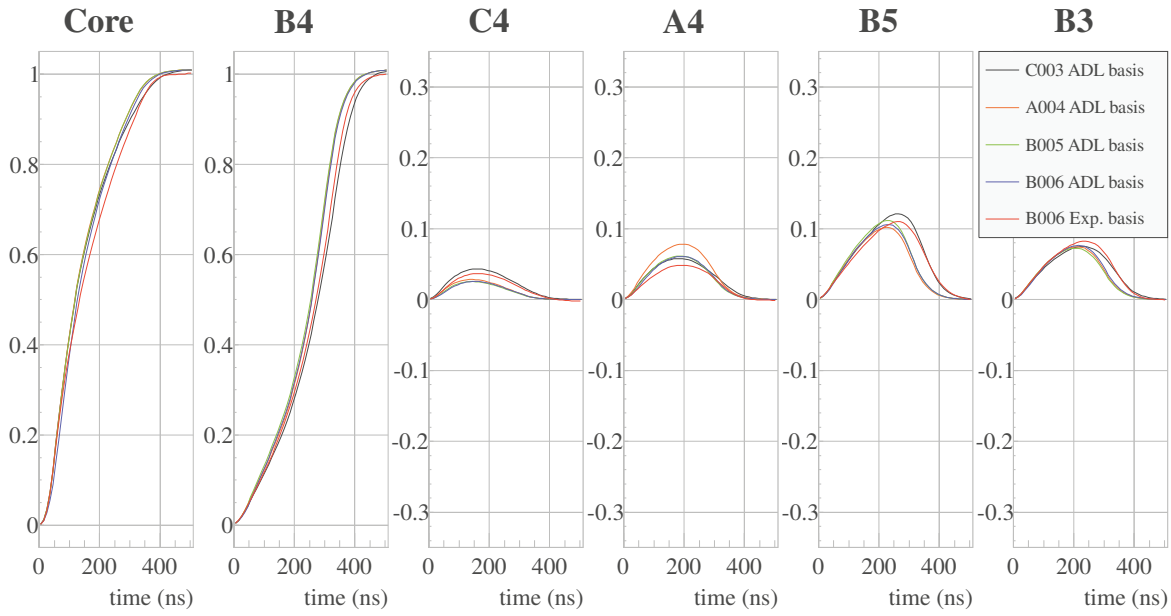

Figure 5.16: Comparison between B006 experimental basis and several ADL bases at position X=10, Y=0, Z=48 mm

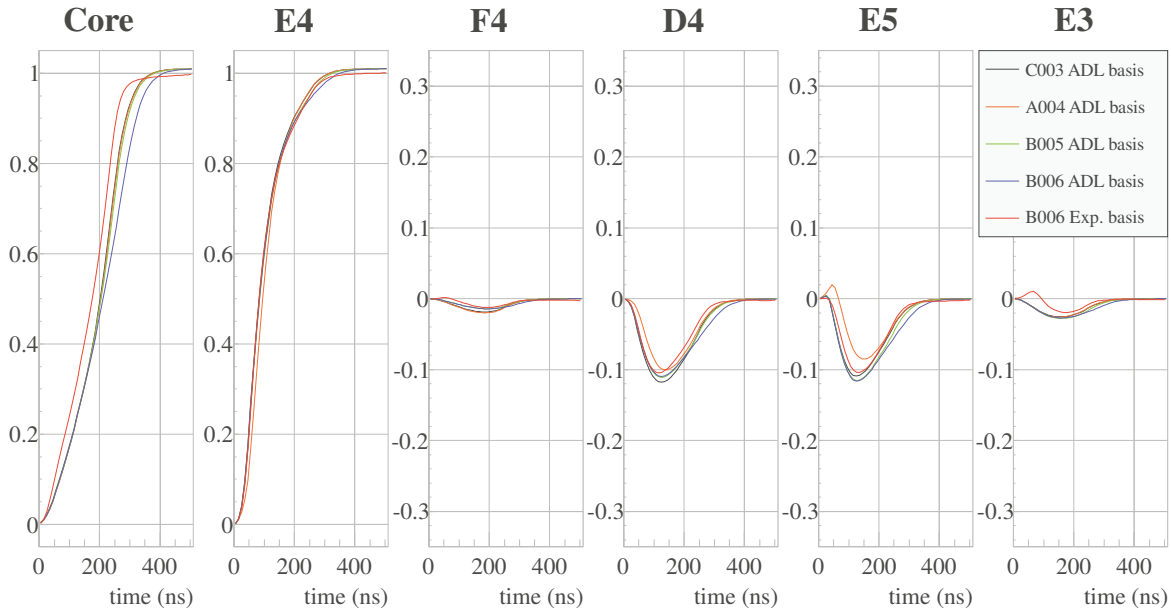

Figure 5.17: Comparison between B006 experimental basis and several ADL bases at position X=30, Y=-4, Z=48 mm

γ-ray interactions during physical experiments. A failure to evaluate simulated pulse shapes lead to miss-behaviors in the PSA and finally to systematic errors in the γ-ray tracking.

Simulations give better results in the coaxial area at Z=68 mm. Large shifts located in segment center can be attributed to two phenomena.

1. **Derivative crosstalk effects:** the area in the segment center contains transient pulse shapes which are almost flat. Derivative crosstalk creates slight bumps which are considered as a significant transient charge amplitude by the χ^2 test. The result is a shift towards the supposed corresponding transient charge.

2. **Inaccurate electron/hole drift speed simulation:** transient pulse shapes are the combination of a positive contribution of electron and a negative contribution of holes. In the segment center region, both contributions have a similar amplitude at a given time, such that they cancel themselves. The resulting signal has a wave shape with very low amplitude. If the mobilities of either electrons or holes are not well parametrized or if the simulated electric field is not realistic enough, the position where both contributions are maximal may be shifted, leading to variations of the wave shape. As transient charges have very low intensity in this region, any slight difference will lead to large discrepancies between experimental and simulated pulse shapes.

High shifts area on the top right of this figure could be explained by a high derivative crosstalk between segments B5 an C5. Or by the fact that simulation does not reproduce the segmentation line shift depicted in sub-section 4.3.2. One advantage for the use of experimental databases instead of simulated ones is that the latter one includes naturally any effects resulting of any divergence compared to the expected crystal behavior.

These effects are correlated to a low position sensitivity in the center of segments, which is a drawback of the AGATA crystal segmentation pattern. This issue can hardly be resolved without completely change the crystal design. New designs, such as the one described in [6], are currently investigated, but they carry other drawbacks.

Another comparison is performed on the Y=0 mm longitudinal cut in order to evaluate reconstruction along depth. Results are shown in fig. 5.19. The worst simulated areas are in the first and in the last slices of the detector. Both areas have already shown to badly behave and this has noticeable effects on interaction location reconstruction. In the rest of the volume, shifts towards the segment centers can be related to either derivative cross-talk or mistakes in the charges drift speed parametrization, as already explained. These effects are larger where transient signals are of small amplitude.

Systematic shifts are evaluated in the whole crystal volume for various simulated ADL databases. The average 3D shift in each 2 mm thick slice is plotted against the detector depth in fig. 5.20. Each ADL database, even those from other crystal geometries allow to determine the interaction locations within 3-4 mm except for the first and the last slices. These values are larger to the ones from the work done in [69] where experimental pulse shapes were measured with coincidence scan technique and were compared to MGS [70] simulated database. In this work derivative crosstalk effect were also not considered. This is due mostly to the high granularity of the simulated grid used (1 mm^3 voxels, compared to 8 mm^3 ones in the present work). Also the detector was a symmetric prototype, easier to modelize. Obviously B006 ADL database is not the best to be used in order to reproduce

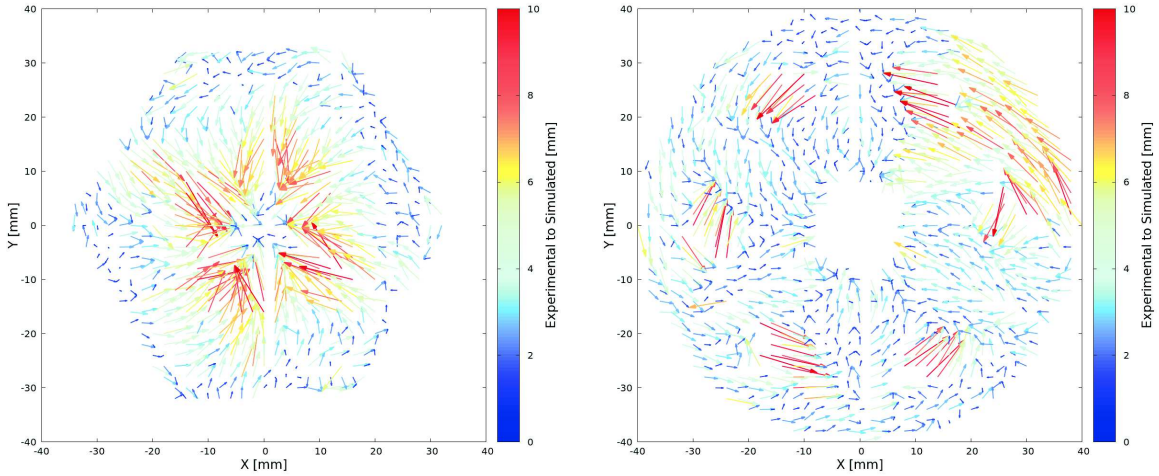

Slice Z = 6 mm
Average shift : 4.2 mm

Slice Z = 68 mm
Average shift : 3.8 mm

Figure 5.18: Arrow plots showing the pulse-shape discrepancies between experiment and simulation. Each arrow starts at the experimental voxel location and points towards the position of ADL B006 database which has the most similar pulse-shape. Two Z-fixed plans are shown, one in the front and one is the rear part of the crystal. Shifts larger than 12 mm are not shown.

B006 experimental pulse shapes. B005 is systematically better, and even C003 is closer to experiment at the rear of the crystal. As the rear of AGATA crystals are almost identical, i.e. coaxial independently from the crystal geometry, one might think that simulated C003 density of impurity (1.16×10^{10} cm^{-3}) is closer to reality than simulated B006 (0.7×10^{10} cm^{-3}). Even so, shifts in slice 6 are so large that it cannot be due only to spurious residual space charge values. Such phenomenon could be attributed to the passivated surface influence on the electric field. Reconstruction is also less efficient in the front of the detector (0 to 16 mm depth) reflecting issues already mentioned occurring in the first slices of the detector. Bumps at Z=38 , Z=56 and Z=72 mm correspond to the segmentation interfaces.

These comparisons are performed in the ideal case where pulses correspond to a single interaction in a single segment. Even there, ADL databases compared to the PSCS one reconstruct positions within a 4 mm range for ∼60% of the crystal volume. The shift is larger than 4 mm in the remaining ∼40%. The numbers remain almost unchanged whatever the simulated database used.

A crucial point arises by combining pieces of information deduced from this work. The AGATA crystal segmentation has been designed to get equivalent count rates in each segment during experiments, where γ-rays are emitted from the front of the crystal. Figure 5.15 shows that the effective thickness of the first slice is much larger than the second one. Obviously, the first slice focuses much more interactions than the next ones. As pulse shapes in this part of the detector are also not well reproduced by simulation, this segmentation geometry likely increases systematic errors in online PSA. Thus, any improvement in this area will impact the position resolution after PSA and consequently improve the tracking performances.

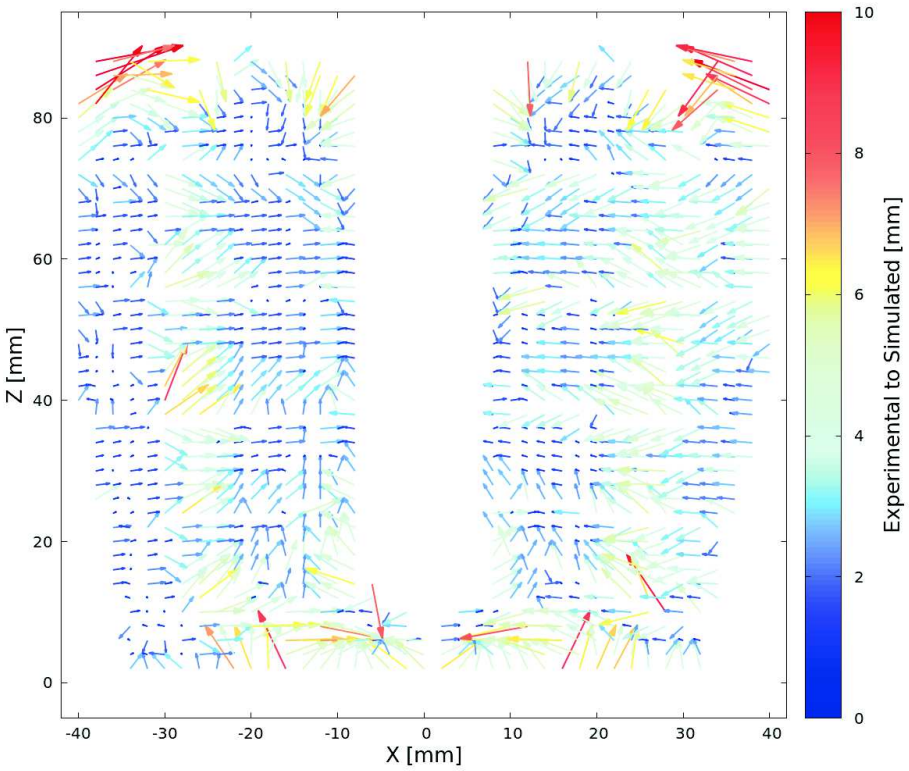

Average shift : 3.5 mm

Figure 5.19: Arrow plot showing the shift between the experimental pulse-shape position and the reconstructed position using ADL B006 database for the Y=0 mm plan. Shifts larger than 12 mm are not shown.

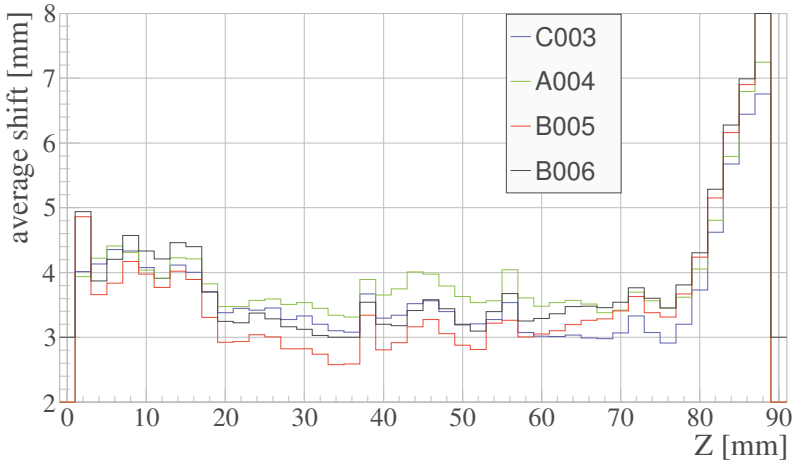

Figure 5.20: Average shift between experimental positions and recovered ADL positions for each 2 mm thick slices along the detector depth.

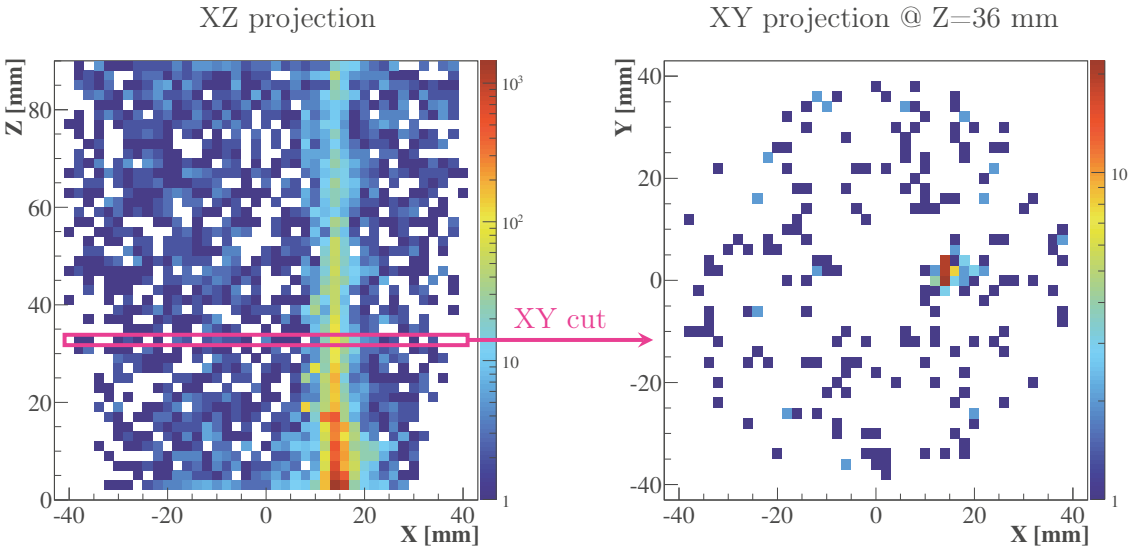

Figure 5.21: Recovered interaction position of 1-fold events in the 350-655 keV range for vertical measurement with the collimator at X=14 mm, Y=2 mm. The V/H_E experimental basis was used as reference.

5.4 Spatial resolution improvements with experimental database

A straightforward way to estimate the PSA reconstruction ability is to compare sets of measurements performed with the collimated γ-ray beam to the experimental pulse-shape database. The comparative procedure is identical to the one used in the previous section: each 1-fold event is compared to the whole database in order to find the best fit, which gives the location of the γ-ray interaction. After comparing each relevant event of the measurement, a spatial distribution is obtained and analyzed. Relevant events are filtered as follows:

- only 1-fold events are considered in order to be independent from any PSA algorithm looking from linear combination of several pulse shapes,
- the minimum energy deposit is 350 keV, thus minimizing errors due to signal noise,
- Compton events (in the 350-655 keV range) and photopeak events (in the 655-670 keV range) are analyzed separately because the latter are more likely to result from multiple γ-ray interactions in a single segment, thus smearing the final spatial distribution.

An example of reconstructed Compton events is shown in fig. 5.21 for which the V/H_E database has been used as a reference. In the left panel, the collimated γ-ray beam is well reconstructed in the crystal. The number of counts in each pixels decreases along the crystal Z axis following an exponential decay, due to γ-ray attenuation in germanium. Pixels filled in blue in the whole crystal volume are due to radioactive background, they do not appear when only photopeak events are considered. The right panel shows a projection in the XY plane at fixed depth Z=36-37 mm. The XY distribution of reconstructed events is well centered around the collimator position. A way to estimate the quality of this distribution is to determine the shift in the XY plane between the center of gravity of the distribution of reconstructed events of this figure, with the expected position (the one given by the collimator position).

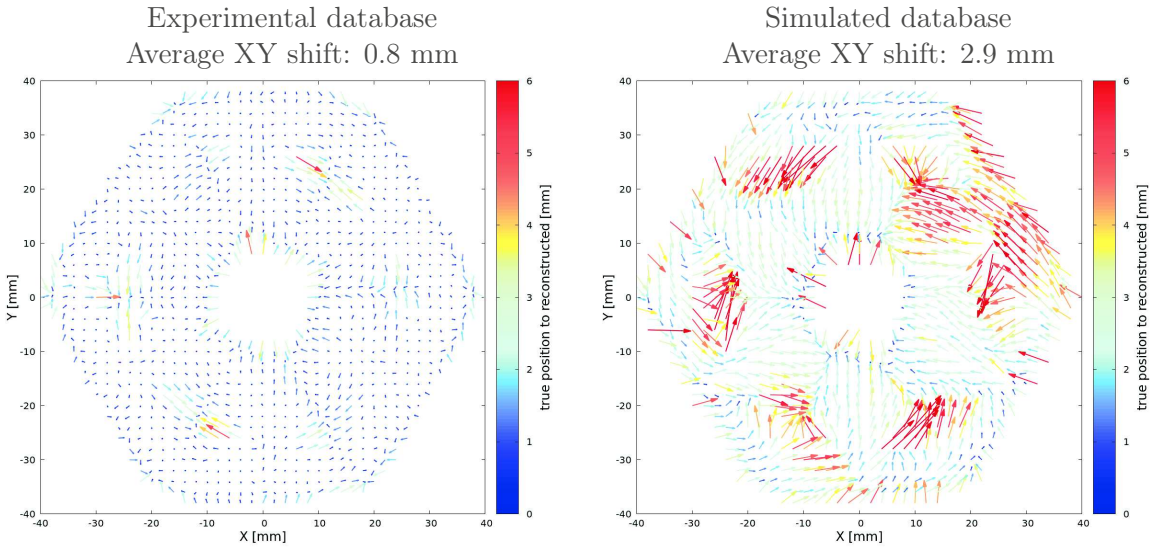

Figure 5.22: Shift in the XY plane, at Z=40 mm. Each arrow starts at the location given by the collimator position and points towards the center of gravity of the position distribution of the reconstructed 1-fold events. Left(right) panels show results using the experimental(simulated) database.

The FWMH of this distribution is also computed. For such computation, the background contribution is suppressed by setting the pixel value to zero for each pixel containing less than 4 counts. For this specific figure, after background suppression, the XY shift is 0.11 mm and the FWHM is 2.5 mm. Considering the 2 mm diameter of the beam spot, these values are very good. If one consider photopeak events (662 keV), these values raise to 0.43 mm XY shift and 3.0 mm FWHM which is still good.

A similar analysis has been performed in each voxel of the crystal volume. The XY shift distribution for a 2 mm thick slice at Z=40 mm with both experimental and simulated databases are given figure 5.22. Arrows are starting from the position of the collimator and are pointing towards the recovered pencil beam distribution after localization of 1-fold events. When the experimental database is used as a reference, the average XY shift is 0.8 mm, it is also uniform in almost the whole crystal section (left panel). There is an area in the center of each segment, where γ-ray interactions are not well localized. It corresponds to the less sensitive area of the detector, where the signal of moving electrons and holes cancel themselves in neighboring segments. The radial information is still accurately given by the net charge pulse shape (Core and hit segment), but the localization information which comes from transient charges is poor and hidden in the noise. A whole worsening of the localization performances is observed when the same events are compared with the simulated database (right panel). Almost each interaction distribution is shifted compared to the expected position and the average XY shift raises to 2.9 mm. This behavior shows again that both signal simulation and electronic response modeling fail to reproduce accurately experimental pulse shapes.

The XY shifts between expected and reconstructed pencil beam positions (averaged over each Z slice) is plotted as a function of the detector depth for several signal databases in

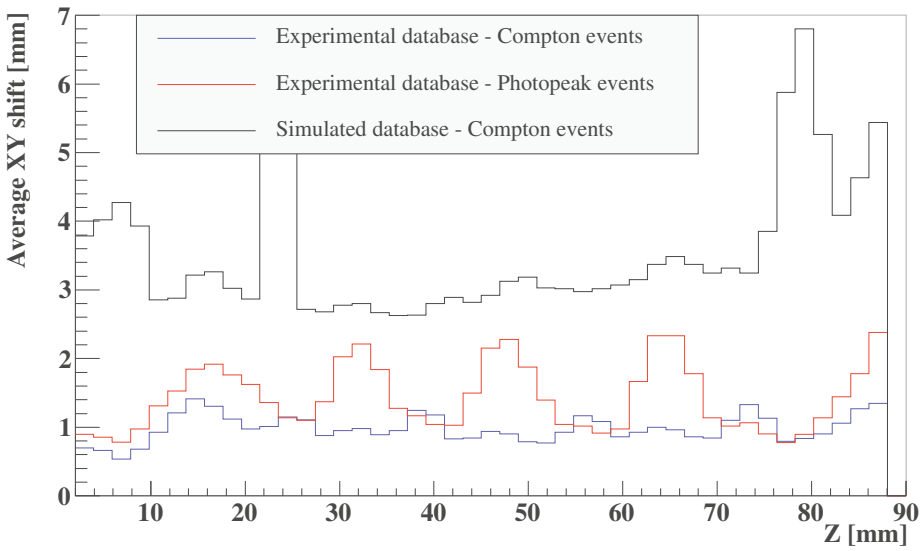

Figure 5.23: Average XY shift between expected and reconstructed pencil-beam positions along the depth of the detector.

Database	Energy range [keV]	XY shift [mm]	FWHM [mm]	Spatial resolution [mm]
experimental	655-670	1.44	3.92	∼3.5
experimental	350-655	0.99	3.41	∼2.5
simulated	350-655	4.27	4.02	∼6

Table 5.2: Results of the pencil beam reconstruction in the XY plane, averaged over all points reaching enough statistics to perform the analysis.

fig. 5.23. Same values averaged over the whole crystal volume are given in table 5.2. A non-physical bump arises with the simulated database at Z=22-24 mm, these points are excluded from the average. The localization of events is better for Compton events than for photopeak events, even if the latter have a better signal over noise ratio. This is because 1-fold full energy events result mostly from multiple Compton scattering, thus mixing information from several interaction positions which pushes the deduced position away from the real one. A PSA algorithm which looks for multiple interactions in a single segment should be used if one wants to perform an efficient tracking. The localization improvement is obvious while using the experimental database versus the simulated one. The 4.27 mm averaged XY shift (given with a 4 mm FWHM spatial resolution, see table 5.2) with the simulated database is in agreement with the global spatial resolution of ∼6 mm at 600 keV obtained with PSA applied to in-beam events, in [34]. The lowering of these values to ∼1 mm shift and ∼3.4 mm FWHM with the use of an experimental database should improve the spatial resolution. Taking into account the beam-spot width (∼2mm), the average XY shift convoluted to the distribution of position, we deduce that the AGATA spatial resolution is presently of ∼6 mm which could be improved to ∼3 mm, thus improving the overall array performances.

Conclusion

An AGATA coaxial, segmented detector has been investigated (crystal B006). Two dimension measurements, similar to the ones performed with other scanning tables, were performed giving access to local efficiency distributions and signal risetime distributions. Additional information was obtained, such as a slight electron trapping effect which was observed by looking at local photopeak centroid shifts. This effect is observable in the Core electrode which collects electrons, but also in segment electrodes which collect holes. Fine investigations along the inter-electrode area were performed, which highlighted charge deficit issues related to a specific mode of charge collection. Indeed, if the hole collection is localized on the inter-electrode area, the readout energy is split between the two neighboring electrodes i.e. a single γ-ray interaction can lead to the readout of two segments hit. Furthermore, the full energy readout is not reached neither in the summed segments nor in the Core. These surface effects concern only a small part of the detector volume and their characterization will allow to correct them in the future. For the first time, a complete experimental pulse-shape database of a large volume, segmented, AGATA detector has been established following a 2-mm pitch grid. This database contains the experimental information of 48 000 voxels. The 3D segmentation pattern is naturally reconstructed with the PSCS technique. Pulse shapes separated by 2 mm inside the crystal volume are clearly distinguished thanks to the amount of information given by the crystal segmentation and the PSCS technique performance. Experimental pulse shapes recovered by PSCS contain a residual noise which is low enough to directly observe Core-to-segment differential crosstalk, which has an intensity below 0.5%. Such signal to noise ratio allows for a direct use of the experimental database for Pulse Shape Analysis (PSA) in AGATA. Comparisons with various AGATA Detector Library (ADL) simulated signal bases have been performed, which reveal several issues concerning PSA. Firstly, there is a significant discrepancy between simulated and experimental signal which can either be due to misleadings in the modeling of the crystal electrical properties or to the charge drift properties. Secondly, the low-pass filtering due to the front-end electronics might be too severe to take into account slight pulse-shape variations due to crystal properties. Thirdly, the differential crosstalk amplitude might be underestimated. All these effects lead to uncertainties in the pulse-shape response modeling. It is expected that experimental signals which are measured with PSCS already contain differential crosstalk, thus minimizing its spurious effects when used for PSA purpose. Comparisons of ADL signals with experimental ones have shown that several simulated bases, even those calculated with different crystal properties, have the same behavior once smoothed by a severe electronic filter. This allows for an easier PSA but with a slight loss in the precision of interaction localization. Further work should use this experimental basis instead of a simulated one for PSA in the AGATA framework. It is

expected that such change improves significantly PSA performances. If so, AGATA crystals of geometry A and C should also be scanned. In a first step, the three experimental bases for A, B and C crystal types should be used for the corresponding detectors in the AGATA array. Due to the electronic smoothing, it might be useless to scan each crystal. If not, in a second step, the IPHC scanning table is able to scan each AGATA crystal individually in reasonable time, thus giving access to full experimental databases. Finally, the scanning table could be also used for detailed studies of HPGe detector characteristics in order to better understand their behaviors, correct for defects and improve their performances.

Bibliography

[1] G.F. Knoll. *Radiation Detection and Measurement – 4th edition.* Wiley, January 2000.

[2] NIST US Department of Commerce, M.J Berger, J.H. Hubbell, S.M Seltzer, J. Chang, J.S. Coursey, R. Sukumar, D.S. Zucker, and K. Olsen. NIST XCOM: Photon Cross Sections Database.

[3] Ervin B. Podgorsak. *Radiation Physics for Medical Physicists.* Biological and Medical Physics, Biomedical Engineering. Springer Berlin Heidelberg, Berlin, Heidelberg, 2010.

[4] S. Akkoyun et al. AGATA—Advanced GAmma Tracking Array. *Nuclear Instruments and Methods in Physics Research Section A*, 668:26–58, March 2012.

[5] I.-Yang Lee. Gamma-ray energy tracking array: GRETINA. *Journal of Physics: Conference Series*, 420(1):012156, March 2013.

[6] R.J. Cooper, D.C. Radford, P.A. Hausladen, and K. Lagergren. A novel HPGe detector for gamma-ray tracking and imaging. *Nuclear Instruments and Methods in Physics Research Section A*, 665:25–32, February 2011.

[7] M. Agostini, E. Bellotti, R. Brugnera, C. M. Cattadori, A. D'Andragora, A. di Vacri, A. Garfagnini, M. Laubenstein, L. Pandola, and C.A. Ur. Characterization of a broad energy germanium detector and application to neutrinoless double beta decay search in ^{76} Ge. *Journal of Instrumentation*, 6(04):P04005–P04005, April 2011.

[8] B. Bruyneel, P. Reiter, and G. Pascovici. Characterization of large volume HPGe detectors. Part I: Electron and hole mobility parameterization. *Nuclear Instruments and Methods in Physics Research Section A*, 569(3):764–773, December 2006.

[9] L. Mihailescu, W. Gast, R. M. Lieder, H. Brands, and H. Jäger. The influence of anisotropic electron drift velocity on the signal shapes of closed-end HPGe detectors. *Nuclear Instruments and Methods in Physics Research Section A*, 447(3):350–360, 2000.

[10] IEEE Nuclear and Plasma Sciences Society, Nuclear Instruments and Detectors Committee, IEEE Standards Board, and American National Standards Institute. *IEEE standard test procedures for germanium gamma-ray detectors.* Institute of Electrical and Electronics Engineers, New York, NY, 1997.

[11] J. Eberth and J. Simpson. From Ge(Li) detectors to gamma-ray tracking arrays–50 years of gamma spectroscopy with germanium detectors. *Progress in Particle and Nuclear Physics*, 60(2):283–337, April 2008.

[12] P. J. Twin, P. J. Nolan, R. Aryaeinejad, D. J. G. Love, A. H. Nelson, and A. Kirwan. TESSA : A multi-detector gamma-ray array designed to study high spin states. *Nuclear Physics A*, 409:343–351, November 1983.

[13] UK-France EUROGAM collaboration. Nuclear Structure in the Nineties; EUROGAM — a high efficiency escape suppressed spectrometer array. *Nuclear Physics A*, 520:657 – 667, 1990.

[14] F. A. Beck. EUROBALL: Large gamma-ray spectrometers through european collaborations. *Progress in Particle and Nuclear Physics*, 28:443–461, 1992.

[15] I-Yang Lee. The gammasphere. *Progress in Particle and Nuclear Physics*, 28:473 – 485, 1992.

[16] G. Duchêne, F. A. Beck, P. J. Twin, G. de France, D. Curien, L. Han, C. W. Beausang, M. A. Bentley, P. J. Nolan, and J. Simpson. The Clover: a new generation of composite Ge detectors. *Nuclear Instruments and Methods in Physics Research Section A*, 432:90–110, August 1999.

[17] P.M. Jones, L.Wei, F.A. Beck, P.A. Butler, T. Byrski, G. Duchêne, G. de France, F. Hannachi, G.D. Jones, and B. Kharraja. Calibration of the new composite CLOVER detector as a compton polarimeter for the eurogam array. *Nuclear Instruments and Methods in Physics Research Section A*, 352:556, 1995.

[18] J. Eberth, H. G. Thomas, P. v. Brentano, R. M. Lieder, H. M. Jäger, H. Kämmerfing, M. Berst, D. Gutknecht, and R. Henck. Encapsulated Ge detectors: Development and first tests. *Nuclear Instruments and Methods in Physics Research Section A*, 369(1):135–140, January 1996.

[19] J. Eberth, P. von Brentano, W. Teichert, T. Mylaeus, R. M. Lieder, W. Gast, G. Hebbinghaus, H. Jäger, K. H. Maier, H. Grawe, H. Kluge, D. Schwalm, J. Gerl, H. Hübel, R. Henck, and D. Gutknecht. Development of composite Ge detectors for EUROBALL. *Nuclear Physics A*, 520:c669–c676, December 1990.

[20] J. Eberth, G. Pascovici, H. G. Thomas, N. Warr, D. Weisshaar, D. Habs, P. Reiter, P. Thirolf, D. Schwalm, C. Gund, H. Scheit, M. Lauer, P. Van Duppen, S. Franchoo, M. Huyse, R. M. Lieder, W. Gast, J. Gerl, and K. P. Lieb. MINIBALL A Ge detector array for radioactive ion beam facilities. *Progress in Particle and Nuclear Physics*, 46(1):389–398, 2001.

[21] D. Gutknecht. Photomask technique for fabricating high purity germanium strip detectors. *Nuclear Instruments and Methods in Physics Research Section A*, 288(1):13–18, 1990.

[22] W. F. Mueller, J. A. Church, T. Glasmacher, D. Gutknecht, G. Hackman, P. G. Hansen, Z. Hu, K. L. Miller, and P. Quirin. Thirty-two-fold segmented germanium detectors to identify -rays from intermediate-energy exotic beams. *Nuclear Instruments and Methods in Physics Research Section A*, 466(3):492–498, July 2001.

[23] J. Simpson et al. *Acta Physica Hungarica, Heavy Ion Physics*, 159, 2000.

[24] C.E. Svensson, P. Amaudruz, C. Andreoiu, A. Andreyev, R.A.E. Austin, G.C. Ball, D. Bandyopadhyay, A.J. Boston, R.S. Chakrawarthy, A.A. Chen, R. Churchman, T.E. Drake, P. Finlay, P.E. Garrett, G.F. Grinyer, G. Hackman, B. Hyland, B. Jones, R. Kanungo, R. Maharaj, J.P. Martin, D. Morris, A.C. Morton, C.J. Pearson, A.A. Phillips, J.J. Ressler, R. Roy, F. Sarazin, M.A. Schumaker, H.C. Scraggs, M.B. Smith, N.Starinsky, J.J. Valiente-Dobón, J.C. Waddington, and L.M. Watters. Tigress: Triumf-isac gamma-ray escape-suppressed spectrometer. *Journal of Physics G: Nuclear and Particle Physics*, 31(10):S1663, 2005.

[25] T. Kröll and D. Bazzacco. Simulation and analysis of pulse shapes from highly segmented HPGe detectors for the gamma-ray tracking array MARS. *Nuclear Instruments and Methods in Physics Research Section A*, 463(1):227–249, 2001.

[26] A. Wiens, H. Hess, B. Birkenbach, B. Bruyneel, J. Eberth, D. Lersch, G. Pascovici, P. Reiter, and H.-G. Thomas. The AGATA triple cluster detector. *Nuclear Instruments and Methods in Physics Research Section A*, 618(1-3):223–233, June 2010.

[27] Th. Kröll and D. Bazzacco. A genetic algorithm for the decomposition of multiple hit events in the gamma-ray tracking detector MARS. *Nuclear Instruments and Methods in Physics Research Section A*, 565(2):691 – 703, 2006.

[28] F. C. L. Crespi, F. Camera, O. Wieland, G. Benzoni, S. Brambilla, B. Million, and D. Montanari. A pulse shape analysis algorithm for HPGe detectors. *Nuclear Instruments and Methods in Physics Research Section A*, 570(3):459–466, January 2007.

[29] F. Didierjean, G. Duchêne, and A. Lopez-Martens. The Deterministic Annealing Filter: A new clustering method for gamma-ray tracking algorithms. *Nuclear Instruments and Methods in Physics Research Section A*, 615(2):188–200, April 2010.

[30] J. van der Marel and B. Cederwall. Backtracking as a way to reconstruct compton scattered gamma-rays. *Nuclear Instruments and Methods in Physics Research Section A*, 437(2–3):538 – 551, 1999.

[31] G.J. Schmid, M.A. Deleplanque, I.Y. Lee, F.S. Stephens, K. Vetter, R.M. Clark, R.M. Diamond, P. Fallon, A.O. Macchiavelli, and R.W. MacLeod. A -ray tracking algorithm for the GRETA spectrometer. *Nuclear Instruments and Methods in Physics Research Section A*, 430(1):69 – 83, 1999.

[32] C.J. Pearson, J.J.V. Dobon, P.H. Regan, P.J. Sellin, E. Morton, P.J. Nolan, A. Boston, M. Descovich, J. Thornhill, J. Cresswell, I. Lazarus, and J. Simpson. Digital gamma-ray tracking algorithms in segmented germanium detectors. *Nuclear Science, IEEE Transactions on*, 49(3):1209–1215, Jun 2002.

[33] A. Lopez-Martens, K. Hauschild, A. Korichi, J. Roccaz, and J-P. Thibaud. Gamma-ray tracking algorithms: a comparison. *Nuclear Instruments and Methods in Physics Research Section A*, 533(3):454–466, November 2004.

[34] P.-A. Söderström et al. Interaction position resolution simulations and in-beam measurements of the AGATA HPGe detectors. *Nuclear Instruments and Methods in Physics Research Section A*, 638(1):96–109, May 2011.

[35] F.C.L. Crespi, F. Camera, B. Million, M. Sassi, O. Wieland, and A. Bracco. A novel technique for the characterization of a HPGe detector response based on pulse shape comparison. *Nuclear Instruments and Methods in Physics Research Section A*, 593(3):440–447, August 2008.

[36] W. Shockley. Currents to Conductors Induced by a Moving Point Charge. *Journal of Applied Physics*, 9(10):635–636, October 1938.

[37] S. Ramo. Currents Induced by Electron Motion. *Proceedings of the IRE*, 27(9):584–585, September 1939.

[38] B. Birkenbach, B. Bruyneel, G. Pascovici, J. Eberth, H. Hess, D. Lersch, P. Reiter, and A. Wiens. Determination of space charge distributions in highly segmented large volume HPGe detectors from capacitance–voltage measurements. *Nuclear Instruments and Methods in Physics Research Section A*, 640(1):176–184, June 2011.

[39] B. Bruyneel, P. Reiter, and G. Pascovici. Characterization of large volume HPGe detectors. Part II: Experimental results. *Nuclear Instruments and Methods in Physics Research Section A*, 569(3):774–789, December 2006.

[40] T. J. Ross, C. W. Beausang, I. Y. Lee, A. O. Macchiavelli, S. Gros, M. Cromaz, R. M. Clark, P. Fallon, H. Jeppesen, and J. M. Allmond. Neutron damage tests of a highly segmented germanium crystal. *Nuclear Instruments and Methods in Physics Research Section A*, 606(3):533–544, July 2009.

[41] R.J. Dinger. Dead Layers at the Surface of p-i-n Detectors - A Review. *IEEE Transactions on Nuclear Science*, 22(1):135–139, February 1975.

[42] E. Sakai. Slow Pulses from Germanium Detectors. *Nuclear Science, IEEE Transactions on*, 18(1):208–218, 1971.

[43] R.J. Cooper, D.C. Radford, E. Hull, K. Lagergren, P. Mullowney, M.-C. Lin, K. Paul, C. Athens, and M. Loh. Effect of a surface channel on the performance of a P-type Point Contact HPGe detector. *Nuclear Instruments and Methods in Physics Research Section A*, 680:48–55, July 2012.

[44] A. Pullia, F. Zocca, and G. Pascovici. An Advanced Preamplifier for Highly Segmented Germanium Detectors. *IEEE Transactions on Nuclear Science*, 53(5):2869–2875, October 2006.

[45] B. Bruyneel, P. Reiter, A. Wiens, J. Eberth, H. Hess, G. Pascovici, N. Warr, and D. Weisshaar. Crosstalk properties of 36-fold segmented symmetric hexagonal HPGe detectors. *Nuclear Instruments and Methods in Physics Research Section A*, 599(2-3):196–208, February 2009.

[46] A. Pullia, D. Weisshaar, F. Zocca, and D. Bazzacco. Cross-Talk Limits of Highly Segmented Semiconductor Detectors. *IEEE Transactions on Nuclear Science*, 58(3):1201–1205, June 2011.

[47] B. Bruyneel, P. Reiter, A. Wiens, J. Eberth, H. Hess, G. Pascovici, N. Warr, S. Aydin, D. Bazzacco, and F. Recchia. Crosstalk corrections for improved energy resolution with highly segmented HPGe detectors. *Nuclear Instruments and Methods in Physics Research Section A*, 608(1):99 – 106, 2009.

[48] S. Agostinelli et al. Geant4—a simulation toolkit. *Nuclear Instruments and Methods in Physics Research Section A*, 506(3):250 – 303, 2003.

[49] M.R. Dimmock, A.J. Boston, H.C. Boston, J.R. Cresswell, L. Nelson, P.J. Nolan, C. Unsworth, I.H. Lazarus, and J. Simpson. Characterisation Results From an AGATA Prototype Detector. *IEEE Transactions on Nuclear Science*, 56(3):1593–1599, June 2009.

[50] T.M.H. Ha, A. Korichi, F. Le Blanc, P. Désesquelles, N. Dosme, X. Grave, N. Karkour, S. Leboutelier, E. Legay, D. Linget, B. Travers, and P. Pariset. New setup for the characterisation of the AGATA detectors. *Nuclear Instruments and Methods in Physics Research Section A*, 697:123–132, January 2013.

[51] M.R. Dimmock. Characterisation of AGATA Symmetric Prototype Detectors. *PhD thesis, University of Liverpool*, 2008.

[52] T.M.H. Ha. Caractérisation des détecteurs d'AGATA et étude de l'hyperdéformation dans la région de masse A 120. *PhD thesis, Université Paris Sud*, 2009.

[53] J.C. Colosimo. The Characterisation of AGATA High Purity Germanium Detectors for Pulse Shape Analysis. *PhD thesis, University of Liverpool*, 2013.

[54] P. Désesquelles. Determination of the hit locations in segmented HPGe detectors without the use of simulations or scanning systems. *Nuclear Instruments and Methods in Physics Research Section A*, 654(1):324 – 329, 2011.

[55] N. Goel, C. Domingo-Pardo, T. Habermann, F. Ameil, T. Engert, J. Gerl, I. Kojouharov, J. Maruhn, N. Pietralla, and H. Schaffner. Characterisation of a symmetric AGATA detector using the gamma-ray imaging scanning technique. *Nuclear Instruments and Methods in Physics Research Section A*, 700:10 – 21, 2013.

[56] L. Arnold, R. Baumann, E. Chambit, M. Filliger, C. Fuchs, C. Kieber, D. Klein, P. Medina, C. Parisel, M. Richer, C. Santos, and C. Weber. TNT digital pulse processor. *IEEE Transactions on Nuclear Science*, 53(3):723–728, June 2006.

[57] V.T. Jordanov, G.F. Knoll, A.C. Huber, and J.A. Pantazis. Digital techniques for real-time pulse shaping in radiation measurements. *Nuclear Instruments and Methods in Physics Research Section A*, 353:261–264, 1994.

[58] M. Richer and C. Santos. TNT2 Digital Pulse Processor Functionalities and TUC control software. *User's Manual*, July 2007.

[59] R. Brun and F. Rademakers. ROOT—an object oriented data analysis framework. *Nuclear Instruments and Methods in Physics Research Section A*, 389(1):81–86, 1997.

[60] B. Bruyneel and the AGATA collaboration. Determination of the Crystal Orientation of the AGATA Detectors. *LNL Annual report*, pages 66 – 67, 2010.

[61] S.J. Colosimo, S. Moon, A.J. Boston, H.C. Boston, J.R. Cresswell, L. Harkness-Brennan, D.S. Judson, I.H. Lazarus, P.J. Nolan, J. Simpson, and C. Unsworth. Characterisation of two AGATA asymmetric high purity germanium capsules. *Nuclear Instruments and Methods in Physics Research Section A*, 773:124–136, February 2015.

[62] M. Amman and P. N. Luke. Three-dimensional position sensing and field shaping in orthogonal-strip germanium gamma-ray detectors. *Nuclear Instruments and Methods in Physics Research Section A*, 452(1):155–166, 2000.

[63] R.J. Cooper, A.J. Boston, H.C. Boston, J.R. Cresswell, A.N. Grint, L.J. Harkness, P.J. Nolan, D.C. Oxley, D.P. Scraggs, I. Lazarus, J. Simpson, and J. Dobson. Charge collection performance of a segmented planar high-purity germanium detector. *Nuclear Instruments and Methods in Physics Research Section A*, 595(2):401–409, October 2008.

[64] J. Hayward and D. Wehe. Incomplete charge collection in an HPGe double-sided strip detector. *Nuclear Instruments and Methods in Physics Research Section A*, 586(2):215 – 223, 2008.

[65] S. Aydin, F , Recchia, D Bazzacco, E Farnea, and C.A. Ur. Effective size of segmentation lines of an agata crystal. *LNL Annual report*, 2007.

[66] Q. Looker, M. Amman, and K. Vetter. Inter-electrode charge collection in high-purity germanium detectors with amorphous semiconductor contacts. *Nuclear Instruments and Methods in Physics Research Section A*, 781:20–25, May 2015.

[67] B. Bruyneel and B. Birkenbach. AGATA Detector simulation Library (ADL) v. 2.0. *https://www.ikp.uni-koeln.de/research/agata/data/ReadMeADL.pdf*, 2015.

[68] ADL download page. *https://www.ikp.uni-koeln.de/research/agata*, 2015.

[69] M.R. Dimmock, A.J. Boston, J.R. Cresswell, I. Lazarus, P. Medina, P. Nolan, C. Parisel, C. Santos, J. Simpson, and C. Unsworth. Validation of Pulse Shape Simulations for an AGATA Prototype Detector. *IEEE Transactions on Nuclear Science*, 56(4):2415–2425, August 2009.

[70] P. Medina, C. Santos, and D. Villaume. A simple method for the characterization of HPGe detectors. *Proceedings of the 21st IEEE Instrumentation and Measurement Technology Conference, 2004*, 3:1828–1832, May 2004.

Appendix A

Résumé en français

Cette section résume les travaux principaux de cette thèse. Une table de scan 3D de détecteurs gamma (γ) a été développée à l'IPHC. Le système est décrit, puis une partie des résultats du scan d'un détecteur AGATA (cristal B006) sont présentés. Les figures auxquelles il est fait référence sont celles de la version anglaise du manuscrit. Pour une description plus détaillée, le lecteur est invité à porter son attention sur la section en anglais.

A.1 Contexte de l'étude

Le noyau concentre 99.97% de la masse d'un atome et ceux ci représentent l'essentiel de la matière. Alors que les noyaux proches de la vallée de stabilité sont bien connus, ceux qui s'en s'éloignent subissent des effets de couches qui bouleversent la compréhension de leur structure. La prise en compte de ces effets dans les modèles stellaires, permet notamment de mieux modéliser l'abondance des noyaux dans l'univers. La recherche s'oriente aujourd'hui vers l'étude de ces noyaux exotiques où la spectroscopie γ constitue un outil de choix pour sonder l'inconnu.

Durant les années 90, la spectroscopie γ a vu l'apogée de la génération de multidétecteurs utilisant la suppression Compton, tels que EUROBALL [14] ou GAMMASPHERE [15]. Ils étaient composés de plus d'une centaine de détecteurs au Germanium Hyper Pur (GeHP) en arrangement sphérique, doté chacun d'un bouclier d'anticoïncidence. Il s'agit de scintillateurs qui permettent de détecter et donc de rejeter les évènements où seule une partie de l'énergie γ est déposée dans le germanium. L'efficacité de ces instruments est cependant limitée par l'angle solide couvert par le germanium ($<$50% de 4π stéradian), réduit à cause de la place occupée par les boucliers d'anticoïncidence. De plus, l'élargissement des raies γ dû à l'effet Doppler est lié à la granularité des détecteurs, c'est à dire à leur ouverture angulaire (typiquement quelques degrés).

Le développement de nouveaux accélérateurs permet la production de noyaux de plus en plus exotiques, aux taux de production de plus en plus faibles. Les conditions expérimentales qui permettent d'arriver à de tels extrêmes rendent la détection des événements d'intérêt très difficile. Dans l'optique de la recherche de ces noyaux rares parmi un bruit de fond très élevé, un spectromètre γ de nouvelle génération doit être utilisé. Il doit allier grande efficacité, hauts taux de comptages, excellente correction de l'élargissement Doppler et grande granularité.

Les derniers développements en instrumentation, tels que la segmentation multiple de détecteurs au GeHP [21] et la technique de l'analyse des formes d'impulsion [28], ou *Pulse Shape Analysis* (PSA), ont fait émerger le concept du tracking γ : de par le processus de formation du signal dans un détecteur au GeHP, le front de montée du signal a une forme qui dépend de la localisation de l'interaction γ. Dans le germanium multi-segmenté, le signal d'un segment touché par un rayonnement γ induit des signaux dans les segments voisins qui accentuent encore cette information, à tel point que deux dépôts d'énergie indépendants ayant lieux à $\sim$1 mm de distance sont clairement distinguables de par la variation de leurs formes d'impulsion associées. Le PSA compare les formes d'impulsions mesurées expérimentalement avec une base de données de formes d'impulsion calculées. Celà permet de retrouver les coordonnées d'interactions du rayonnement γ, associées aux énergies partielles déposées. L'utilisation de ces informations dans un logiciel de tracking permet de reconstruire le parcours le plus probable du photon γ au sein du détecteur. Les dépôts d'énergie partiels de chaque photon γ reconstitué sont alors sommés, ce qui augmente de manière significative le rapport pic/fond du spectre γ. Par ailleurs, à l'issue du PSA et du tracking, la localisation précise de la première interaction réduit l'ouverture angulaire à une fraction de degré. Cela permet de corriger de manière efficace l'élargissement des pics par effet Doppler. La capacité de détection du spectromètre γ (ou pouvoir de résolution) est ainsi grandement accrue.

C'est dans ce cadre qu'a été conçu AGATA [4] (Advanced GAmma Tracking Array): un multidétecteur haute résolution pour la spectroscopie γ aux extrêmes, développé par une collaboration européenne. Il sera constitué à terme de 180 cristaux au GeHP, couvrant un angle solide de 82% de 4π stéradian et utilisera le tracking γ. Chaque cristal est un cylindre de 80 mm de diamètre pour 90 mm de long, avec des faces avant biseautées conduisant à une section hexagonale irrégulière, pour s'intégrer dans une sphère. La segmentation de chaque cristal consiste en 6 sections et 6 tranches pour un total de 36 segments plus une voie Core, l'anode centrale qui mesure l'énergie déposée dans l'intégralité du cristal. Trois formes de cristaux sont utilisées pour optimiser la couverture angulaire d'AGATA. Elles sont regroupées dans un même cryostat, un triple cluster. AGATA sera constitué de 60 triples clusters.

Le PSA est une opération délicate et cruciale, compte tenu de la quantité de données à traiter. Il est basé sur la comparaison des signaux mesurés avec des bases de données de formes d'impulsion. Celles utilisées à ce jour sont issues de simulations (calculées sur une grille 3D de 2 mm de côté) et permettent au PSA d'atteindre une résolution spatiale de l'ordre de 5 mm à 1 MeV [34]. Cette valeur est assez élevée, elle reflète les divergences entre les bases de données simulées et les formes des signaux expérimentaux.

L'IPHC a développé un banc de scan de détecteurs γ, basé sur la technique de Pulse Shape Comparison Scan [35] (PSCS), qui permet de déterminer de manière expérimentale les formes d'impulsion en fonction de la position d'interaction dans l'ensemble du volume du cristal (48500 points) en trois semaines seulement. Les tables de scan classiques utilisent une technique de coïncidence entre le germanium et des détecteurs scintillateurs collimatés placés latéralement. Le scan de 1200 points dure entre 1 et 2 mois. Les performances de la table de scan de l'IPHC permettront de remplacer les bases de données simulées par des bases expérimentales pour chaque cristal AGATA. L'objectif est d'améliorer la résolution spatiale du PSA et, par conséquent, d'améliorer les performances du spectromètre AGATA.

A.2 Sonder les détecteur avec une table de scan

La table de scan de L'IPHC permet de sonder localement la réponse d'un détecteur γ. Elle consiste en un intense faisceau γ collimaté, monté sur une table XY permettant son déplacement dans un plan. Sa particularité est qu'un détecteur GeHP peut être placé à l'aplomb du faisceau, de manière très précise, suivant deux orientations, horizontale et verticale. La technique du PSCS est alors mise en oeuvre sur les séries de mesures qui se croisent. Son principe, schématisé sur la figure 3.1, page 40, est le suivant: dans un premier temps, le détecteur est placé en position verticale (position A), afin d'éclairer sa face avant. Le faisceau parcourt toute la surface du détecteur. Ainsi, pour chaque position XY dans le détecteur, l'ensemble des formes d'impulsions le long de l'axe Z sont collectées. Dans un second temps, le détecteur est placée à l'horizontale (position B) où il est éclairé latéralement. Ainsi les formes d'impulsions sont collectées dans un plan XY du cristal à une position Z connue. Deux séries de mesures,qui se chevauchent virtuellement en un point M de coordonnées (X_M, Y_M, Z_M) dans le détecteur, contiennent chacune des formes d'impulsions qui diffèrent les unes des autres, sauf au point M où elles sont identiques. Les signaux issus de la mesure A sont comparés à ceux issus de la mesure B à l'aide d'un test de χ^2, afin de sélectionner les signaux les plus semblables entre les deux séries de donnéees. Si la valeur de χ^2 est faible, il s'agit des signaux issus du point de croisement des deux mesures. A la fin du test, les signaux ainsi sélectionnés sont moyennés pour former le signal expérimental au point M. De cette manière, l'information venant de l'intégralité du volume du détecteur est accessible grâce à deux scans de quelques jours seulement, suivis d'une analyse de données post-mesure de cinq jours environ.

Le châssis mécanique du banc de scan est conçu afin de positionner le faisceau γ collimaté le plus précisément possible dans le référentiel du détecteur. La table XY garantit un positionnement à 20 μm près. Le cryostat d'essai AGATA est placé dans une pièce mécanique, l'équerre, qui permet de placer le détecteur dans les positions verticale et horizontale, avec la possibilité de faire une rotation à 360° du détecteur autour de son axe Z, ainsi que des ajustements fins de son azimuth et de son élévation. Afin de garantir que les séries de mesures verticale et horizontale se croisent parfaitement, une procédure de scan et d'alignement a été mise en place. La position relative du cristal par rapport aux axes de la table de scan est déterminée précisément via des scans dédiés en position verticale. Un système d'alignement laser permet de garantir l'alignement lors du passage en position horizontale.

L'électronique d'acquisition numérique est composée de 10 cartes TNT2 [56]. Il s'agit de digitizers de 14 bits à 100 MHz, capables de mesurer précisément l'énergie déposée en utilisant un filtre trapezoïdal [57]. Simultanément, le signal est extrait sur 120 points, soit une fenêtre de 1,2 μs. Un trigger numérique avec un seuil de l'ordre de 30 keV est appliqué sur le signal Core puis propagé sur les 36 segments. Ainsi, s'il y a un dépôt d'énergie, les formes d'impulsions de toutes les voies seront collectées. Cette image instantanée de la réponse du détecteur est la brique de base du PSA. Considérant la finesse de la grille de scan 3D (voxels de 8 mm^2, scans par pas de 2 mm) et la statistique requise pour le test de χ^2, le volume de données brutes à l'issue des mesures est de l'ordre de 4 To par détecteur AGATA.

La source γ est placéee dans un blindage composée de plomb et d'un alliage de tungstène. La collimation est obtenue avec un trou de 1,5 mm de diamètre sur une longueur de 165 mm. Deux sources sont utilisables, dont les caractéristiques sont données dans le tableau 3.1,

page 44. La source de ^{241}Am permet de sonder la surface et de déterminer la position du cristal, tandis que la source de ^{137}Cs permet d'explorer le volume et d'utiliser la technique du PSCS.

A.3 Alignement du détecteur

La procédure d'alignement est la marche à suivre pour garantir le croisement optimal des mesures verticales et horizontales. Deux référentiels sont utilisés, celui de la table de scan (X_T, Y_T, Z_T) et celui du cristal (X_C, Y_C, Z_C). L'axe Z_C est celui du trou central, l'axe Y_C est celui de la ligne de segmentation entre les sections A et F, sur la face avant du cristal. La procédure d'alignement du détecteur est la suivante:

1. Le cryostat est placé en position verticale et aligné grossièrement de telle sorte que la face avant du capot semble parallèle à la face supérieure du collimateur.

2. Le cryostat est tourné autour de l'axe de rotation continu, de sorte que la ligne de segmentation entre les sections A et F du cristal soit colinéaire à l'axe Y_T de la table de scan.

3. Un scan au ^{137}Cs est effectué autour du trou central, le long des axes X_C et Y_C. Le pas entre deux points de mesures est très fin (200 μm) et la statistique est importante (150 s/pt). L'aire du photopic de 662 keV dans les segments de chaque tranche en coincidence est extraite pour chaque point de scan. Son analyse permet de mesurer la position du centre de chaque tranche et donc de déterminer l'inclinaison du trou central par rapport au faisceau γ. Si cette inclinaison est détectable, elle est corrigée grâce aux vis micrométriques de l'équerre prévues à cet effet. A ce moment, l'axe Z_C du cristal et le faiceau γ sont alignés. De même les axes X_C et Y_C sont alignés avec les axes X_T et Y_T de la table de scan (second item).

4. La source de ^{137}Cs est remplacée par le faisceau laser. Les mires (2 trous calibrés espacés de 165 mm, solidaires du cryostat) sont alors ajustées, de telle sorte que la figure de diffraction la plus intense soit observée à leur sortie. A cet instant, les mires donnent l'orientation de l'axe Z_C du cristal, elles resteront fixes jusqu'à la fin de l'ensemble des mesures.

5. Toutes les mesures en position verticale peuvent être effectuées.

6. Le cryostat est placé en position horizontale.

7. Le faisceau laser à la sortie du collimateur est reflété à 90° à l'aide d'un prisme. L'angle de 90° en élévation est défini par le prisme, l'angle azimutal est définit parallèlement à l'axe X_T grâce à une marque de référence calibrée placée sur le mur de la salle de mesure. L'orientation du détecteur est ajustée avec les vis micrométriques, de sorte que le laser passe par les mires. A cet instant, l'axe Z_C du détecteur est perpendiculaire au faisceau γ et aussi parallèle à l'axe X_T.

8. Toutes les mesures en position horizontale peuvent être effectuées.

Chaque étape énumérée ci-dessus a fait l'objet de scans spécifiques afin de vérifier que l'effet du déplacement du détecteur soit bien celui attendu. Cette procédure est maintenant validée, ce qui permettra un gain substantiel de temps pour les mesures futures de cristaux coaxiaux.

A.4 Résultats de scans 2D

Pour chaque scan effectué, un premier niveau d'étude consiste à analyser chaque voie du détecteur de manière individuelle. Cela représente 37 spectres γ à analyser pour plusieurs milliers de point. Les informations qui sont extraites sont typiquement l'aire nette du photopic, la position du centroïde et la largeur à mi-hauteur du photopic.

L'aire nette du photopic de ^{137}Cs pour un scan vertical par pas de 1 mm est montrée sur la figure 4.2, page 61, pour chaque segment du détecteur. Les segments de la première tranche sont atteints par une quantité uniforme de photons γ sur toute leur surface. L'efficacité photopic est donc majoritairement déterminée par les diffusions Compton. Plus la première interaction a lieu au centre du volume, plus la probabilité que le photon γ diffusé soit réabsorbé augmente, plus l'efficacité photopic est importante. Au contraire, à la surface du segment, une grande partie des γ interagissant par effet Compton sont diffusés à l'extérieur du cristal. Ils ne contribuent donc pas à la pleine énergie. Pour les tranches supérieures, l'aire nette observée est liée à la géométrie des segments, mais aussi et surtout à l'atténuation des photons γ incidents par les tranches inférieures. Cette figure donne une estimation de la statistique disponible en chaque point pour le scan 3D dans la section suivante.

Les figures 4.6, page 65 et 4.7, page 66 montrent la position moyenne du centroïde du pic de 662 keV de la source de ^{137}Cs en fonction du rayon d'interaction dans les 6 tranches du cristal, respectivement dans le Core (en coincidence avec un segment touché) et dans les segments. L'allure globale est une baisse du centroide lorsque le rayon augmente, qui est plus marquée dans le Core que dans les segments. Cet effet est caractéristique d'un piégeage d'électrons dans le cristal, qui est un défaut classique du GeHP type n utilisé pour la fabrication des cristaux AGATA. L'effet est cependant très faible et n'affecte que modestement la résolution globale du détecteur.

D'autre mesures ont été effectuées, notamment la détermination de l'orientation des axes cristallographiques dans le cristal. Cette information est accessible en analysant les variations de la longueur des formes d'impulsions, à rayon constant, en fonction de l'azimut de l'interaction (voir figure 4.10, page 70). Le résultat (tableau 4.4) est que l'axe <110> est aligné dans le coin de la section A de la face avant, comme annoncé par le fabricant et mesuré par d'autre moyens [60].

A.5 Résultats du scan 3D

Le PSCS a été mis en oeuvre dans l'ensemble du volume du détecteur. Seul les évènements qui valident les conditions suivantes sont utilisés pour l'analyse de comparaison par χ^2:

1. l'énergie est déposée dans un unique segment afin de sélectionner des interactions uniques,

2. seuls les évènements de 662 keV sont utilisés.

Concernant le second critère, une interaction de 662 keV dans un segment provient très probablement de multiples diffusions Compton confinées dans ce segment Au contraire, une interaction du continuum Compton est très probablement une interaction unique avec diffusion hors du détecteur. Il serait donc plus judicieux d'utiliser les évènements Compton pour le PSCS. Cependant, à cause du bruit de fond radioactif dans la salle de scan, les évènements dans la gamme 0-650 keV ne proviennent pas forcément d'un photon γ issu du collimateur et leur utilisation dans le PSCS donne des résultats incohérents.

Afin de pouvoir comparer les formes d'impulsion entre elles, elles subissent le traitement de normalisation et d'alignement temporel suivant:

- la ligne de base est ramenée à zero,
- les gains des voies électroniques sont alignés,
- le signal Core est normalisé à 10000, le même facteur de normalisation est appliqué aux autres voies,
- l'échantillonage est virtuellement augmenté de 100 MHz à 1 GHz par extrapolation linéaire entre deux points consécutifs,
- une moyenne mobile de 11 points est appliquée sur le signal de 1 GHz,
- le Core est aligné de sorte que le temps à 50% de son amplitude maximum soit à 600 ns,
- le segment qui a le plus grand dépôt d'énergie est aligné de sorte que le temps à 50% de son amplitude maximum soit à 600 ns, le même décalage temporel est appliqué aux autres segments,
- l'échantillonage est ramené à 100 MHz.

L'effet d'un tel filtre préserve la forme globale du signal. Après ce traitement, chaque signal peut être analysé de façon identique, en s'affranchissant des effets de déclenchement de trigger ou des variations de l'énergie déposée.

Une simulation de l'ensemble de la technique a été effectuée. La géomérie du détecteur et du faisceau γ collimaté sont intégrés dans le code, de type Monte-Carlo, Geant4 [48], qui permet de simuler des positions d'interactions γ réalistes. Ces données sont alors utilisées en entrée d'un code de simulation de formes d'impulsion développé spécifiquement. Les formes synthétiques créées passent par un filtrage électronique puis subissent une analyse de χ^2 identique à celle du PSCS. Les formes d'impulsions sélectionnées proviennent d'évènements dont l'historique est connu, ce qui permet d'identifier leur origine. Bien que la section efficace relative d'interaction photo-électrique (donc de mono-interaction) à 662 keV n'est que de 2% du total des interactions, $\sim$43% des formes d'impulsions sélectionnées par le χ^2 proviennent d'évènements photoélectriques (voir tableau 5.1 page 97). Les autres sont des diffusions Compton très proches du premier point d'interaction. Le PSCS est donc efficace pour retrouver les formes d'impulsions du point de croisement.

Le cristal AGATA B006 a été scanné dans tout son volume par la technique de PSCS. La forme d'impulsion moyenne de chacun des 48000 voxels de 8 mm^2 a été mesurée. Deux scans au minimum sont nécessaires, avec chacun une orientation différente du faisceau γ incident. Le volume de données généré ainsi que le temps nécessaire pour la mesure, le traitement et l'analyse des données sont montrés sur la figure 5.6 page 99. Sans optimization de l'algorithme

d'analyse, celle-ci durerait 6 mois. Une astuce pour réduire ce temps est de concentrer la comparaison par χ^2 uniquement sur les échantillons qui contiennent l'information de localisation, c'est à dire sur les formes d'impulsion du Core, du segment touché et de ses 4 segments plus proches voisins (ceux au-dessus, en dessous, à gauche et à droite du segment touché). Seuls les points échantillonnés qui proviennent du front de montée du signal sont utilisés. Les comparaisons d'intérêts sont celles au χ^2 le plus bas. Si une comparaison de forme d'impulsion en cours de calcul a un χ^2 provisoire supérieur à un seuil, cette comparaison est stoppée avant la fin car elle diverge trop. Seules les 200 comparaisons au χ^2 le plus faible sont conservées. La plus élevée de ces valeurs définit le seuil de χ^2 qui varie donc avec le temps : il est élevé au début du test et diminue au fur et à mesure que des comparaisons successives donnent des valeurs de χ^2 plus faibles. La valeur finale informe de la qualité de la comparaison :

- un χ^2 final bas signifie que le test est réussi, et la forme d'impulsion déterminée expérimentalement est fiable,
- un χ^2 final élevé indique que les formes d'impulsion sélectionnées ne sont pas strictement identiques.

Le χ^2 élévé en fin de test peut avoir plusieurs explications :

- les mesures avec faisceau collimaté ne se croisent pas, il n'y a donc pas de formes d'impulsion strictement identiques dans les deux séries de données,
- les mesures avec faisceau collimaté se croisent sur un voxel où il n'y a pas de germanium, typiquement à l'extérieur du cristal, dans le trou central ou encore dans une zone inactive du cristal,
- il y a un manque de statistique dans une série de données, donc il est peu probable de trouver des formes d'impulsion strictement identiques. C'est typiquement le cas le long des bordures extérieures des segments.

Les résultats bruts du PSCS sont montrés sur la figure 5.7(a) page 100. De nombreux points apparaissent alors qu'à l'évidence, ils ne correspondent pas au volume réel du détecteur. Ils sont cependant caractérisés par une valeur de χ^2 élevée, ce qui permet de les rejeter en filtrant les résultats bruts par un simple seuil de χ^2 (voir figure 5.7 page 100). La base de données utilisable est ainsi formée.

Un inconvénient à l'utilisation de formes d'impulsion expérimentales est qu'elles sont issues de mesures, par conséquent elles contiennent du bruit. Si ce bruit est trop important, les résultats du PSA sont trop approximatifs et l'utilisation d'une base expérimentale ne serait pas justifiée. Un exemple de forme d'impulsion finale est montré dans la figure 5.8 page 102. Les voies Core et segment touché ont un dépôt de charges alors que les autres voies ont un signal induit durant la collection des charges. Seules les voies proches de l'interaction ont un signal suffisament intense pour participer à l'information de localisation. Un zoom sur la ligne de base permet d'observer un motif récurrent sur les voies loin de l'interaction. Il est attribué à la diaphonie induite par le Core dans les segments par couplage capacitif. Son amplitude, de l'ordre de 0.4% de l'amplitude maximale est en accord avec la littérature [45]. Plusieurs informations sont tirées de cette figure :

- les résultats de PSCS permettent d'évaluer les effets de diaphonie du Core vers les segments,

- le bruit résiduel des formes d'impulsion moyennes issues du PSCS est très faible, inférieur à 0.1%.

Des exemples de formes d'impulsions extraites de la base de données expérimentale sont montrés dans les figures 5.9 page 103, 5.10 page 104 et 5.11 page 104. Dans chacun des cas, deux formes d'impulsions correspondant à des positions d'interaction séparées de 2 mm sont clairement différenciées. Considérant la continuité entre les formes d'impulsion voisines et le niveau de bruit très faible, la base de données est utilisable telle quelle dans un algorithme de PSA.

A.6 Comparaison de la base de données expérimentale avec une base simulée

Une comparaison de la base de données expérimentale de formes d'impulsions avec les bases de données simulées est effectuée. Pour ce faire les formes d'impulsions simulées passent par un filtre qui reproduit l'effet de l'électronique d'acquisition (voir section 2.5.3 page 35). La conséquence est qu'une grande partie des effets fins se retrouvent moyennés et ne se distinguent plus de l'allure globale. Pour une position donnée, la forme d'impulsion simulée et l'expérimentale semblent à priori assez similaires. Cependant la comparaison a aussi été faite avec des formes d'impulsion simulées provenant d'autres géométries de détecteurs que celle du cristal B006. Il apparaît que la base simulée de B006 ne semble ni meilleure ni pire que celles des cristaux B005, A004 ou C003 par exemple. Plusieurs raisons expliquent ce phénomène :

- les simulations de formes d'impulsions ne reproduisent que partiellement la réalité,
- le filtrage électronique est trop prononcé malgré un important travail de la collaboration AGATA pour produire des préamplificateurs rapides, il ne rend pas compte des variations fines entre chaque cristaux,
- l'effet de diaphonie dérivatif entre les voies (qui modifie les formes d'impulsion) influe plus fortement qu'attendu sur le PSA.

Afin d'évaluer dès à présent les performances du PSA en utilisant une base de données expérimentale, les séries mesurées avec le faisceau collimaté sont analysées. Pour chaque évènement avec un segment touché, la position d'interaction est déterminée en comparant le signal expérimental avec la base de données. La distribution des points d'interaction dans le cristal, le long du faisceau collimaté, permet de déterminer le décalage par rapport à la position du collimateur et une résolution spatiale dans le plan perpendiculaire au faisceau γ. Le décalage moyen des distributions reconstruites dans le plan XY est de 0.99 mm en utilisant la base de donnée expérimentale et de 4.27 mm en utilisant une base simulée. En considérant la largeur de faiceau de 2 mm et en extrapolant avec les valeurs de résolution actuelles d'AGATA, la résolution spatiale pourrait passer de 5-6 mm à 600 keV à 2-3 mm FWHM en utilisant des bases de données expérimentales.

A.7 Conclusion et perspectives

Le cristal AGATA B006 été scanné de manière approfondie à l'IPHC. L'utilisation du Pulse Shape Comparison Scan a permi d'établir pour la première fois une base de données complète de formes d'impulsions expérimentales, selon une grille carrée de 2 mm de côté. La comparaison de cette base de données expérimentale avec des bases simulées montre une variation importante entre les deux, qui est expliquée par une mauvaise estimation du filtrage lié à l'électronique d'acquisition dans les bases de données simulées. L'utilisation de la base de données expérimentale en lieu et place d'une base simulée dans un algorithme de PSA montre une amélioration significative de la résolution spatiale de reconstruction des points d'interaction. Il y a donc tout intérêt à scanner les détecteurs AGATA avec cette méthode. Le temps nécessaire pour reproduire une telle base sur un autre cristal est de deux semaines de scan plus une semaine d'analyse de données, ce qui rend un scan systématique tout à fait envisageable.

Cette base expérimentale doit être testée avec des expériences de physique utilisant AGATA. Dans un premier temps, elle pourrait remplacer chacun des cristaux quels que soit leur géométrie. Une amélioration du PSA devrait être observée ou, tout du moins, une dégradation n'est pas attendue. Par la suite, chaque géométrie de cristal devrait avoir sa propre base de données (ce qui implique encore deux scans à effectuer à l'IPHC, correspondant aux géométries A et C). Si les performances du PSA sont améliorées, alors un scan systématique pourra être planifié.

D'autres effet inattendus ont été observés. La charge d'une mono-interaction peut être partagée entre deux segments pour la fraction des interactions conduisant à la collection des trous sur l'inter-piste séparant les segments. Ou encore, le diamètre effectif du trou central plus large que ce qui est communément pris en compte. La prise en compte de ces effets permettront d'améliorer les performances du spectromètre AGATA ou de mieux les simuler.

La capacité de la table de scan de l'IPHC à étudier finement la réponse des détecteurs au GeHP a été démontrée. La poursuite de ces études permettra d'améliorer les performances d'autres détecteurs dans des domaines tels que l'imagerie γ ou la mesure à bas bruit de fond.

Michaël Ginsz

Caractérisation de détecteurs multi-segmentés au germanium hyper pur

Characterization of high-purity, multi-segmented germanium detectors

L'apparition de la segmentation électrique des détecteurs au GeHP et de l'électronique numérique a ouvert la voie à des applications prometteuses, telles que le tracking γ, l'imagerie γ ou la mesure bas bruit de fond, pour lesquelles une connaissance fine de la réponse du détecteur est un atout. L'IPHC a développé une table de scan utilisant un faisceau γ collimaté, qui sonde la réponse d'un détecteur dans tout son volume en fonction de la localisation de l'interaction γ. Elle est conçue pour utiliser une technique innovante de scan 3D, le Pulse Shape Comparison Scan, qui a été d'abord simulée afin de démontrer son efficacité. Un détecteur AGATA a été scanné de manière approfondie. Des scan 2D classiques ont permis, entre autres, de mettre en évidence des effets locaux de modification de la collection des charges, liés à la segmentation. Pour la première fois, une base de données 3D, complète, de formes d'impulsions fonction de la position d'interaction γ a été établie. Elle permettra notamment d'améliorer les performances du spectrometre γ AGATA.

Mots clé : spectroscopie gamma, détecteur germanium hyper pur, table de scan, analyse de formes d'impulsions, partage de charge, multi-détecteur AGATA.

Recent developments of electrical segmentation of HPGe detectors, coupled with digital electronics have led to promising applications such as γ-ray tracking, γ-ray imaging or low-background measurements which will benefit from a fine knowledge of the detector response. The IPHC has developed a new scanning table which uses a collimated γ-ray beam to investigate the detector response as a function of the location of the γ-ray interaction. It is designed to use the Pulse Shape Comparison Scan technique, which has been simulated in order to prove its efficiency. An AGATA detector has been thoroughly scanned. 2D classical scans brought out, for example, local charge collection modification effects such as charge sharing, due to the segmentation. For the first time, a 3D, complete pulse-shape database has been established. It will especially allow to improve the overall AGATA array performances.

Keywords : γ-ray spectroscopy, hyper-pure germanium detector, scanning table, pulse-shape analysis, charge sharing, AGATA array.